UV DISINFECTION BETWEEN CONCENTRIC CYLINDERS

A Dissertation
Presented to
The Academic Faculty

by

ZHENGCAI YE

In Partial Fulfillment
of the Requirements for the Degree
Doctor of Philosophy in the
School of Chemical and Biomolecular Engineering

Georgia Institute of Technology
May 2007

UV DISINFECTION BETWEEN CONCENTRIC CYLINDERS

Approved by:

Dr. Larry J. Forney, Advisor
School of Chemical & Biomolecular Engineering
Georgia Institute of Technology

Dr. Pradeep Agrawal
School of Chemical & Biomolecular Engineering
Georgia Institute of Technology

Dr. Spyros G. Pavlostathis
School of Civil and Environmental Engineering
Georgia Institute of Technology

Dr. Victor Breedveld
School of Chemical & Biomolecular Engineering
Georgia Institute of Technology

Mr. John Pierson
Georgia Tech Research Institute
Georgia Institute of Technology

Date Approved: December 1, 2006

DEDICATION

To Mom, Wife, and …

ACKNOWLEDGEMENTS

First, I would like to acknowledge my advisor Dr. Larry Forney for his guidance and support. I also want to thank Dr. Tatiana Koutchma for her guidance and support when I worked at National Center for Food Safety and Technology (NCFST), Illinois Institute of Technology in summer 2005.

Second, I would like to thank Mr. John Pierson for his guidance, suggestions and help during my experiments. I also would like to thank other committee members, Dr. Pradeep Agrawal, Dr. Victor Breedveld, Dr. Spyros Pavlostathis and Dr. Mark White for their valuable advice.

I also thank Dr. Aklilu Giorges for his suggestions and help during my experiments and helpful discussion.

Finally FoodPAC (Food Processing Advisory Council for the State of Georgia), Georgia Tech Research Institute Agricultural Technology Research Program and U. S. Food and Drug Administration are gratefully acknowledged for financial support. Fluent Inc. (Lebanon, NH) is gratefully acknowledged for their software.

TABLE OF CONTENTS

LIST OF TABLES

LIST OF FIGURES

NOMENCLATURE

A	absorption coefficient with 10 base, cm^{-1}, $I_x = I_0 \times 10^{(-Ax)}$
Av	Avogadro's number, 6.023×10^{23} photons/einstein
c	constant which is combined with boundary layer thickness δ to correct for deviations between real reactors and plug flow reactors, cm
C_1	constant determined by κ, $C_1 = \frac{2}{\frac{1-\kappa^4}{1-\kappa^2} - \frac{1-\kappa^2}{\ln(1/\kappa)}}$
C_A	constant, $C_A = \Omega_1 \frac{1-\mu_{21}R_2^2/R_1^2}{1-R_2^2/R_1^2}$
d	gap width, cm
d_h	the hydraulic diameter, m
De	Dean number
h	the wave amplitude of wavy rotors, mm
H	depth of the petri dish, cm
i	event level
I	fluence rate, mW/cm^2
I_0	incident fluence rate, mW/cm^2
I_{av}	average fluence rate, mW/cm^2
I(r)	fluence rate at the position of the gap r, mW/cm^2
I_x	fluence rate at the path length x, mW/cm^2
It	UV fluence, mJ/cm^2
J_i	diffusion flux of i^{th} species, $kg/m^2 \cdot s$
k	the inactivation constant, cm^2/mJ

L	the length of radiation section, cm
L_c	the characteristic length, m
Lw	the wavelength of wavy rotors, mm
n	threshold for inactivation in the series-event model
m	dimensionless group, $m = \frac{R_m - R_1}{R_2 - R_1}$
N	concentration of viable microorganisms, CFU/mL
N_0	concentration of viable microorganisms before exposure, CFU/mL
N_{av}	average concentration of viable microorganisms at the outlet of the reactor, CFU/mL
N_i	concentration of viable microorganisms at event level i, CFU/mL
P	pressure, Pa
Q	volumetric flow rate, mL/s
r	radius, cm
R_1	radius of inner cylinder, cm
R_2	radius of outer cylinder, cm
R^2	the coefficient of determination
Rc	dimensionless group, $\frac{2R_1}{R_1 + R_2}$ (irradiated from the inner cylinder) or $\frac{2R_2}{R_1 + R_2}$ (irradiated from the outer cylinder)
R_{curv}	the mean radius of curvature, m
R_i	net rate of production of i^{th} species, kg/s
Re	Reynolds number
R_m	one radius meeting the mean value theorem, $R_1 \le R_m \le R_2$
Sc_t	turbulent Schmidt number

t	time, s
Ta	Taylor number
Ta_{cr}	critical Taylor number
u	velocity, cm/s or m/s
u_r	radial velocity components, cm/s
u_z	axial velocity components, cm/s
u_τ	the friction velocity, $u_\tau = \sqrt{\tau_w / \rho_w}$
U_{av}	average velocity, $\mathrm{Uav} = \frac{Q}{\pi(R_2^2 - R_1^2)}$, cm/s
x	the path length or x coordinate, cm
y+	a nondimensional parameter defined by the equation, $y^+ = \frac{\rho u_\tau y_P}{\mu}$
y_P	the distance from point P to the wall
Y_i	mass fraction of i^{th} species
z	axial coordinate, cm
α	absorption coefficient with e base, cm^{-1}, $I_x = I_0 \exp(-\alpha x)$
θ	angle around the cylinder, degree, $0 \le \vartheta \le 2\pi$
κ	ratio of the radius of the inner cylinder to that of outer cylinder, $\kappa = R_1 / R_2$
λ_w	wavelength, m
λ	penetration depth, cm
μ	dynamic viscosity, Pa·s
μ_{21}	the ratio of angular velocity of the outer cylinder to that of inner cylinder, $\mu_{21} = \Omega_2 / \Omega_1$
μ_t	turbulent viscosity, Pa·s
ν	kinematic viscosity, m^2/s

ρ	density, g/cm^3
σ_y	the standard deviation of log reductions
τ_{av}	average residence time, s
Ω	angular velocity, s^{-1}
Ω_1	angular velocity of inner cylinder, s^{-1}
Ω_2	angular velocity of outer cylinder, s^{-1}

SUMMARY

Outbreaks of food-born illness associated with the consumption of unpasteurized juice and apple cider have resulted in a rule published by the U.S. Food and Drug Administration (FDA) in order to improve the safety of juice products. The rule (21 CFR120) requires manufacturers of juice products to develop a Hazard Analysis and Critical Control Point (HACCP) plan and to achieve a 5-log reduction in the number of the most resistant pathogens. Ultraviolet (UV) disinfection is one of the promising methods to reach this 5-log reduction of pathogens.

The absorption coefficients of juices typically vary from 10 to 40 cm^{-1} and can be even higher depending on brand and processing conditions. Thin film reactors consisting of two concentric cylinders are suitable for inactivating pathogens in juices. When the two concentric cylinders are fixed, the flow pattern in the gap can be laminar Poiseuille flow or turbulent flow depending on flow rates. If the inner cylinder is rotating, and the rotating speed of the inner cylinder exceeds a certain value, the flow pattern can be either laminar or turbulent Taylor-Couette flow.

UV disinfection between concentric cylinders in laminar Poiseuille flow, turbulent flow and both laminar and turbulent Taylor-Couette flow was investigated experimentally and numerically. This is the first systematic study done on UV disinfection between concentric cylinders in all three flow patterns. The present work provides new experimental data for pathogen inactivation in each of the three flow patterns. In addition, the present study constitutes the first systematic numerical CFD predictions of expected inactivation levels. Proper operating parameters and optimum gap widths for different flow patterns are suggested. It is concluded that laminar Poiseuille flow provides inferior (small) inactivation levels while laminar Taylor-Couette

flow provides superior (large) inactivation levels. The relative inactivation levels are: laminar Poiseuille flow < turbulent flow < laminar Taylor-Couette flow.

CHAPTER 1

INTRODUCTION

1.1 Ultraviolet Disinfection

1.1.1 Disinfection Methods

Disinfection, as applied to water treatment, wastewater treatment and food processing, is a process by which pathogenic microorganisms are inactivated to provide public health protection. There are two common types of methods to achieve disinfection: (1) Chemical disinfection such as chlorination; (2) Physical disinfection such as pasteurization and ultraviolet (UV) disinfection.

The traditional disinfection method is chlorination. The main problems associated with chlorination are residual chlorine compounds and the danger of handling chlorine. Dechlorination and other safety requirements increase the cost of chlorine-based disinfection while the cost of UV disinfection has been reduced because new and efficient UV disinfection systems have been developed. Currently, the cost of the two processes is similar for wastewater disinfection (Water Environment Federation, 1996). Furthermore, because of residual chlorine compounds, chlorination is mainly used for processing of water or wastewater, and it is seldom used for processing of liquid foods such as juices.

Among physical disinfection methods, thermal pasteurization has been used for processing of foods for many years. Because it is a thermal method, the flavor of foods is affected and some nutritional components, which are sensitive to heat, are destroyed during the disinfection process. Moreover, it is cost-prohibitive for small juice producers (Koutchma et. al, 2004b).

Outbreaks of food-born illness associated with the consumption of unpasteurized juice and apple cider have resulted in a rule published by the U.S. Food and Drug

Administration (FDA) in order to improve the safety of juice products. The rule (21 CFR120) requires manufacturers of juice products to develop a Hazard Analysis and Critical Control Point (HACCP) plan and to achieve a 5-log reduction in the numbers of the most resistant pathogens (US FDA, 2000).

UV disinfection is one of promising methods to reach the 5-log reduction of pathogen. Compared with traditional disinfection methods such as pasteurization and chlorination, UV disinfection has following advantages:

(1) Because UV disinfection is a physical method, it leaves no harmful chemical residuals,

(2) Because UV disinfection is a non-thermal method, the flavor of food is not affected. Nutritional components, which are sensitive to heat, are not destroyed by the UV disinfection process or are destroyed less than by pasteurization.

However, like other photochemical reaction systems, UV disinfection has a unique and intrinsic characteristic since radiation energy is absorbed by the fluid in which the microorganisms are suspended leading to non-uniform fluence rates. The simplified form of the radiative transfer equation is Lambert-Beer's law,

$$I_x = I_0 \exp(-\alpha x) \tag{1.1}$$

where

I_x, fluence rate at path length x, mW/cm^2;

I_0, incident fluence rate, mW/cm^2;

α, absorbance coefficient (e base), cm^{-1};

x, path length, cm.

From equation (1.1), the radiation fluence rate decreases exponentially with the path length from the radiation source. In other words, the non-uniform disinfection rates caused by the non-uniformity of fluence rate can severely limit disinfection efficiency especially when liquid foods with high absorption coefficients are treated. The non-

uniform disinfection rates present a big challenge when designing UV disinfection reactors. The application of UV to juice disinfection is the main topic of this study.

1.1.2 Mechanism of UV Disinfection

Light is characterized by its wavelength. UV has wavelengths between 200 – 400 nm and can be further divided into UVA (320-400 nm), UVB (280-320 nm) and UVC (200-280 nm). Approximately 85% of the output from low-pressure mercury arc lamps is monochromatic at a wavelength of 254 nm (Water Environment Federation, 1996). According to equation (1.2),

$$E_\lambda = \frac{hC}{\lambda_w} Av \tag{1.2}$$

where

E_λ, radiant energy at a given wavelength λ_w, kJ/einstein;

C, speed of light, 3×10^8 m/s;

h, Planck's constant, 6.626×10^{-34} J·s;

λ_w, wavelength, m;

Av, Avogadro's number, 6.023×10^{23} photons/einstein.

Therefore, radiant energy at λ_w = 254 nm has 472 KJ/einstein. In a photochemical reaction, one einstein represents one "mole". It should be noted that 472 KJ/einstein or 472 KJ/mole is greater than the bond energies of several important bonds in microbial systems. For example, the C-H bond is about 401-414 KJ/mole and the C-C bond is about 347-355 KJ/mole (March, 1985). Both proteins and nucleic acids are effective absorbers of UVC. This absorption causes genetic damage and thus disinfection of bacteria and viruses; therefore, UVC light is also referred to as germicidal radiation.

DNA (Deoxyribonucleic acid) consists of a sequence of four constituent bases known as purines (adenine and guanine) and pyrimidines (thymine and cytosine). They are linked together in a double-stranded helix. When UVC radiation is absorbed by the

pyrimidine bases (mainly thymines), it permits a unique photochemical reaction, which leads to dimerization of adjacent pyrimidines (formation of a chemical bond between the pyrimidines). Most of the time, the dimerization happens with thymines as shown in Figure 1.1, but cytosine dimers and thymine-cytosine heterodimers can also be formed. This disruption in the structure of the DNA makes it unable to replicate when the cell undergoes mitosis. This is the fundamental mechanism of UV disinfection (Jagger, 1967).

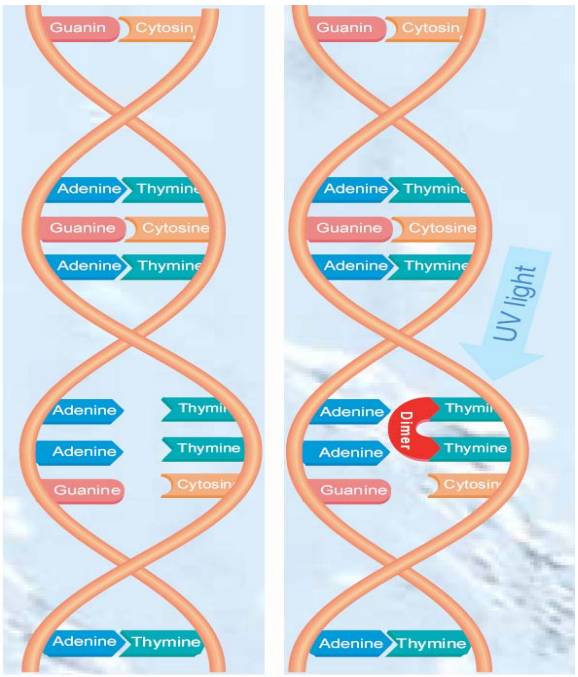

Figure 1.1 UV inactivates microorganisms by disrupting their DNA (from Radata, 2006)

1.1.3 UV Reactors Configuration

According to lamp geometry, the majority of UV disinfection systems for wastewater processing today are open-channel, modular design and can be divided into two groups as shown in Figure 1.2 (Water Environment Federation, 1996):

(a) Horizontal lamp configuration. Principal flow direction is parallel to lamp axes

(b) Vertical lamp configuration. Principal flow direction is perpendicular to staggered lamp

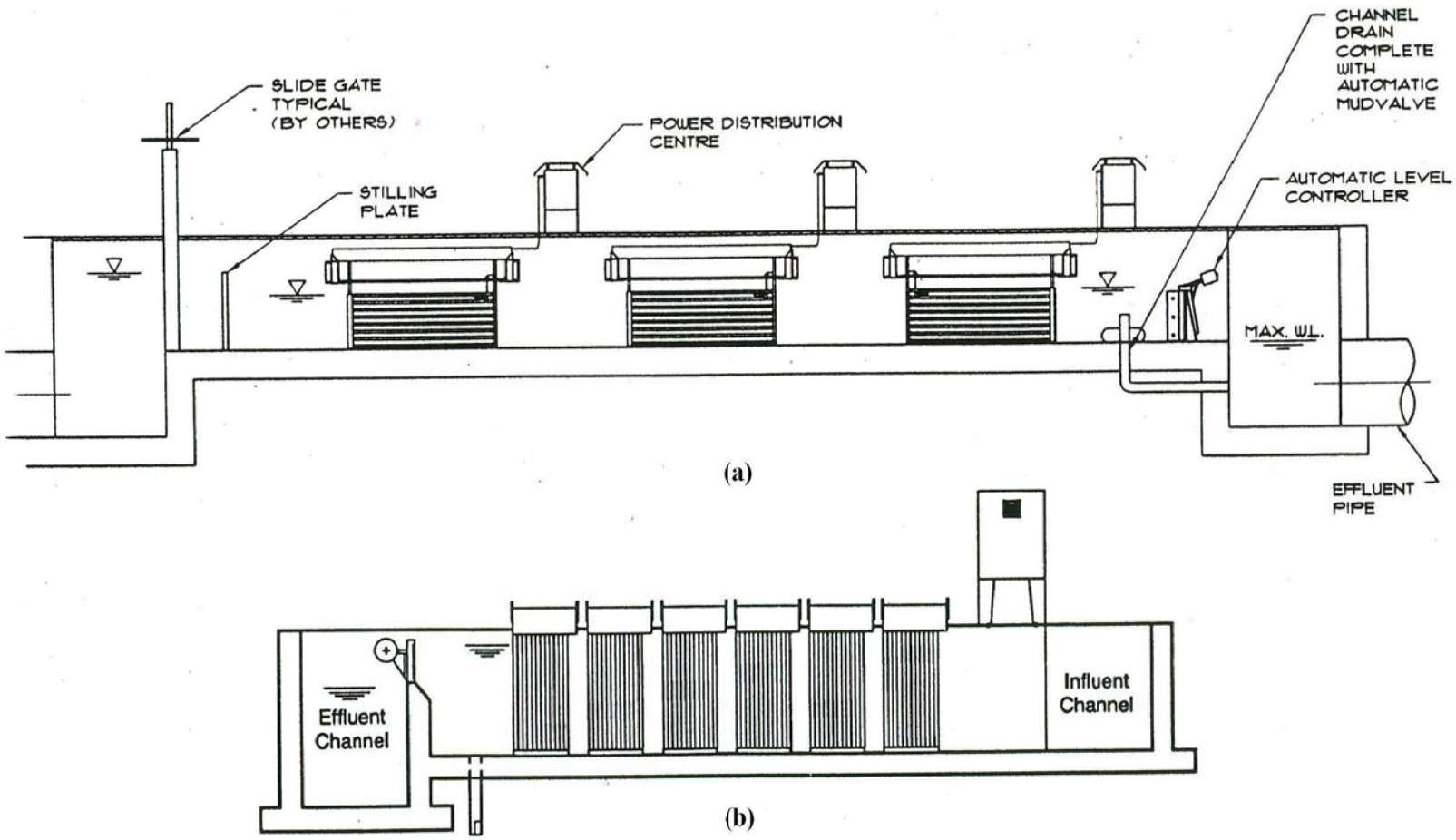

Figure 1.2 (a) **Schematic illustration of open-channel UV disinfection system with horizontal lamp configuration**

(b) **Schematic illustration of open-channel UV disinfection system with vertical lamp configuration (from Water Environment Federation, 1996)**

The above configurations are suitable for processing large quantities of liquids with low absorption coefficients such as wastewater (Chiu et al., 1999, Lyn et al., 1999). The absorption coefficients of juices typically vary from 10 to 40 cm^{-1} and can be even higher depending on brand and processing conditions. If the above configurations are used to disinfect juices with high absorption coefficients, the required distance between two neighboring lamps is very small. Another type of UV reactor producing an annular thin film between two concentric cylinders is more suitable for inactivating pathogens in juices. The schematic diagram of a thin film annular reactor is shown in Figure 1.3. The juices flow through the gap formed by two concentric cylinders. UV is irradiated from the inner cylinder (quartz sleeve) so that pathogens are inactivated.

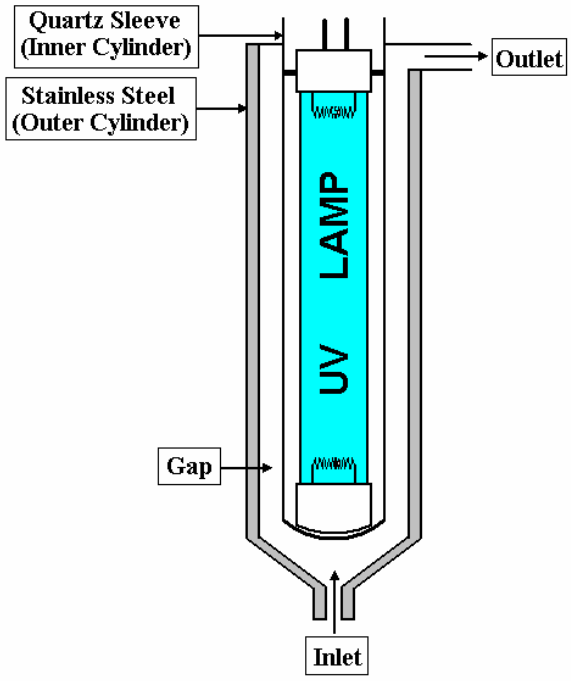

Figure 1.3 Schematic diagram of a thin film annular reactor

When the two concentric cylinders are fixed, the flow pattern in the gap can be laminar Poiseuille flow or turbulent flow depending on flow rates. If the inner cylinder is rotating, and the rotating speed of the inner cylinder exceeds a certain value, the flow pattern can be either laminar or turbulent Taylor-Couette flow (Taylor, 1923, Lueptow et

al., 1992). UV disinfection in laminar Poiseuille flow, turbulent flow and both laminar and turbulent Taylor-Couette flow will be investigated.

1.2 Taylor-Couette Flow

1.2.1 Brief History of Taylor-Couette Flow

It is often thought that the study of Taylor-Couette flow began with Taylor's first paper (Taylor, 1923), but his work was actually built on three persons' earlier work. Couette (1890) experimented with two long concentric cylinders with the inner cylinder fixed and the outer cylinder rotating. He observed by experiments that the torque sustaining the steady rotation increased linearly with angular velocity of the outer cylinder, Ω_2, if Ω_2 was less than a critical value. However, the torque increased sharply when Ω_2 was greater than the critical value. Couette concluded that the change from steady laminar flow to turbulent flow resulted in the abrupt increase in the torque. Afterwards, Mallock (1896) confirmed Couette's observation and extended Couette's experiments to the case with the inner cylinder rotating. He showed an important difference between the two cases:

(1) If the outer cylinder was fixed with the inner cylinder rotating, the flow was always unstable at all speeds tested.

(2) If the inner cylinder was fixed with the outer cylinder rotating, the flow was stable until the rotation of the outer cylinder produced turbulence.

Because both Couette and Mallock concentrated on viscosity measurements, hydrodynamic instability was not investigated in depth. Inspired by Mallock's work, Lord Rayleigh (1916) realized the role of angular momentum in promoting instability, and the Rayleigh criterion was proposed, i.e., the flow of ***inviscid*** fluid is stable when the cylinders rotate in the same direction and equation (1.3) is met,

$$\Omega_2 R_2^2 > \Omega_1 R_1^2 \tag{1.3}$$

where Ω_2 and Ω_1 are angular velocities of the outer and inner cylinder respectively, and R_2 and R_1 are radii of the outer and inner cylinder respectively.

Taylor (1923) extended the works of Couette, Mallock and Rayleigh, and verified his calculations experimentally with very long cylinders. Taylor also observed the appearance of the toroidal vortices (now known as Taylor or Taylor-Couette vortices) under some circumstances. Figure 1.4 is the center section of such a pattern (Koschmieder, 1979) when $Ta=1.16\ Ta_{cr}$, where Ta_{cr} is the critical Taylor number for transition from Couette flow to Taylor-Couette flow. The Taylor number is here defined as:

$$Ta = \frac{2\kappa^2}{1-\kappa^2}\frac{\Omega_1^2 d^4}{\upsilon^2} \tag{1.4}$$

where κ is the radius ratio of the inner cylinder to the outer cylinder, Ω_1 is the angular velocity of the inner cylinder, d is the gap width, and ν is the kinematic viscosity.

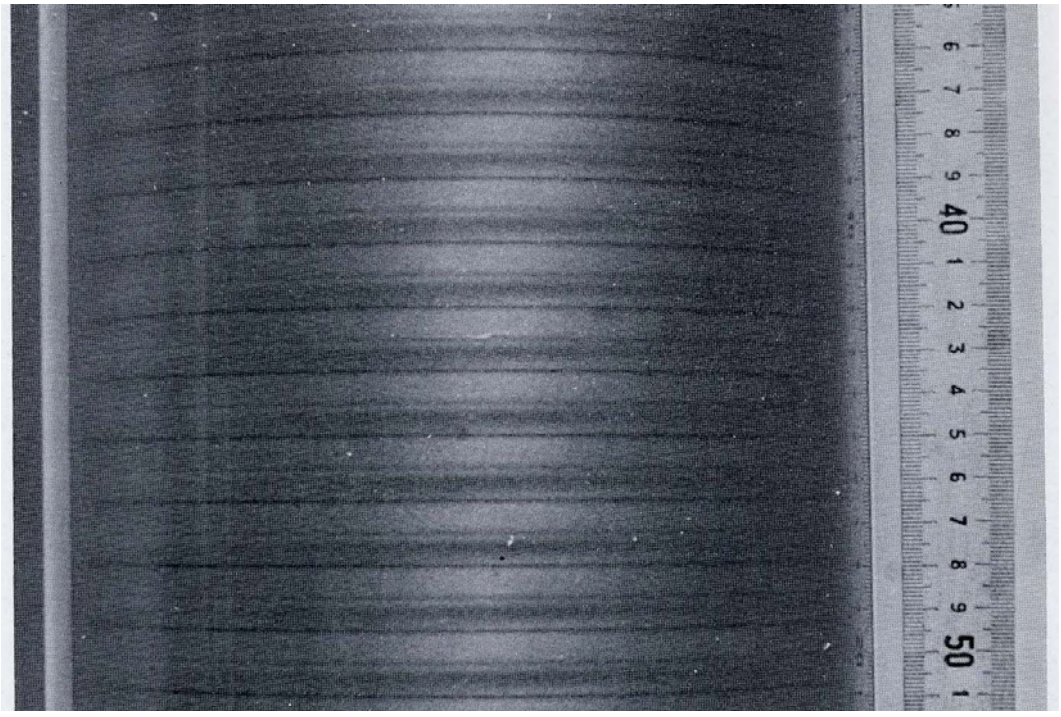

Figure 1.4 Center section of the fluid column with laminar axisymmetric Taylor vortices at $Ta=1.16\ Ta_{cr}$ (from Koschmieder, 1979)

Actually there are now several different forms of the Taylor number depending on one or both of two cylinders rotating. For example, when both cylinders are rotating, the Taylor number can be defined as,

$$Ta = -2\Omega_1 C_A (1+\mu_{21}) d^4 / \upsilon^2 \tag{1.5}$$

that was used by Chandrasekhar (1960), where μ_{21} is the ratio of the angular velocity of the outer cylinder to that of inner cylinder, $\mu_{21} = \Omega_2 / \Omega_1$, and $C_A = \Omega_1 \dfrac{1-\mu_{21} R_2^2 / R_1^2}{1-R_2^2 / R_1^2}$. If the inner cylinder is rotating and the outer cylinder is fixed, $\mu_{21} = 0$ and equation (1.5) will be reduced to equation (1.4) except for an opposite sign. Another form of the Taylor number with only the inner cylinder rotating is

$$Ta = \frac{4\Omega_1^2 R_1^2 (R_2 - R_1)^3}{\upsilon^2 (R_1 + R_2)} \tag{1.6}$$

that was used by Hasoon and Martin (1977). Actually, substitution of $\kappa = R_1/R_2$ and $d = R_2-R_1$ into equation (1.4) gives one half the value of equation (1.6) or $Ta_{(equation 1.6)} = 2Ta_{(equation 1.4)}$. Finally, the form,

$$Ta = \frac{R_1 \Omega_1 d}{\upsilon} \tag{1.7}$$

was used by Lueptow et al. (1992) and Wereley and Lueptow (1999). Because equation (1.7) is similar to the Reynolds number, it is also called the rotating Reynolds number.

Since the effect of the radius ratio is not considered in equation (1.7), the following form including the effect of the radius ratio can be defined as,

$$Ta = \frac{R_1 \Omega_1 d}{\upsilon} \left(\frac{d}{R_1} \right)^{1/2} \tag{1.8}$$

that has been used more extensively (Coeuret and Legrand, 1981, Sczechowski et al., 1995, Xue et al., 2002, Forney et al., 2003a). If $R_1 + R_2 \cong 2R_1$ is substituted into

equation (1.4), it can be shown that the value of equation (1.4) is the square of equation (1.8), namely, $Ta_{(equation\ 1.4)} = \left[Ta_{(equation\ 1.8)}\right]^2$. The form of equation (1.8) will be used in this thesis unless otherwise noted.

Because of Taylor vortices' special characteristics, Taylor-Couette flow has been extensively studied, both experimentally and theoretically. These studies mainly focused on variations of study by Taylor and mass and heat transfer in Taylor-Couette flow.

1.2.2 Taylor-Couette Flow without an Axial Flow

Because G. I. Taylor's pioneering work focused on the transition from Couette flow to Taylor-Couette flow, later research was extended to the transition from laminar Taylor-Couette flow to turbulent Taylor-Couette flow, finally to turbulent flow (Donnelly, 1958, Coles, 1965, Davey et al., 1968, Fenstermacher et al., 1979, Koschmieder et al., 1979, Jones, 1985, Andereck et al., 1986). In Coles' experiments (Coles, 1965), two distinct kinds of transition were identified. The first transition was caused by the inner cylinder rotating faster than the outer cylinder. With the increase in rotating speeds, a series of periodic flows were excited. Therefore, the first transition was also referred to as spectral evolution. On the other hand, the second transition was caused by the outer cylinder rotating faster than the inner cylinder. Two distinct flow patterns, laminar and turbulent, were divided by a fixed Reynolds number. Then, the second transition was also referred to as catastrophic transition. Coles' main results are shown in Figure 1.5. Ro and R_i in Figure 1.5 represent the rotating Reynolds numbers of the outer cylinder and inner cylinder, respectively, based on the radius and the surface speed.

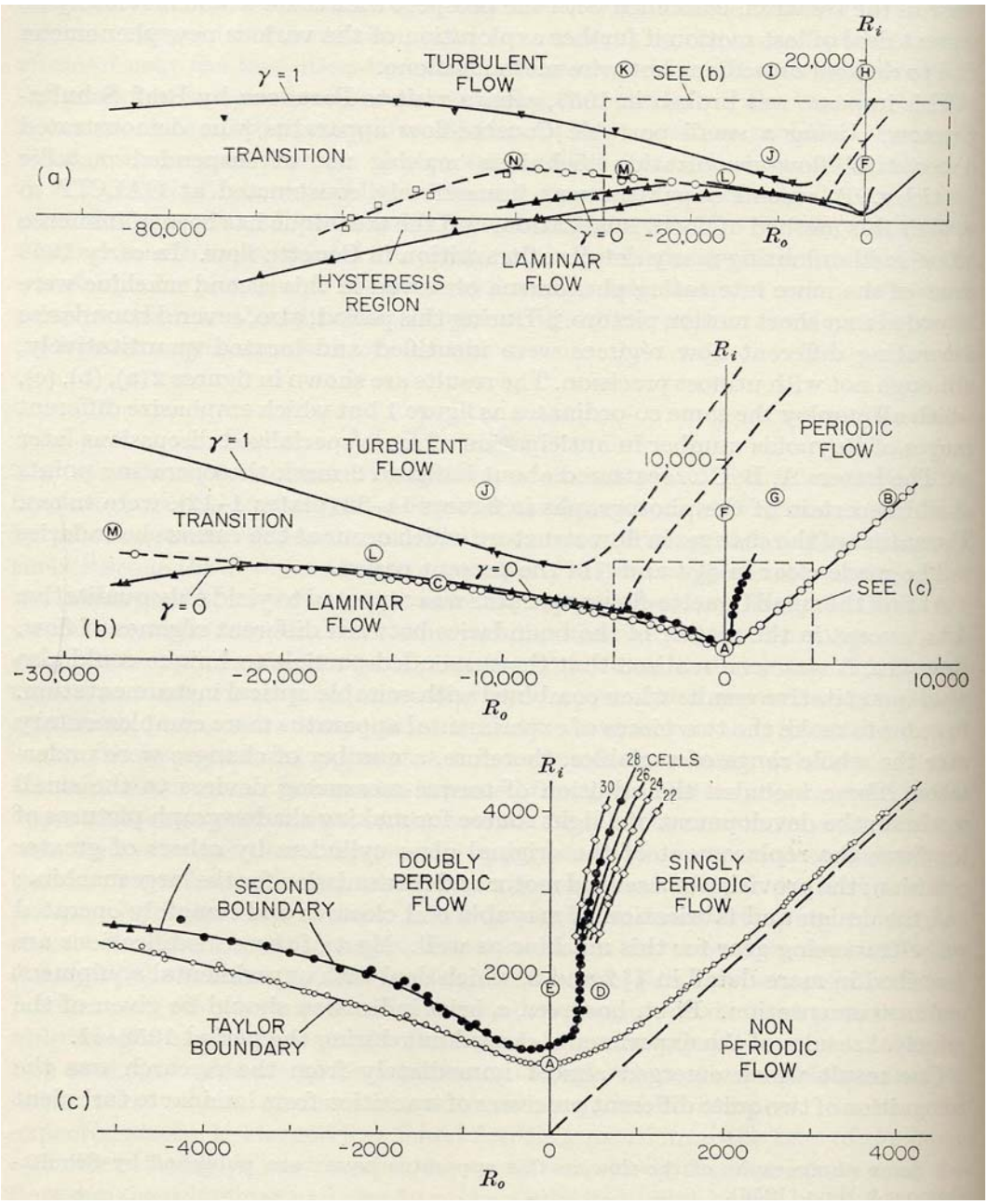

Figure 1.5 Different regimes in circular Couette flow from visual observation (From Coles, 1965)

In Andereck's experiments (Andereck et al., 1986), the same protocol as Coles' (1965) was followed, and observed states included "*Taylor vortices, wavy vortices, modulated wavy vortices, vortices with wavy outflow boundaries, vortices with wavy inflow boundaries, vortices with flat boundaries and internal waves (twists), laminar*

spirals, interpenetrating spirals, waves on interpenetrating spirals, spiral turbulences, a flow with intermittent turbulent spots, turbulent Taylor vortices, a turbulent flow with no large-scale features and various combinations of these flows." Their main results are shown in Figure 1.6.

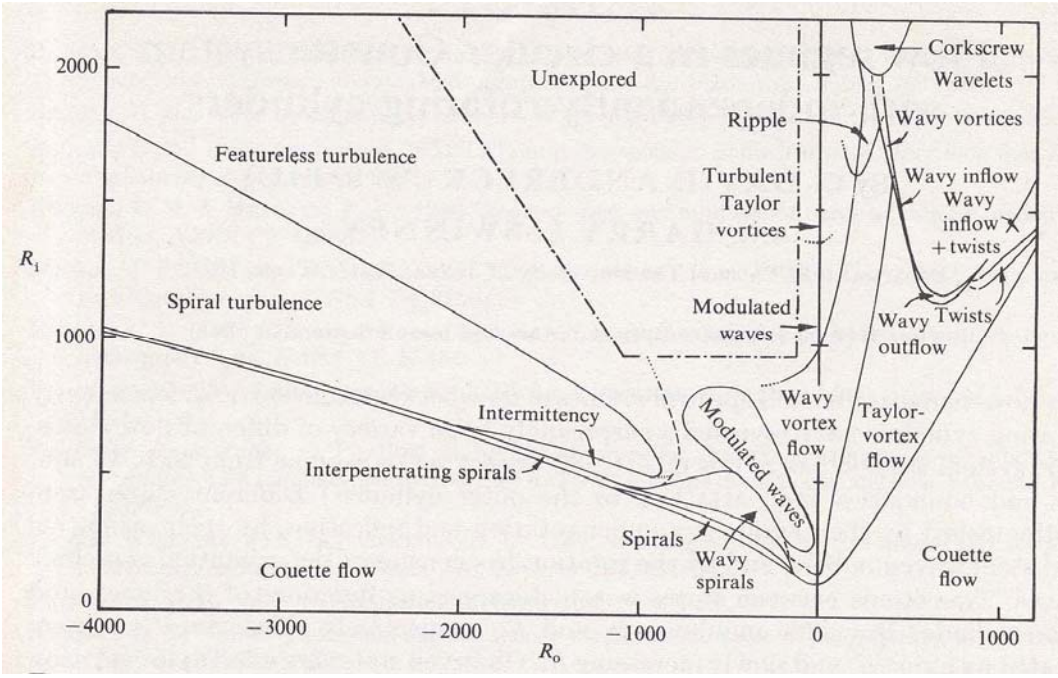

Figure 1.6 Regimes observed in flow between independently rotating concentric cylinders (From Andereck et al., 1986)

According to Figure 1.6, when the outer cylinder was fixed (R_0=0), six flow states were observed. With increasing angular velocity of the inner cylinder, these flow states were:

1) Couette flow
2) Taylor vortex flow (see Figure 1.4)
3) Wavy vortex flow (see Figure 1.7)
4) Modulated wavy vortex flow
5) Turbulent Taylor vortex flow (see Figure 1.8)
6) Turbulent flow

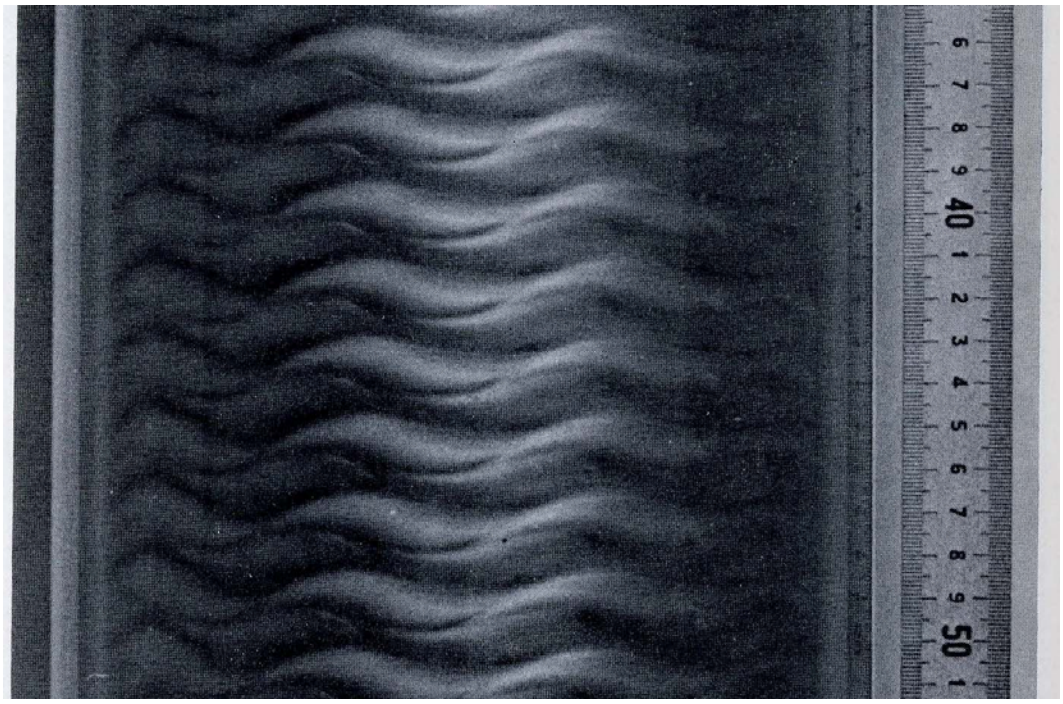

Figure 1.7 Center section of wavy vortex flow at Ta=8.49 Ta_{cr} (from Koschmieder, 1979)

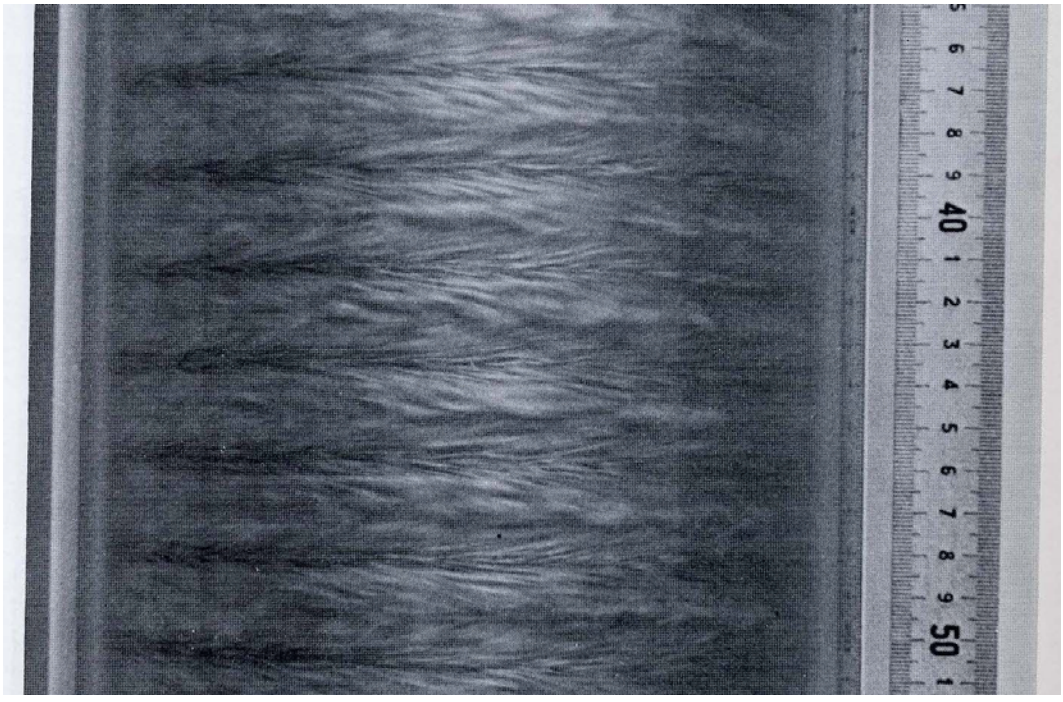

Figure 1.8 Center section of turbulent Taylor vortex flow at Ta=3800 Ta_{cr} (from Koschmieder, 1979)

1.2.3 Taylor-Couette Flow with an Axial Flow

When pressure-driven Poiseuille flow (axial flow) is superimposed on Taylor-Couette flow, the shear instability caused by the axial flow and the centrifugal instability caused by the circular Couette flow cause a transition from laminar Couette-Poiseuille flow to axial flow with toroidal Taylor vortices (sometimes called Taylor-Couette-Poiseuille flow in many references in order to differentiate from Taylor-Couette flow without an axial flow). The combination of the two different instabilities forms a rich variety of flow regimes depending on the flow conditions (Lueptow et al., 1992). Taylor-Couette-Poiseuille flow can be found in several engineering applications, including rotating machinery, heat and mass transfer and journal bearings.

Taylor-Couette-Poiseuille flow (abbreviated as Taylor-Couette flow below for brevity) was first studied by Goldstein (1937) though his results were proven wrong afterwards by many researchers. Later, an axisymmetric disturbance in a narrow annular gap was applied to analyze Taylor-Couette-Poiseuille flow numerically (Chandrasekhar, 1960, DiPrima, 1960). Then, wide annular gaps were considered (Hasoon and Martin, 1977, DiPrima and Pridor, 1979, Fasel and Booz, 1984). Their research showed that toroidal Taylor vortices advanced downstream with the axial flow. If the assumption of the axisymmtric disturbance was removed and the disturbance was assumed to be non-axisymmetric, a new regime, pairs of helical vortices, was predicted (Chung and Astill, 1977, Takeuchi and Jankowski, 1981, Ng and Turner, 1982).

Many experiments (Kaye and Elgar, 1958, Donnelly, 1960, Becker and Kaye, 1962, Snyder, 1962, Schwarz, 1964, Kataoka et al., 1977, Gravas and Martin, 1978, Sorour and Coney, 1979, Takeuchi and Jankowski, 1981, Buhler and Polifke, 1990, Lueptow et al., 1992) were carried out to confirm these numerical results and to find new regimes. Figure 1.9 is Lueptow's results where there were mainly seven flow regimes, including:

1) Taylor vortices

2) Wavy vortices

3) Random wavy vortices

4) Modulated wavy vortices

5) Turbulent modulated wavy vortices

6) Turbulent wavy vortices

7) Turbulent vortices

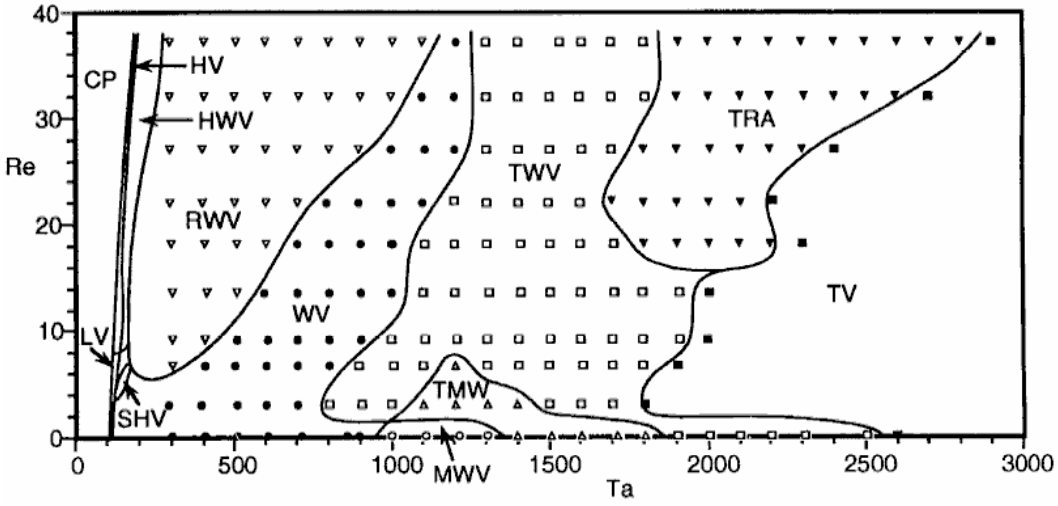

Figure 1.9a Flow regimes for circular Couette flow with an imposed axial flow

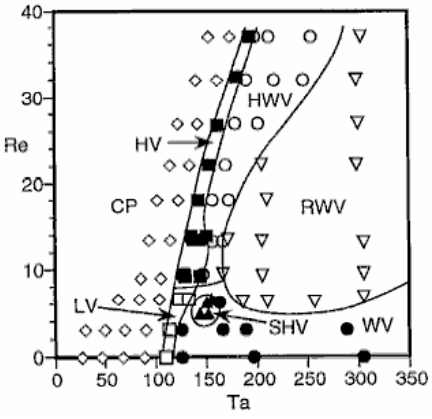

Acronyms for flow regimes.

CP	Couette–Poiseuille flow
HV	Laminar helical vortices
HWV	Laminar helical wavy vortices
LV	Laminar vortices
MWV	Laminar modulated wavy vortices
RWV	Random laminar wavy vortices
SHV	Stationary helical vortices
TMW	Turbulent modulated wavy vortices
TRA	Transitional flow
TV	Turbulent vortices
TWV	Turbulent wavy vortices
WV	Laminar wavy vortices

Figure 1.9b Detail of flow regimes for low Taylor numbers

Figure 1.9 Flow regimes for circular Couette flow with an imposed axial flow (From Lueptow et al., 1992)

The toroidal vortices with the axial flow in these regimes were similar to their counterparts without the axial flow except that the former advanced downstream with the displacement velocity that is about 1.17 times the average axial velocity ((Simmers and Coney, 1980, Gu and Fahidy, 1985, 1986, Haim and Pismen, 1994, Howes and Rudman, 1998).

1.2.4 Application of Taylor-Couette Flow to Photochemical Reaction and UV Disinfection

Kataoka et al. (1975) first proposed that fluid particles entering a Taylor vortex reactor had nearly the same residence times and that the device behaved as a plug flow reactor (PFR). This proposal was confirmed by the analysis of the residence time distribution (RTD) (Pudjiono et al., 1992, Pudjiono and Tavare, 1993). Kataoka et al. (1975) suggested the possibility of using the Taylor vortex system as a chemical reactor when a uniform RTD was required. Moreover, if the inner cylinder is rotating, the large velocity gradient increases heat and mass transfer rates near the surface of the inner cylinder. Cohen and Marom (1983) investigated a Taylor vortex reactor (TVR) for converting isopropanol into acetone. In the latter work, the oxidizing copper catalyst was coated on the inner cylinder for the surface catalytic reaction. Cohen and Marom also found that enhanced heat and mass transfer in the TVR doubled the rate of the isopropanol conversion.

The Taylor vortex reactor (TVR) has also been successfully applied to photochemical reactions (Haim and Pismen, 1994, Sczechowski et al., 1995, Forney and Pierson, 2003b, 2003c, Forney et al., 2005a), polymerization reactions (Xue et al., 2002) and mass transfer (Coeuret and Legrand, 1981, Min et al., 1994, Baier et al., 1998, Baier et al., 1999, Forney et al., 2002a, Park et al., 2004, Park et al., 2006). Recently, fast competitive reactions in Taylor-Couette flow were studied (Forney et al., 2005)

When the fluid in photochemical reactors absorbs radiation, point values of the photochemical reaction rates are intrinsically non-uniform. The major deficiency in photochemical reactor design is inefficient radiation utilization. Low photon-efficiency was reported for many photocatalytical reactions (Turchi et al., 1993). Taylor-Couette flow was introduced to increase the photon-efficiency remarkably in photocatalytical reactions and photolysis (Haim and Pismen,1994, Forney and Pierson, 2003b). Figure 1.10 is the stream function of a Taylor-Couette flow case in the moving frame (1.17 times the average axial velocity) and shows the reason the photon-efficiency is increased . The motion of fluids in Taylor vortex reactors consists of two parts: one is uniform axial movement downstream and the other is revolution around a vortex center. Therefore, in Taylor vortex reactors, fluids have similar residence times and also nearly the same chance of receiving radiation in regions of both high and low fluence rates that provides the possibility of increasing photon-efficiency.

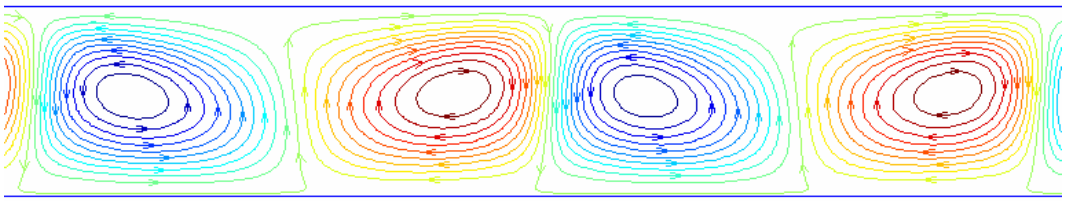

Figure 1.10 Stream function in the moving frame (1.17 times the average axial velocity)

Fluids alternately undergoing high and low radiation areas can also meet some special requirements such as controlled periodic illumination (CPI). For example, Sczechowski et al. (1995) investigated the application of TVR to heterogeneous photocatalysis, in which the main purpose of the vortices was to create a dark recovery time for catalyst particles. Because the photocatalyst particles were periodically illuminated, photon-efficiency was greatly increased.

Haim and Pismen (1994) systematically investigated the application of TVR to homogeneous photochemistry. In their research a first-order photochemical reaction and fluid obeying Lambert-Beer's law were considered. The motivation was to overcome the

effect of the radiation fluence rate gradients inherent in photochemical solutions, which causes concentration gradients. It was shown that the high degree of radial mixing due to the vortices eliminated the concentration gradients created by the radiation fluence rate gradients. The overall rate of reaction increased because the reactant concentration was increased by vortex circulation in the illuminated zone of the reactor. At last it was concluded that the vortices were an effective method for fast reactions in which the fluid strongly attenuated the incoming radiation.

Forney et al. (2002, 2003a, Forney and Pierson, 2003c, 2004) investigated the possibility of applying Taylor-Couette flow to UV disinfection. Their research showed that the inherent property of photochemical reactors, nonuniform fluence distribution, was alleviated to a great degree.

1.3 Computational Fluid Dynamics

Many chemical processes involve fluid flow. The understanding and prediction of the behavior of fluid flow are important from both a theoretical and applied point of view. Although considerable information about fluid flow can be gained via laboratory experiments, these measurements may have several disadvantages:

- They are costly and time consuming,
- The data is limited to a few points in time and space,
- It may be difficult or even impossible to satisfy all dimensionless parameters for experiments,
- If intrusive measurement techniques are used, the actual flow fields are disturbed,
- Some properties are difficult or even impossible to measure experimentally by current technology.

These problems have led to efforts to build mathematical models to describe fluid flow (these models usually consist of a set of partial differential equations) and the development of efficient computer programs to predict the velocity field. For example,

the equations, which describe single phase, incompressible fluid flow, are the Navier-Stokes equations (Bird et al., 2002)

$$\frac{\partial \vec{u}}{\partial t} + \vec{u} \cdot \nabla \vec{u} = -\frac{1}{\rho} \nabla P + \upsilon \nabla^2 \vec{u} \tag{1.9}$$

and continuity equation

$$\nabla \cdot \vec{u} = 0 \tag{1.10}$$

where $\vec{u}$, P, ρ and ν represent velocity, pressure, density and kinematic viscosity respectively. If chemical reaction and species transport are involved, the conservation equations for i^{th} species should be solved simultaneously (Bird et al., 2002).

$$\frac{(\partial \rho Y_i)}{\partial t} + \nabla \cdot (\rho \vec{u} Y_i) = -\nabla \cdot \vec{J}_i + R_i \tag{1.11}$$

where Y_i, J_i, R_i represent mass fraction, diffusion flux and net rate of production of i^{th} species respectively.

The *Navier-Stokes* equations for single phase flow are nonlinear and consist of second-order partial differential equations (PDEs) where no analytic solution exists except for a few special cases. With the significant advances made in both computational algorithms and computer hardware over the past half century, it is possible to obtain numerical solutions at every discrete point with the aid of digital computers. A new science called computational fluid dynamics (CFD) was developed. The aim of CFD is to use numerical techniques to solve the *Navier-Stokes* equations (1.9), the continuity equation (1.10) and the species transport equations (1.11). CFD has now become an indispensable tool for designing and analyzing fluid flow.

Among several commercial CFD software packages which are used to simulate Taylor-Couette flow, FLUENT from Fluent,Inc (Lebanon,NH) is one of the most popular (Baier et al., 1999, Zhu et al., 2000, Zhu et al., 2001, Marchisio et al., 2001). FLUENT will be used to simulate UV disinfection in both turbulent flow and Taylor-Couette flow.

1.4 Objective

The objective of this work is to investigate UV disinfection in thin film annular reactors in laminar Poiseuille flow, turbulent flow and both laminar and turbulent Taylor-Couette flow. The experiments and numerical objectives include:

(1) Measure and fit the UV inactivation rates of *Escherichia coli* (*E. coli*) K12 and *Yersinia pseudotuberculosis* (*Y. pseudotuberculosis*) in order to provide rate expressions necessary in numerical modeling;

(2) Compare UV disinfection in the three flow patterns and suggest proper operating parameters for different flow patterns;

(3) Find the optimum gap width for each flow pattern;

(4) Find a simple correlation formula for each flow pattern. Although UV disinfection levels can be obtained by numerical simulations or experiments, it is desirable to find a simple correlation for log reductions and other parameters such as absorption coefficients.

CHAPTER 2

UV INACTIVATION KINETICS

2.1 Traditional Methods of Measuring UV Inactivation Kinetics

The most important and fundamental parameter in the design of UV reactors used to inactivate pathogens is the inactivation fluence-response behavior, i.e. UV inactivation kinetics. The experimental procedure consists of a quantification of microbial viability in a microbial population exposed to a known UV fluence (Water Environment Federation, 1996). Traditional methods to obtain a known fluence are to apply a collimated beam apparatus to produce radiation that is nearly parallel (Water Environment Federation, 1996). A shallow petri dish can then be placed under the beam and irradiated for a certain time as illustrated in Figure 2.1.

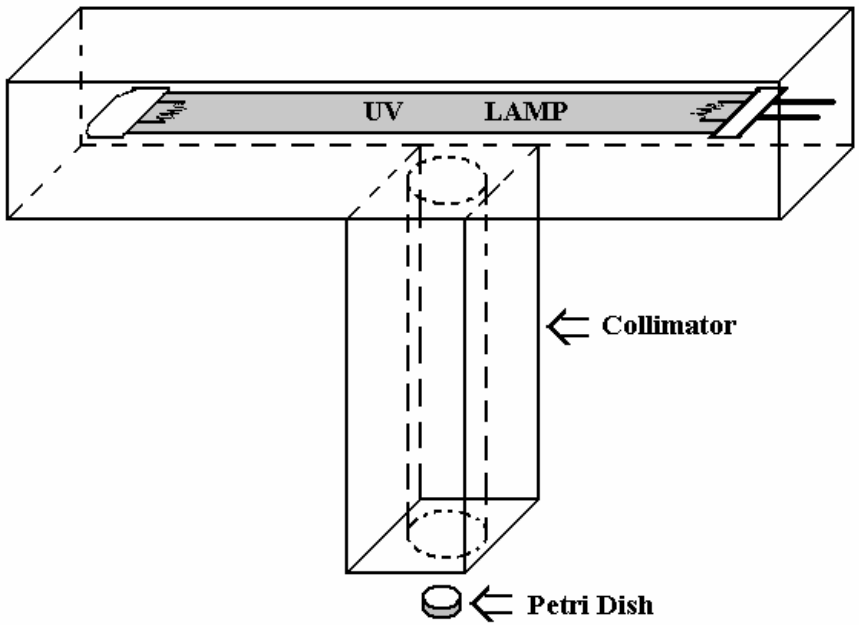

Figure 2.1 Schematic illustration of a collimation apparatus for UV exposure experiments

Since the actual fluence rate within the petri dish decreases from its top surface to the bottom, the local fluence rate may be integrated over the entire fluid depth ($0 \leq x \leq H$) to obtain a depth-averaged fluence rate I_{av},

$$I_{av} = \frac{1}{H}\int_0^H I(x)dx \tag{2.1}$$

The liquid depth is normally 1 cm or less and a micromagnetic stirring bar is applied in order to ensure a uniform fluence distribution. The fluence-response behavior can then be obtained within a certain time or a certain fluence range as illustrated in Figure 2.2. In Figure 2.2, N and N_0 are concentrations of viable microorganisms after and before exposure, respectively. A common unit for the concentration of viable microorganisms is the Colony Forming Unit per milliliter (CFU/mL).

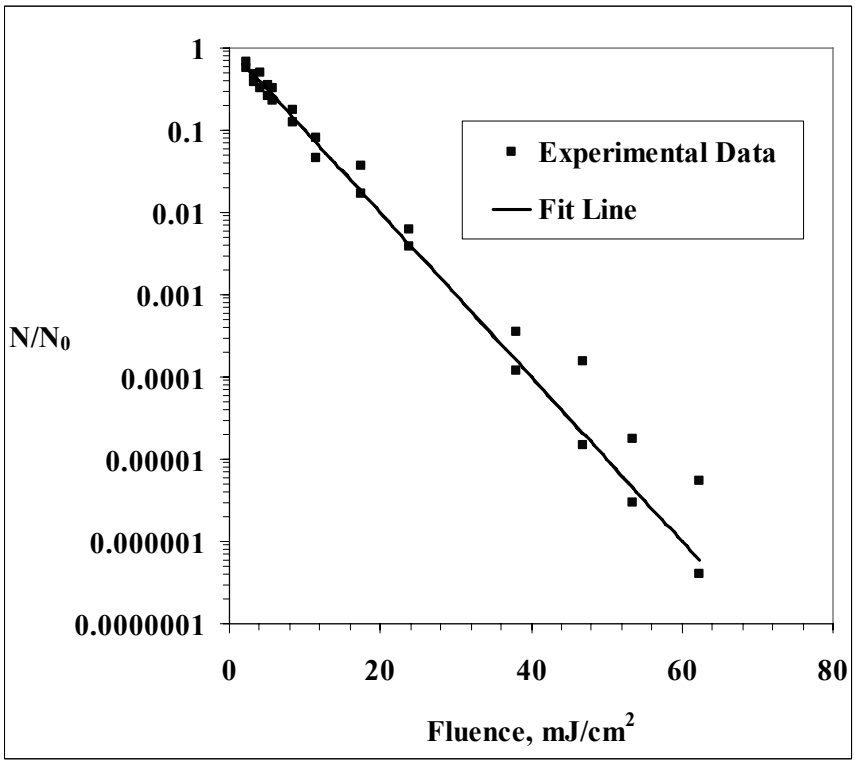

Figure 2.2 Inactivation fluence-response behavior from UV irradiation

It is obvious that the traditional methods require that the UV radiation is parallel and that the fluence distribution is uniform. However, the UV radiation provided by the collimated beam apparatus is only approximately parallel, instead of perfectly parallel. Another disadvantage is that uniform fluence cannot be guaranteed, especially when liquids have high absorption coefficients. Unfortunately, a majority of liquid foods have high absorption coefficients. Because a certain volume of sample is required to

determine the concentration of the sample by a surface plate method, the liquid depth cannot be decreased indefinitely in order to approach a uniform fluence distribution. Although a micromagnetic stirring bar can be applied to approximate a uniform fluence distribution, this creates a non-uniform fluid depth in the petri dish because of the vortex caused by the stirring bar. The non-uniform fluid depth renders equation (2.1) invalid as a means of estimating the depth-averaged fluence rate.

2.2 Theoretical Background of a Novel Method to Measure UV Inactivation Kinetics

In order to overcome the disadvantages of traditional methods, a novel method to measure the inactivation rate is proposed (Ye et al., 2006). In the novel method, a thin-film annular reactor as shown in Figure 1.3 is used to replace a collimated beam apparatus. Fluid was pumped into the reactor through the inlet and flowed through the gap formed by the inner cylinder (quartz sleeve) and the outer cylinder (stainless steel). During the process, the fluid was irradiated and left the reactor through the outlet.

The fluid flow in the radiation section can be approximated as annular Poiseuille flow (see Figure 2.3). After the Navier-Stokes equations of laminar flow for Newtonian fluids are simplified and solved, a velocity profile can be obtained (Bird et al., 2002).

$$u(r) = C_1\left[1 - \frac{r^2}{R_2^2} + \frac{1-\kappa^2}{\ln(1/\kappa)}\ln\left(\frac{r}{R_2}\right)\right]U_{av} \tag{2.2}$$

where

u(r), axial velocity at radius r, cm/s;

U_{av}, average axial velocity, $U_{av} = \dfrac{Q}{\pi(R_2^2 - R_1^2)}$, cm/s;

κ, ratio of the radius of the inner cylinder to that of the outer cylinder, $\kappa = R_1 / R_2$;

C_1, constant determined by κ, $C_1 = \dfrac{2}{\dfrac{1-\kappa^4}{1-\kappa^2} - \dfrac{1-\kappa^2}{\ln(1/\kappa)}}$.

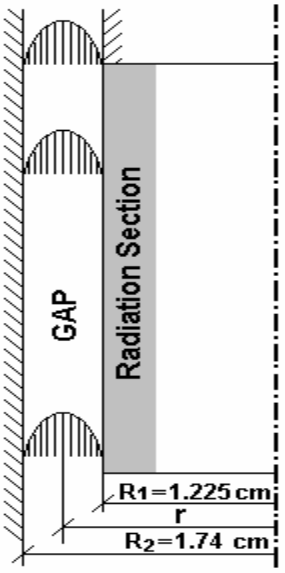

Figure 2.3 Schematic diagram of annular Poiseuille flow

The UV fluence rate in an annular gap can be approximated by Lambert-Beer's law,

$$I(r) = I_0 \frac{R_1}{r} \exp(-\alpha(r - R_1)) \tag{2.3}$$

where

I(r), fluence rate at the radius r, mW/cm^2;

α, absorbance coefficient (e base), cm^{-1}.

Because stream lines of the annular Poiseuille flow are parallel, and axial dispersion and diffusion between neighboring radial layers are negligible, UV fluence *It* (the product of fluence rate *I* and exposure time τ) can be described by the following equation,

$$It(r)=I(r)L/u(r) \tag{2.4}$$

where L is the length of radiation section.

If UV inactivation kinetics is known as a function of fluence *It*,

$$\frac{N}{N_0} = f(\mathrm{It}) \tag{2.5}$$

where N and N_0 are concentrations of viable microorganisms after and before exposure, respectively, the average concentration of viable microorganisms at the outlet of the reactor, N_{av} , can be obtained by integrating:

$$\frac{N_{av}}{N_0} = \frac{\int_0^{2\pi}\int_{R_1}^{R_2} f(\mathrm{It(r)})\mathrm{u(r)rd}\theta\mathrm{dr}}{\int_0^{2\pi}\int_{R_1}^{R_2} \mathrm{u(r)rd}\theta\mathrm{dr}} \tag{2.6}$$

Conversely, because N_{av} can be measured by experiments, parameters in the inactivation kinetics model can be fitted by mathematical methods such as the least squares method. This is the theoretical background of the novel method to measure UV inactivation kinetics.

Compared with traditional methods, neither the collimated beam apparatus nor uniform fluence is required in the novel method. Therefore, the disadvantages of the traditional methods can be overcome. Moreover, since many UV devices in industry are annular continuous flow reactors, the parameters of the inactivation kinetics obtained from the novel method are more reliable and accurate than those obtained from the traditional methods.

The UV inactivation kinetics of two microorganisms, *Escherichia coli* K12 (ATCC 25253) and *Yersinia pseudotuberculosis* (*Y. pseudotuberculosis*), was measured to validate the novel method.

2.3 Models of UV Inactivation Kinetics

2.3.1 First Order Inactivation Model

Many different modeling approaches have been proposed to predict UV inactivation kinetics (Collins and Selleck, 1972, Severin et al., 1983, Kowalski, 2001). Among them, the first order inactivation model is the simplest. It assumes that the inactivation rate changes with respect to pathogen concentration, N, and fluence rate, I, such that

$$\frac{dN}{dt} = -kIN \tag{2.7}$$

where k is first order inactivation constant, cm^2/mJ. It was also defined as pseudo-first order model or mixed second order model in some references (Severin et al., 1983, Chiu et al., 1999). If k and *I* are constant, by integration,

$$\frac{N}{N_0} = \exp(-kIt) \tag{2.8}$$

The first-order model is able to reasonably predict inactivation when the fluence is within certain limits. However, it does not agree well with experiments at low or high fluence (Severin et al., 1984). Sigmoidal shaped inactivation curves are often observed in many experiments (See Figure 2.4, Harris et al., 1987). At first, the first order inactivation constant is small at relatively low fluence. These kinds of phenomena are also referred to as a shouldered survival curve (Harm, 1980). Then, the first order inactivation constant increases with fluence. Finally, when the fluence is larger than a certain value, the first order inactivation constant begins to decrease with the increase in fluence. These kinds of phenomena are also referred to as tailing phenomena.

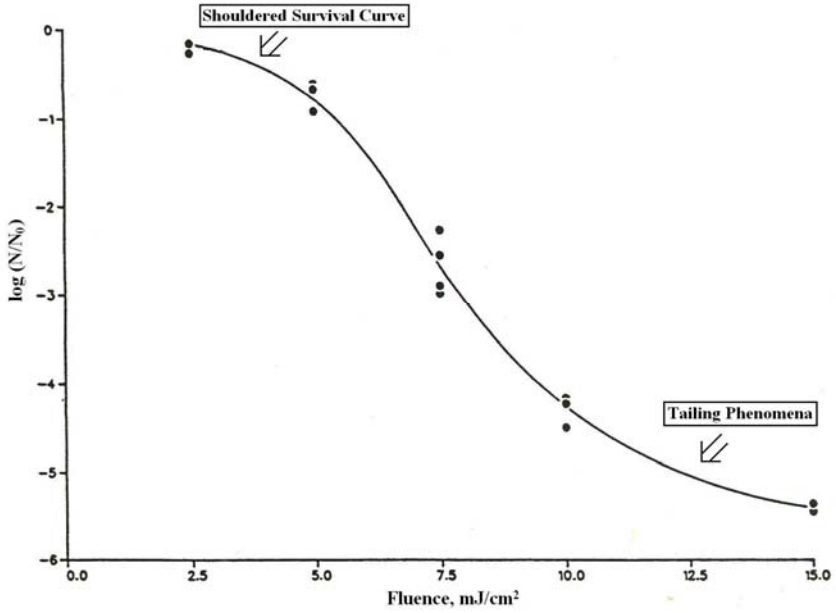

Figure 2.4 Observed deviations from the first order inactivation model (from Harris et al., 1987)

A lag in microbial inactivation at low fluence (the shouldered survival curve) can be observed, perhaps because microorganisms absorbing a sublethal UV fluence may recover and continue multiplying. The sublethal UV fluence had little adverse effect in the analytical procedure to quantify microbial viability. Also, the tailing phenomena (the decline in the slope of the fluence-log reduction curve) at high fluence may be observed. The tailing phenomena may be attributable to the result of heterogeneity among a population of microorganisms. Some organisms may be relatively less resistant to UV radiation while other organisms in the same population may be more resistant. Another reason for the tailing effect is particles such as pulp in juices. Particles may provide a hiding space for a viable organism or an opaque surface to shade microorganisms from UV radiation.

Because the tailing phenomena often begin to appear when the log reductions are larger than 5, it is not very important in real applications of UV disinfection. Other models, for example, multi-target (Severin et al., 1983, Kowalski, 2001), series-event (Severin et al., 1983), the Collins-Selleck model (Collins and Selleck, 1972), were developed to account for deviations from the first-order model at low fluence. Both the first order inactivation model and series-event inactivation model (Severin et al., 1983) were compared in order to improve the correlation of the experimental data.

2.3.2 Series-Event Inactivation Model

As stated before, a lag in microbial inactivation at low fluence can be observed for many kinds of microorganisms. The series-event inactivation model was proposed by Severin et al. (1983) to account for the lag at low fluence. It assumes that inactivation of microorganism elements takes place in a stepwise fashion,

$$M_0 \xrightarrow{kI} M_1 \xrightarrow{kI} \cdots M_i \xrightarrow{kI} \cdots M_{n-1} \xrightarrow{kI} M_n \xrightarrow{kI} \cdots \tag{2.9}$$

The inactivation rate at each step is the first order with respect to the fluence rate I,

$$\frac{dN_i}{dt} = kI(N_{i-1} - N_i) \tag{2.10}$$

where subscript *i* is event level and *k* is the inactivation constant. *k* is assumed to be the same for different event levels. When n elements (a threshold) of microorganisms have been inactivated, the microorganisms will become nonviable. If k and *I* are constant, the concentration of surviving microorganisms N is determined by:

$$\frac{N}{N_0} = \exp(-kIt)\sum_{i=0}^{n-1}\frac{(kIt)^i}{i!} \tag{2.11}$$

where n is a threshold. It is obvious that if n=1, the above equation will be reduced to the first order model.

The physical meaning behind equation (2.11) is that more than one hit is required for UV inactivation of an individual microorganism. At the beginning of UV inactivation (low fluence), the probability of individual microorganism to obtain n hits (where n > 1) is rather low. As the UV inactivation continues, more surviving microorganisms have accumulated n-1 hits and require only one additional hit to be inactivated completely (Harm, 1980) so that the inactivation curve becomes steeper with increasing fluence. Larger threshold values of *n* represent microorganisms that are more resistant at low fluence. Figure 2.5 shows this trend clearly. The inactivation constants in Figure 2.5 were obtained by fitting the same experimental data with different thresholds. At low fluence, the first order model cannot account for the shouldered survival curve and overestimates log reductions. At high fluence, the series event model predicts higher log reductions than the first order model. Moreover, the difference of the log reductions between the first order model and the series event model increases with the fluence and the threshold. The series event and the first order models, however, predict similar log reductions with intermediate fluence values.

The shouldered survival curve can be observed in UV inactivation of many types of microorganisms. The first order model (n=1) is valid only for some viruses whose

sensitive material is single-stranded DNA or single-stranded RNA (Harm, 1980). Figure 2.6 is one example (Severin et al., 1984), where n=1 for f2 bacterial virus.

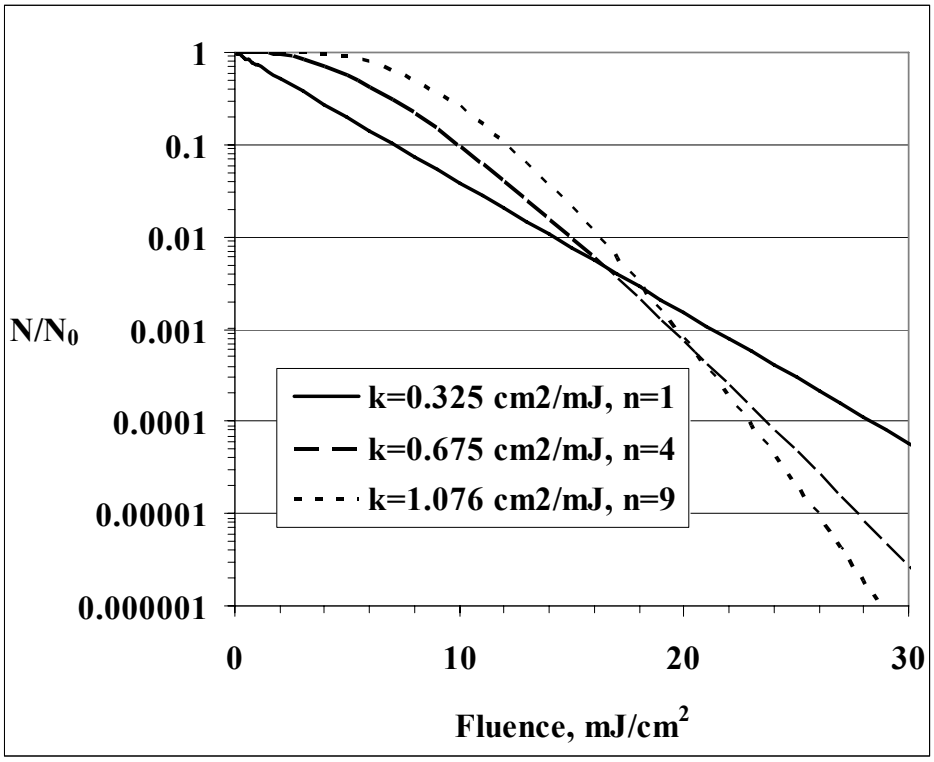

Figure 2.5 Log reductions with different thresholds

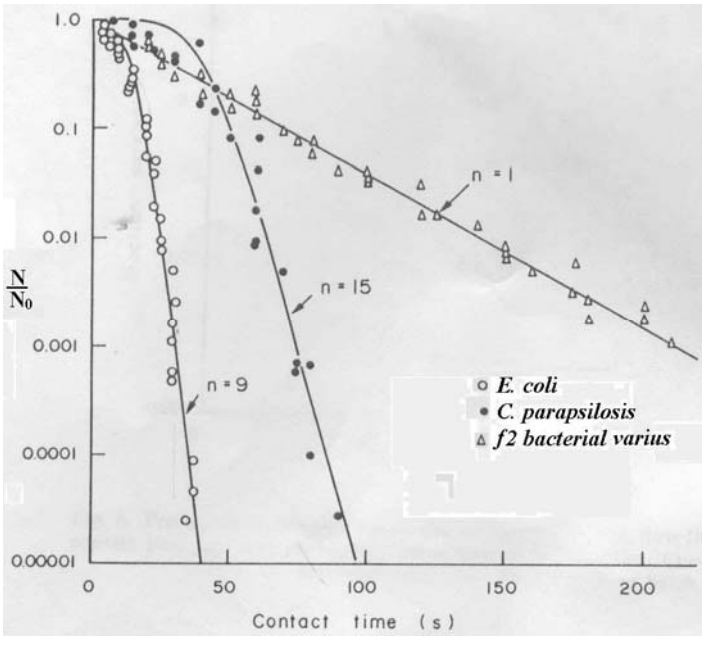

Figure 2.6 Batch inactivation data; analysis with series-event model (From Severin et al., 1984)

2.4 UV Inactivation Kinetics of *E. Coli*

2.4.1 Materials and Methods

Model Solutions

Model caramel solutions (Koutchma and Parisi, 2004a, Koutchma et al., 2004b) were used to simulate absorptive properties of juices and to study the effect of absorbance on UV inactivation. The base for the model system was a 0.025 M sodium malate buffer (Fisher Scientific, Hanover Park, IL) at pH 3.5. Caramel (Pepsi Cola Co, NY) was used in the range of concentrations from 0.04% to 0.2%. Correspondingly, absorption coefficients varied from about 2.4 cm^{-1} to 12 cm^{-1}.

UV-Treatment Configurations

The thin-film annular reactor used in the study was an UltraDynamics model TF-1535 (Severn Trent Services Inc., Colmar, PA). The system included a UV lamp, protective quartz sleeve and a remote power supply for 120/220 Vac 50/60 Hz operation with a built-in lamp failure indicator. The single low pressure, germicidal UV lamp was positioned in a 316L stainless steel reactor vessel. The outer diameter of the quartz sleeve was 2.45cm and the inner diameter of the stainless steel tube was 3.48cm. Correspondingly, the gap formed by the two cylinders was 0.515cm wide.

The schematic diagram of the UV-treatment system used in the experiments is shown in Figure 2.7. The whole system consisted of 3 chambers with various lengths of 80cm, 40cm and 20cm. All three single-bulb UV reactors were used in the study. Each reactor was mounted in the vertical position with the fluid flowing from the bottom to the top in order to fill the annular gap fully and avoid bubbles. Samples for microbial analysis were taken after steady state conditions were reached with the UV lamps and flow conditions. The flow rate of the pump varied from 3 to 37 ml/s and was controlled

by the shielded flow meter. Correspondingly, the average residence time varied from 1.5 to 135 seconds.

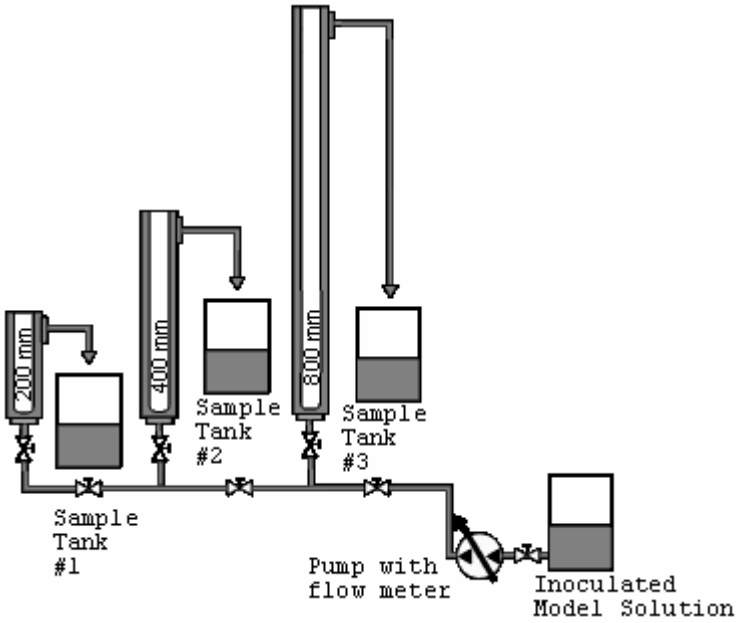

Figure 2.7 Schematic diagram of the UV-treatment system

Test Microorganism and Microbiological Analysis

Because *E. coli* K12 (ATCC 25253) is nonpathogenic and its UV sensitivity is not notably different from E. coli O157:H7:960218 (from the Osaka, Japan outbreak) (Koutchma 2004b), *E. coli* K12 was chosen as a target microorganism. The starting culture was adapted to malic acid (Swanson et al., 1985, Miller and Kaspar, 1994). Bacteria were grown for 18 hours in tryptic soy broth (TSB, Difco Fisher Scientific, Hanover Park, IL) and first adjusted to pH 5.5 at 37^{o}C with malic acid. One milliliter of culture adapted to pH 5.5 was added to TSB adjusted to pH 4.5 and incubated for 18 hours. The UV sensitivity of acid adapted bacteria to pH 4.5 and non-pH adapted cells were compared.

Stock cultures were maintained at 4^{o}C on tryptic soy agar (TSA) (Difco, Fisher Scientific, Hanover Park, IL). Cultures were grown for 18 hours in TSB with 0.75% glucose in 250 ml Erylenmyer flasks at 37^{o}C. Stationary phase cultures typically reached

a final concentration of approximately 10^9 CFU/ml. Cells were harvested by centrifuging at 500 rpm and washing with 0.1% peptone water prior to inoculation to yield an initial level of concentration about 10^6 -10^7 CFU/ml. For inoculation to model solutions at a final concentration of 10^6 CFU/ml, culture was added directly without prior harvesting or washing. For enumeration, appropriate dilutions were made with 0.1% peptone water and surface plated in duplicate on TSA. Plates were incubated for 24-30 hours at 37^{o}C and counted.

Absorbance Measurements

Absorbance of model caramel solutions was measured at 254 nm by a spectrophotometer GENESYS™ 6 (Thermo Spectronic, Rochester, NY). Because absorbance of most of the sample solutions was out of the range of the spectrophotometer (maximum measurable value is 3 or 4) if standard 1-cm cuvettes were used, matched demountable fused quartz cuvettes (NSG Precision Cells Inc., NJ) with path length of 1.0, 0.5, 0.2 and 0.1 mm were used. Each solution was measured four times or more and averaged. The absorption coefficient of the solution was determined from the slope of the absorbance versus the path length (Koutchma and Parisi, 2004a).

Measurements of UV Radiation Fluence rate on the Surface of UV Lamps

After the UV lamps were turned on for 10 minutes, an IL 1700 Research Radiometer equipped with an SUD240 detector (International Light, Inc., Newburyport, MA) was used to measure the radiation fluence rate of the UV lamps. The radiation fluence rate was measured along the whole length of the UV lamp and averaged.

For the reactors with lengths of 80cm, 40cm and 20cm, the average fluence rate on the surface of the quartz sleeves was measured to be 12, 16 and 15.4 mW/cm^2 respectively, and the effective radiation lengths were 77.9cm, 29.2cm and 11.2cm respectively. For the 80cm reactor, UV output claimed by the manufacturer was 13.8 W.

According to this output, the average radiation fluence rate should be 23 mW/cm^2, which was almost twice as much as the measured value. However, the manufacturer tested the output at 1 meter away from the lamp and guaranteed it was more than 0.12 mW/cm^2. From this, average radiation fluence rate on the surface of the quartz sleeve was inferred to be more than 9.8 mW/cm^2. It appeared that the measured values were more reliable, so they were used in the following calculations.

2.4.2 First Order Inactivation Model

The inactivation constant in the first order inactivation model can be obtained by the least squares method. The purpose of the least squares method is to find the inactivation constant k in the equation (2.7) that minimizes the sum of the squares of the deviations (SD) between logarithm reduction values fitted from the equation and the experimental values

$$SD = \sum \left[\log\left(\frac{N_{av}}{N_0}\right)_{fit} - \log\left(\frac{N_{av}}{N_0}\right)_{\exp} \right]^2 \tag{2.12}$$

Figure 2.8 is the first order inactivation rate constant of *E. coli* fitted according to different absorption coefficients A (10 base absorption coefficient, A=ln(10)α), where R^2 is the coefficient of determination, σ_y the standard deviation of log reductions, I_0 incident fluence rate and τ_{av} average residence time. N is the average *E. coli* concentration after UV exposure, and will be used instead of N_{av} for the sake of brevity.

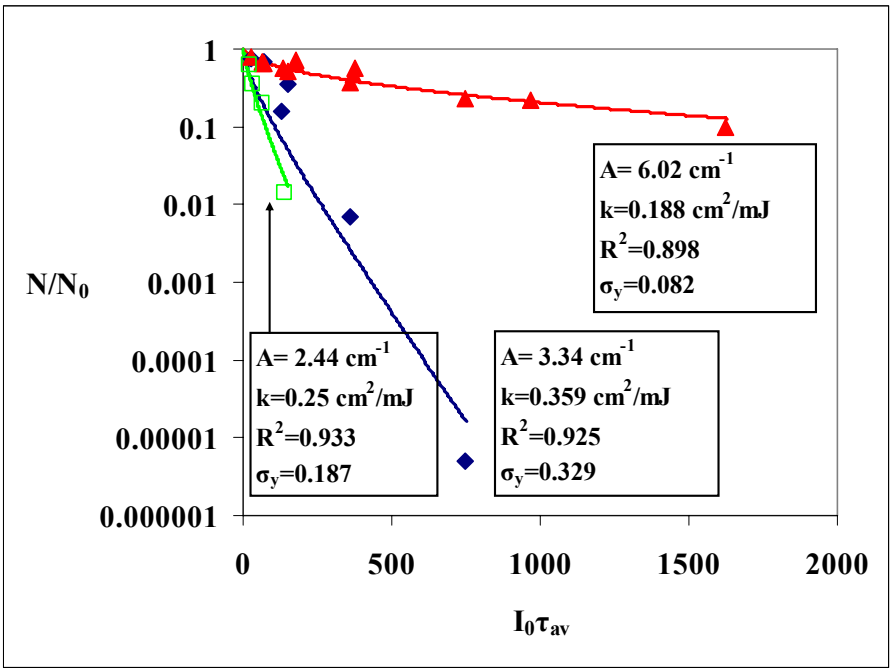

Figure 2.8 First order inactivation constants of *E. coli* with different absorption coefficients

Theoretically, the inactivation constant k is independent of the absorption coefficient. However, it is shown in Figure 2.8 that the inactivation constant k depends on the absorption coefficient. These results are due to the low log reduction level and shouldered survival curve of *E. coli*. When most of the *E. coli* receives low fluence and the log reduction level is low (curve A=6.02 cm^{-1} and curve A=2.44 cm^{-1}), the first order model gives a small inactivation constant. On the other hand, the first order model gives a large inactivation constant when the log reduction level is high (curve A=3.34 cm^{-1}).

After 38 experimental points were fitted by the first order inactivation model, the values of the inactivation constant k=0.32494 cm^2/mJ with R^2= 0.907 and σ_y=0.354 were obtained. Figure 2.9 is the comparison of *E. coli* log reductions between experiments and fitted data with the first order inactivation model. Because the experiments were done in different reactors (correspondingly different incident fluence rates) with different absorption coefficients, different inactivation levels were obtained for the same average residence time. The maximum absolute error of log reduction is 0.9285 when the log

reduction is 5.3. The maximum relative error of the log reduction is 277% when the log reduction is 0.1745. Because of the shouldered survival curve of *E. coli*, the first order model overestimates inactivation at low log reduction and underestimates inactivation at high log reduction.

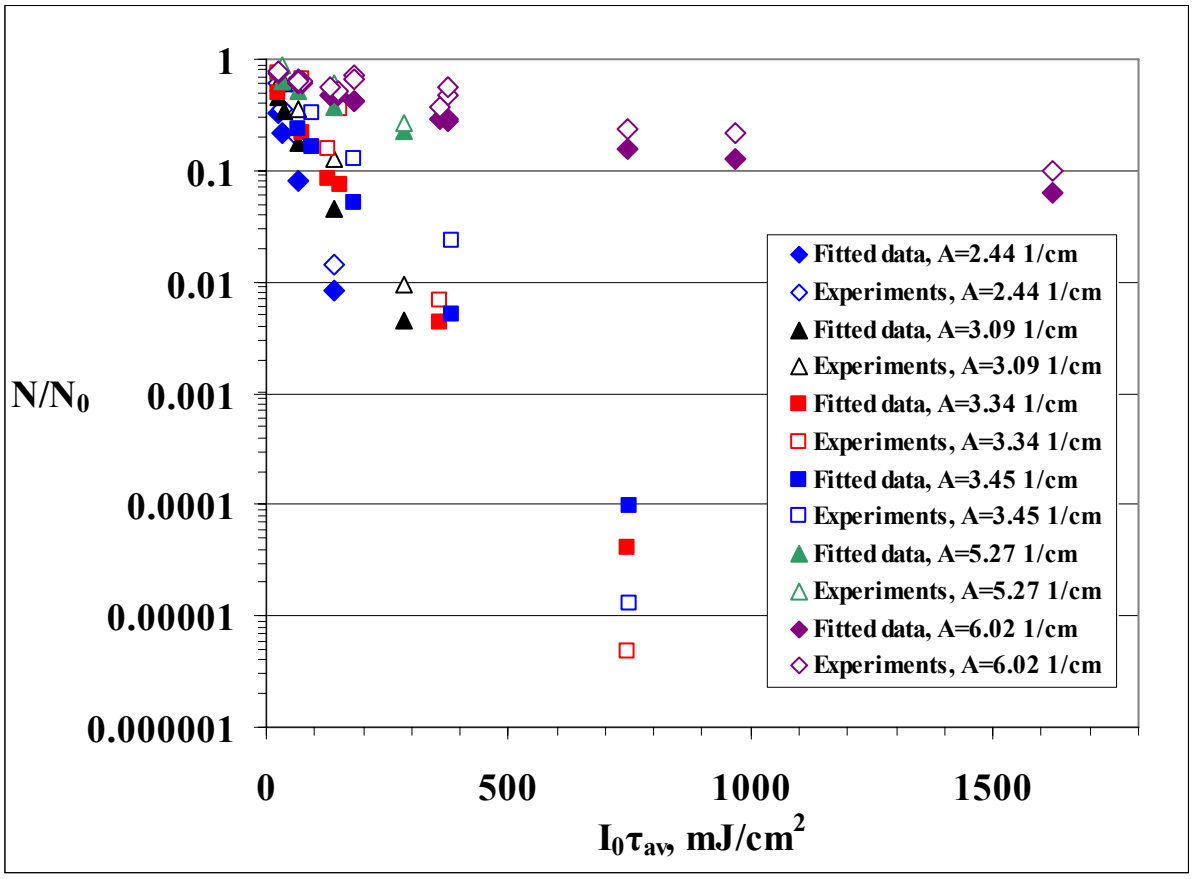

Figure 2.9 Comparison of *E. coli* log reductions between experiments and fitted data with the first order inactivation model

The fluence required for 90% inactivation of *E. coli* with the first order inactivation model is reported in some references (see Table 2.1). No names of strains were revealed and water or wastewater was used in most references. Because of different strains and culturing conditions, it was common that the first order inactivation constants measured by different authors were not the same. It was reported by Koutchma et al. (2004b) that *E. coli* K12 (ATCC 25253) had a lower inactivation rate than *E. coli*

O157:H7 (DHS1) and *E. coli* O157:H7 (H3482). The measured value, k=0.325 cm^2/mJ, is similar to the latest value (k=0.371-0.658 cm^2/mJ), and it is within a reasonable range.

Table 2.1 Reported inactivation constant of *E. coli*

Fluence required for 90% inactivation, mJ/cm^2	First order inactivation constant, cm^2/mJ	Reference
=	0.893	Severin et al., 1984
3	0.77	Wolfe, 1990
3.2	0.72	Cairns, 1991
1.33	1.73	Wilson et al., 1992
3.5-6.2	0.371-0.658	Taghipour, 2004

2.4.3 Series-Event Inactivation Model

As stated before, the first order model overestimates inactivation at low log reduction and underestimates inactivation at high log reduction. Figure 2.10 shows the inactivation constants of *E. coli* fitted with the series-event model according to different absorption coefficients, where n is the threshold value.

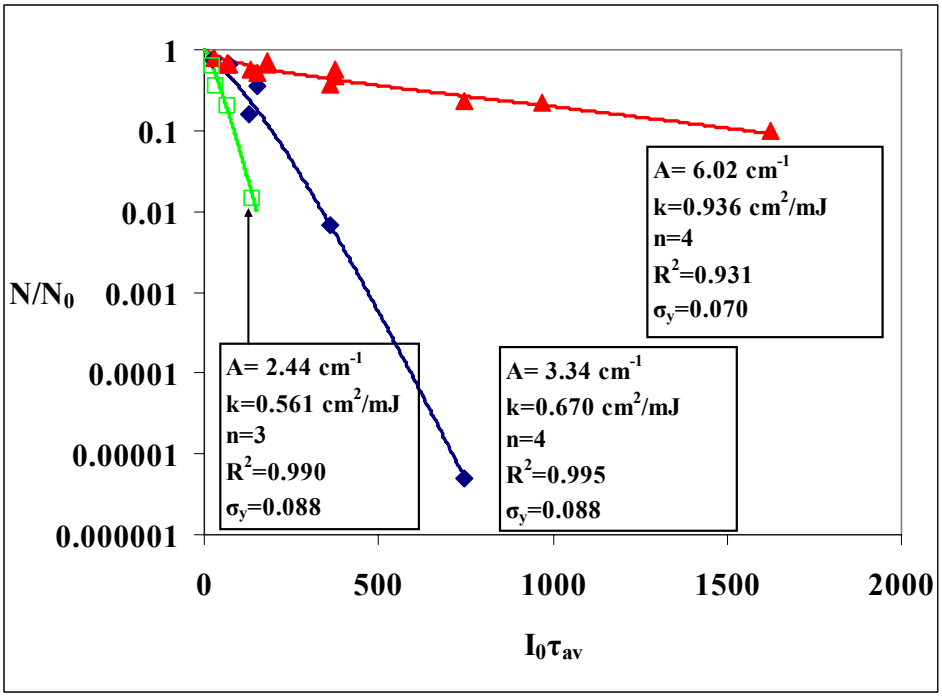

Figure 2.10 Inactivation constants of the series-event model of *E. coli* with different absorption coefficients

In Figure 2.10, k=0.693 cm^2/mJ with R^2=0.987 and σ_y=0.128 were obtained if n=4 was used to fit the data of A=2.44 cm^{-1}. Different absorption coefficients give similar inactivation constants. On the contrary, the first order model gives different inactivation constants for different absorption coefficients.

After 38 experimental points were fitted by the series-event inactivation model, the values of inactivation constant k=0.67474 cm^2/mJ and threshold n=4 with R^2=0.987 and σ_y=0.133 were obtained. In contrast, values of k=1.538 cm^2/mJ and threshold n=9 with R^2=0.967 were reported by Severin et al. (1983). If the experimental data were fitted with the threshold n=9, k=1.076 cm^2/mJ with R^2=0.96 and σ_y=0.237 were obtained and the inactivation constant was similar to Severin's data (Severin et al., 1983) when n=9.

Figure 2.11 is the comparison of *E. coli* log reductions between experiments and fitted data with the series-event inactivation model. The maximum absolute error of log reduction is 0.434 when the log reduction is 2.1. The maximum relative error of log reduction is 72.5% when the log reduction is 0.1745.

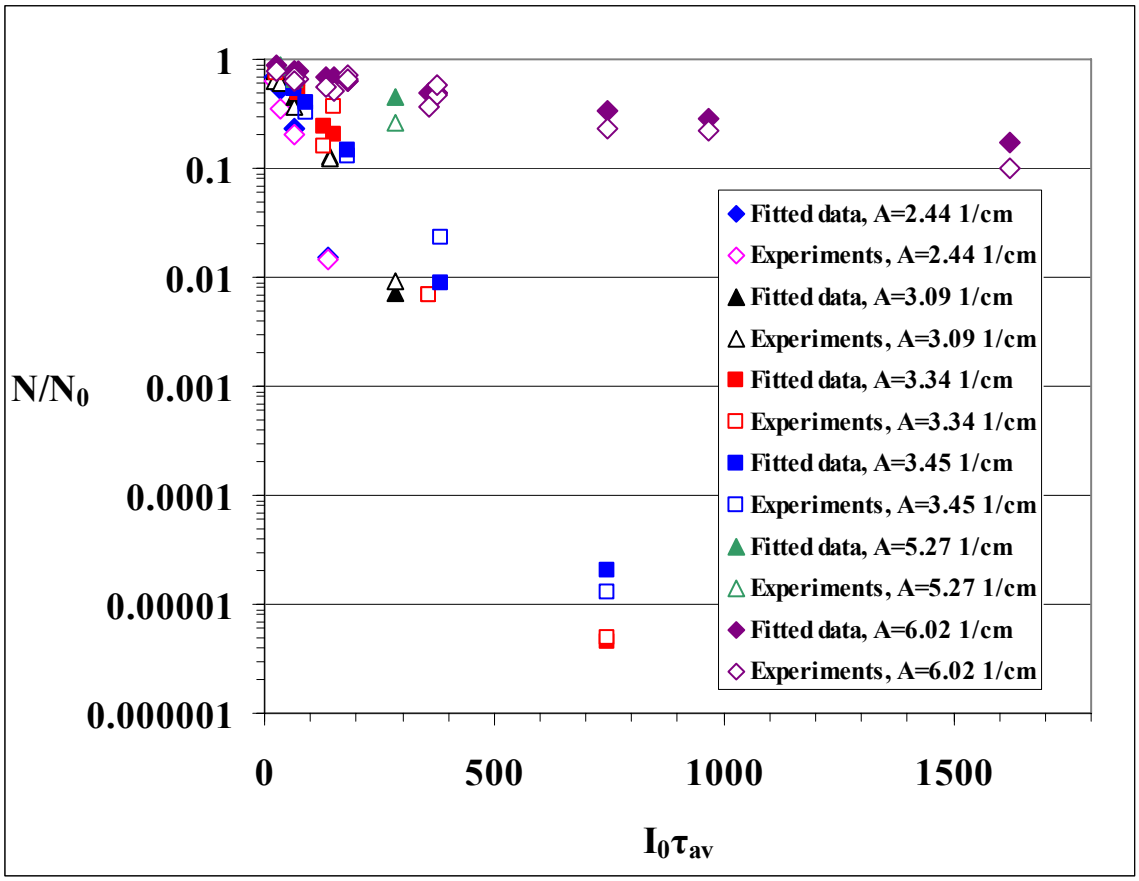

Figure 2.11 Comparison of *E. coli* log reductions between experiments and fitted data with the series-event inactivation model

It is found that compared with the first order inactivation model, the series-event inactivation model is better suited to fit the experimental data of *E. coli* K12. The R^2 is increased from 0.907 to 0.987 and the σ_y is decreased from 0.354 to 0.133. Both the maximum absolute error and maximum relative error are decreased. The reason is that the fluence distribution is so broad that it includes both low and high fluence, especially when absorption coefficients of the fluids are high. Therefore, deviation from the first-order model has to be accounted for.

2.5 UV Inactivation Kinetics of *Y. pseudotuberculosis*

In recent years, the threat of attacks on a nation's food supply by terrorists or other hostile individuals has forced the food industry to examine the effect of food

processing methods on uncommon pathogens. *Yersinia* species are examples of such pathogens. No studies have been conducted to show that commercial UV treatment systems can inactivate *Y. pseudotuberculosis*, one of the *Yersinia* species.

Y. pseudotuberculosis is a gram-negative rod-shaped coccobacillus belonging to the family *Enterobacteriaceae* (Bioinformatics Educational Resource, 2006). Although *Y. pseudotuberculosis* is the least common of the three main *Yersinia* species including *Yersinia pestis* and *Yersinia enterocolitica* to cause infections in humans, *Y. pseudotuberculosis* is widely present in the environment (soil, water, vegetables, etc), and human infections transmitted via contaminated water and foods are highly possible. No foodborne outbreaks caused by *Y. pseudotuberculosis* have been reported in the United States (FDA/CFSAN, 2005). However, it was reported in Okayama, Japan in 1991 that children were exposed to *Y. pseudotuberculosis* because of the consumption of untreated drinking water. Four laboratory-confirmed cases of *Y. pseudotuberculosis* were reported in British Columbia, Canada in November 1998 (Canada Communicable Disease Report, 1999). Other cases were also reported in European countries.

2.5.1 Materials and Methods

Since the materials and methods used to measure the inactivation kinetics of *Y. pseudotuberculosis* were similar to those used for *E. coli*, the test microorganism and microbiological analysis that is unique to the former is described below.

Test Microorganism and Microbiological Analysis

Inoculum preparation

From refrigerated stock (streak plate) an isolated colony of *Y. pseudotuberculosis* (Obtained from The Center for Food Safety and Applied Nutrition, U.S. FDA) was selected and aseptically transferred to 100 mL of brain-heart infusion (BHI, Becton Dickinson, Franklin Lakes, NJ) in a 500 mL baffled flask. This culture was incubated

with shaking at 25 ^{o}C for approximately 24 hours. Good growth was observed at the end of incubation. Culture pH was measured with pH paper and found to be approximately 7.0.

Ten grams of D-glucose was dissolved in 90 mL deionized water and filter sterilized to produce a 10% glucose solution. Ten mL of this solution was aseptically transferred to 90 mL BHI in a 500 mL baffled culture flask. The result was BHI with 1% glucose.

One mL of the previous culture was aseptically transferred to the BHI with 1% glucose. The resulting culture was incubated at 25 ^{o}C with shaking for about 16 hours (overnight). At the end of incubation a sample of the culture was aseptically withdrawn and tested with pH paper. The pH was found to be approximately 5.0. The culture typically reached a final concentration of approximately 10^{9} CFU/ml.

Inoculation and enumeration

When inoculating juice or water to a final concentration of 10^{6} CFU/ml, culture was added directly without prior harvesting or washing. For enumeration, appropriate dilutions were made with 0.1% peptone water and surface plated in duplicate on BHI plates. The plates were incubated for 48 hours at 25^{o}C and counted.

2.5.2 First Order Inactivation Model

After 19 experimental points were fitted by the first order inactivation model, the values of the inactivation constant k= 0.557 cm^{2}/mJ with R^{2}= 0.916 and σ_{y} =0.402 were obtained. Figure 2.12 is the comparison of *Y. pseudotuberculosis* log reductions between experiments and fitted data with the first order inactivation model. The maximum absolute error of log reduction is 1.19 when the log reduction is 4.9. The maximum relative error of log reduction is 124% when the log reduction is 0.41.

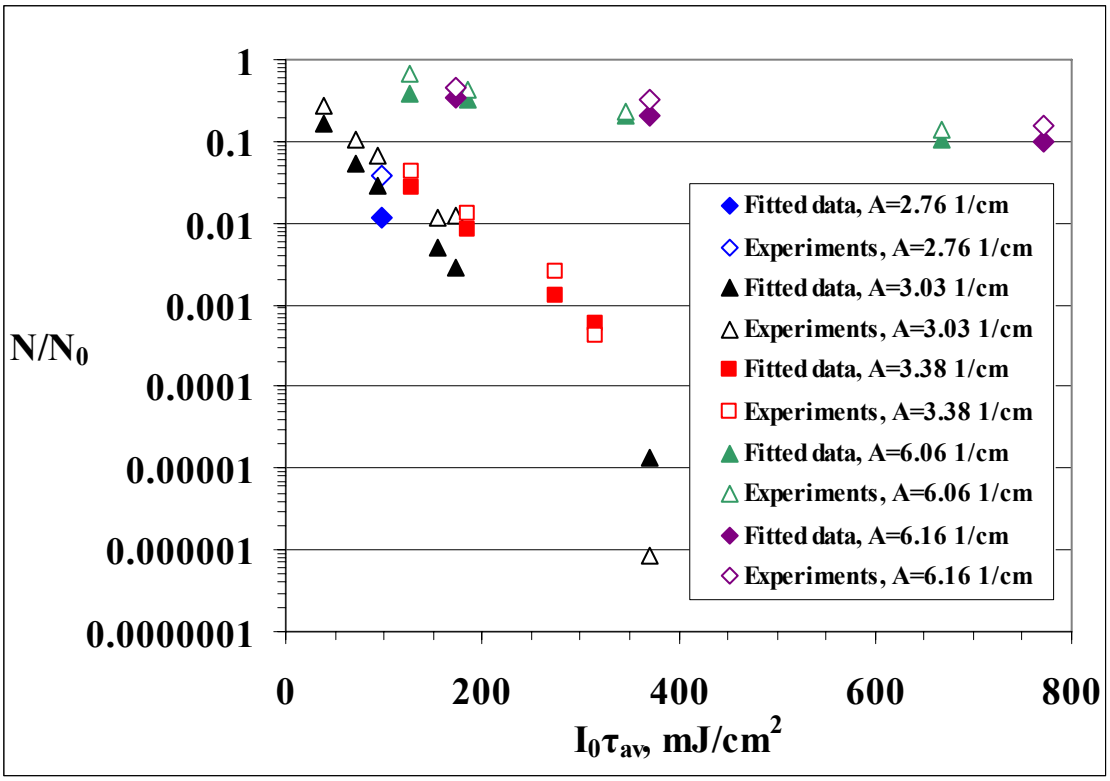

Figure 2.12 Comparison of *Y. pseudotuberculosis* log reductions between experiments and fitted data with the first order inactivation model

No UV inactivation data of *Y. pseudotuberculosis* have been reported in any references. The fluence required for 90% inactivation of *Yersinia enterocolitica*, one of three main *Yersinia* species, with the first order inactivation model is reported in Table 2.2. It shows that the first order inactivation constant of *Y. pseudotuberculosis* is the same order as that of *Yersinia enterocolitica*.

Table 2.2 Reported UV decimal reduction fluence of *Yersinia enterocolitica*

Medium	Fluence required for 90% inactivation, mJ/cm^2	First order inactivation constant, cm^2/mJ	Reference
Drinking water	1.07	2.15	Wilson et al., 1992
N/A	0.921	2.5	Hoyer, 1998
Eggshell surface	7,647-3,342	=	Favier et al., 2001

The inactivation rate of *E. coli* K12 (ATCC 25253) was measured in the same reactors by the same method. The first order inactivation constant k=0.325 cm^2/mJ with R^2= 0.907 was obtained. These results show that *Y. pseudotuberculosis* is less resistant to UV than *E. coli* K12.

2.5.3 Series-Event Inactivation Model

After 19 experimental points were fitted by the series-event inactivation model, the values of the inactivation constant k=0.984 cm^2/mJ and threshold n=3 with R^2=0.972 and σ_y =0.212 were obtained. Figure 2.13 is the comparison of *Y. pseudotuberculosis* log reductions between experiments and fitted data with the series-event inactivation model. The maximum absolute error of log reduction is 0.6 when the log reduction is 2.5. The maximum relative error of log reduction is 34 .1% when the log reduction is 0.24.

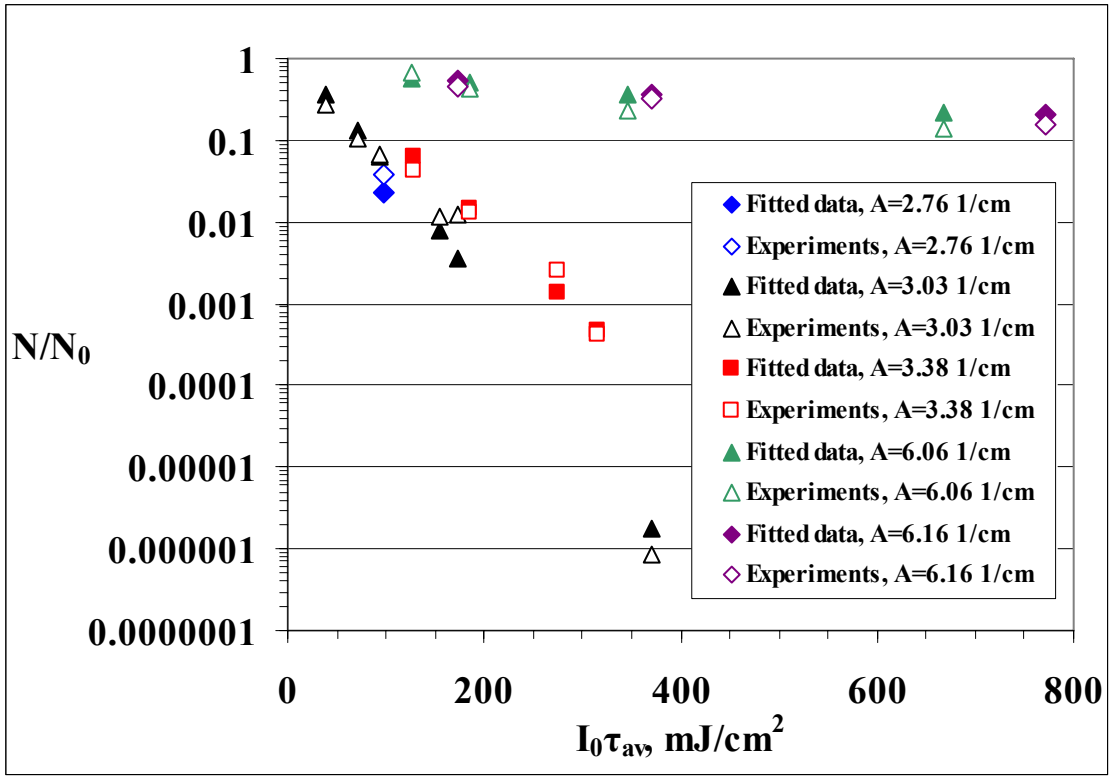

Figure 2.13 Comparison of *Y. pseudotuberculosis* log reductions between experiments and fitted data with the series-event inactivation model

It is found that the series-event inactivation model is better suited to fit experimental data of *Y. pseudotuberculosis* than the first order inactivation model. The R^2 is increased from 0.916 to 0.927 and the σ_y is decreased from 0.402 to 0.212. Both the maximum absolute error and maximum relative error decrease. Like *E. coli*, the possible reason is still the broad distribution of UV fluence that includes both low and high fluence especially when fluids have high absorption coefficients. Deviation from the first-order model, mainly due to the lag in microbial recovery exposed to low UV fluence, has to be accounted for. Figure 2.14 shows colonies of *Y. pseudotuberculosis* incubated for 48 hours for enumeration. It is obvious that colonies are different in size. The possible reason is that sublethally injured cells of *Y. pseudotuberculosis* may recover and multiply slower.

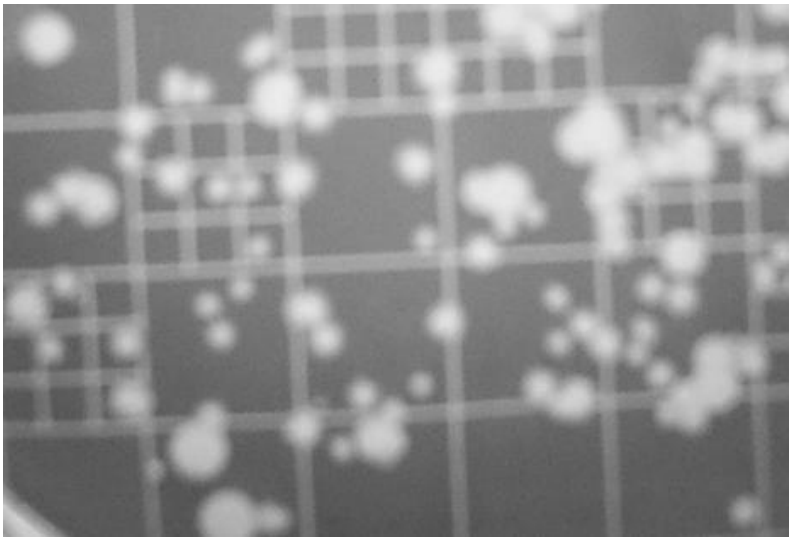

Figure 2.14 Colonies of *Y. pseudotuberculosis* incubated for 48 hours for enumeration

2.6 Conclusions

1. A novel method to measure inactivation kinetics with a thin-film annular reactor is proposed. The method can overcome the disadvantages of traditional methods for highly absorptive liquids. Moreover, since many UV devices in industry are

continuous flow annular reactors, the parameters of inactivation kinetics obtained from the novel method are more reliable and accurate than those obtained by the traditional methods.

2. Compared with the first order inactivation model, the series-event inactivation model is better suited to fit experimental UV inactivation data of *E. coli* K12 and *Y. pseudotuberculosis*.
3. After fitting experimental UV inactivation data of *E. coli* K12 with the series-event inactivation model, the values of k=0.67474 cm^2/mJ and threshold n=4 with the coefficient of determination R^2=0.987 and the standard deviation σ_y=0.133 were obtained compared to a value of k=0.32494 cm^2/mJ with R^2= 0.907 and σ_y=0.354 for the first order inactivation model.
4. After fitting experimental UV inactivation data of *Y. pseudotuberculosis* with the series-event inactivation model, the values of k=0.984 cm^2/mJ and threshold n=3 with the coefficient of determination R^2=0.972 and the standard deviation σ_y=0.212 were obtained compared to a value of k=0.557 cm^2/mJ with R^2= 0.916 and σ_y=0.402 for the first order inactivation model.

CHAPTER 3

UV DISINFECTION IN LAMINAR REACTORS

3.1 UV Fluence Distribution

The UV fluence profile along the gap of one reactor for the UltraDynamics model TF-1535 described in Section 2.4 was investigated. The outer diameter of the quartz sleeve was 2.45 cm and the inner diameter of the stainless steel tube was 3.48 cm. The single low pressure, germicidal UV lamp was 77.9 cm long.

After the velocity profile, equation (2.2), and the fluence rate profile, equation (2.3), are substituted into equation (2.4), the UV fluence profile at the outlet is calculated from equation (3.1),

$$It(r) = I_0 \frac{L}{U_{av}} \frac{R_1}{r} \exp(-\alpha(r - R_1)) \frac{1}{C_1\left[1 - \frac{r^2}{R_2^2} + \frac{1-\kappa^2}{\ln(1/\kappa)} \ln\left(\frac{r}{R_2}\right)\right]} \tag{3.1}$$

Figure 3.1 is the UV fluence profile when the absorption coefficient equals 3 cm^{-1} and the flow rates range from 3 to 37 mL/s corresponding to a Reynolds number range $69 < Re < 854$. Figure 3.2 is the UV fluence profile when the flow rate equals 12 mL/s and the absorption coefficients range from 0 to 12 cm^{-1}. Figures 3.1 and 3.2 show that the UV fluence varies from roughly 10^{-3} mJ/cm^2 to 10^5 mJ/cm^2. Because UV is irradiated from the inner cylinder, the combination of high fluence rate and long residence time leads to high fluence near the inner cylinder. With increasing distance from the inner cylinder, the combination of decreasing fluence rate and residence time results in a gradual decrease in fluence. After $(r- R_1)/(R_2- R_1) > 0.5$, the residence time begin to lengthen. Correspondingly, the decreasing rate of fluence becomes slow. However, if the absorption coefficients of juices are high, e. g., A=12 cm^{-1} in Figure 3.2, the decreasing fluence rate is more important than longer residence times so that the decreasing rate of fluence is hardly affected by the residence time distribution. As expected, the lowest

fluence is not the position with the shortest residence time ($(r- R_1)/(R_2- R_1) \approx 0.5$) or the farthest position from the radiation source ($r = R_2$), and rather somewhere near the outer cylinder.

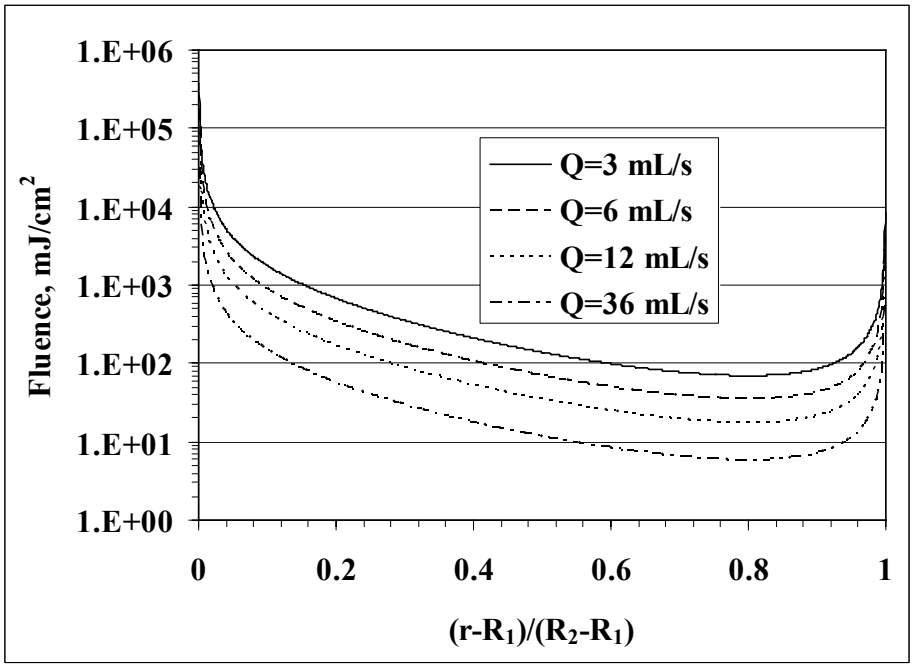

Figure 3.1 UV fluence profile with different flow rates and A=3 cm^{-1}

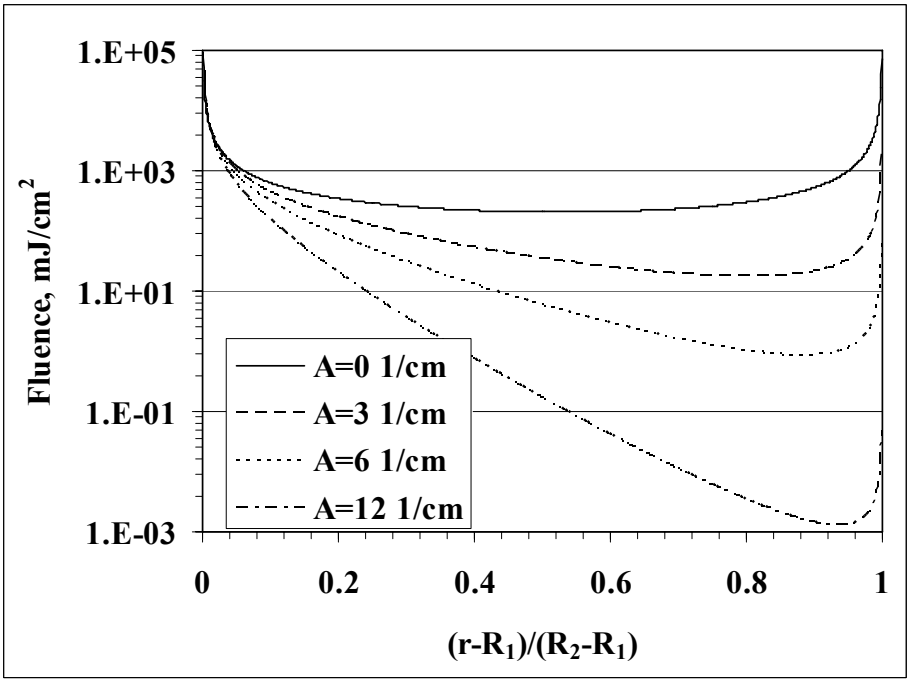

Figure 3.2 UV fluence profile with different absorption coefficients and Q=12 mL/s

The UV fluence profile can be processed further to generate the UV fluence distribution function. The definition of the fluence distribution function is similar to that of the age distribution function (Froment and Bischoff, 1990). The age distribution function is defined as the fraction of fluids leaving the reactor that has residence time of (t, $t+dt$). Because the UV fluence distribution is so broad for photochemical reactors, the fluence distribution function has to be defined as the fraction of fluids leaving the reactor that has fluence of ($logIt$, $logIt+d(logIt)$) instead of (It, $It+d(It)$). Thus, one defines

$$E(logIt)d(logIt) = \text{Fraction of fluids leaving reactor that has fluence of (logIt, logIt+d(logIt))} \quad (3.2)$$

The fluence distribution function in Figures 3.3 and 3.4 corresponds to the fluence profile in Figures 3.1 and 3.2, respectively. Compared with the fluence profile, the fluence distribution function clearly demonstrates the effect of flow rates and absorption coefficients on the fluence.

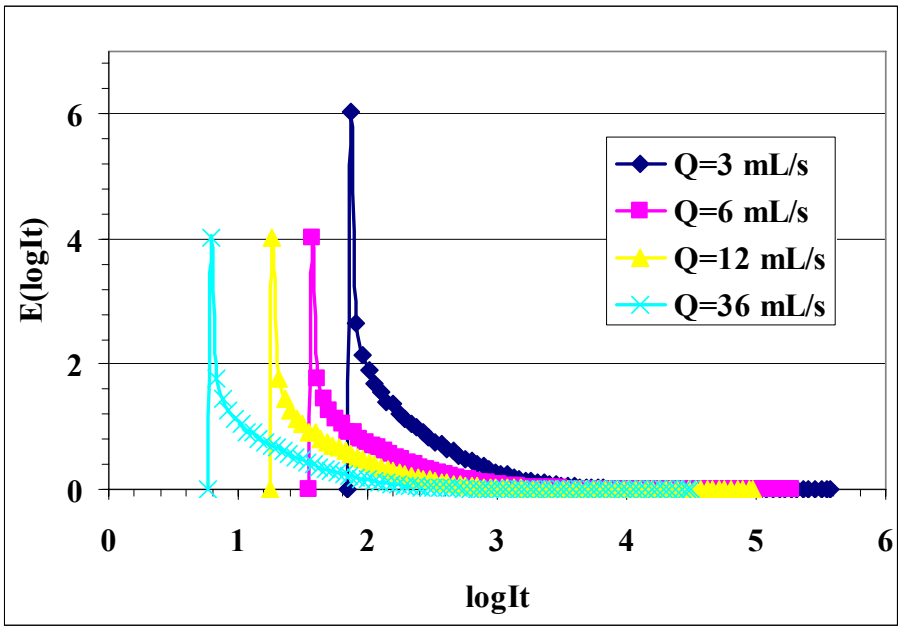

Figure 3.3 UV fluence distribution function with different flow rates and A=3 cm^{-1}

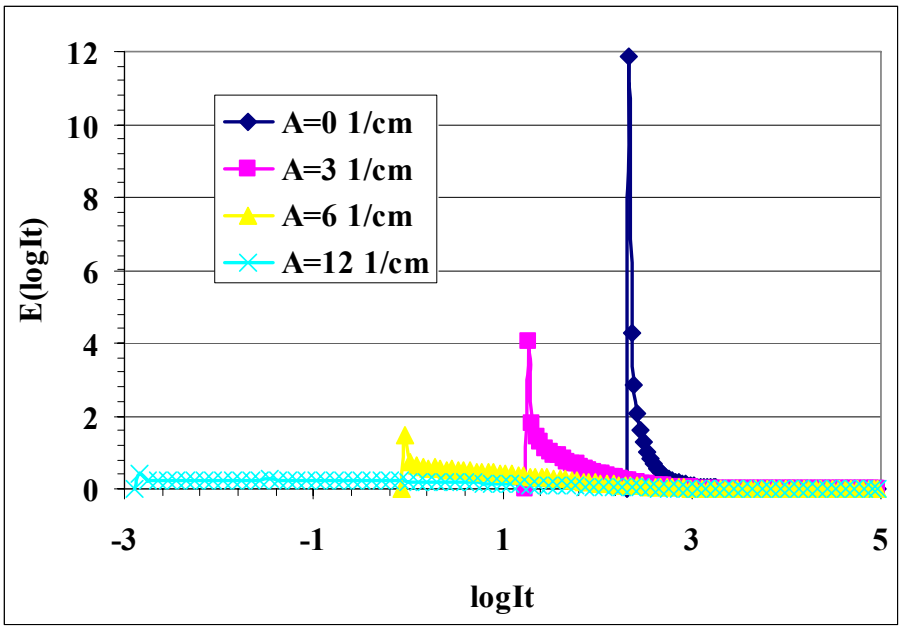

Figure 3.4 UV fluence distribution function with different absorption coefficients and Q=12 mL/s

When the absorption coefficient is fixed, according to equation (3.1), the fluence proportionally increases with the average residence time (the reciprocal of the flow rate). What is reflected in the curves of the fluence distribution function with different flow rates is that all curves have almost the same shape as shown in Figure 3.3. The only difference is that the peaks of the fluence distribution functions appear at different levels depending on the flow rates. When the flow rate is fixed, high absorption coefficients result in broad fluence distributions. Correspondingly, the shape of the fluence distribution function with high absorption coefficients is a low peak and a broad width like A=12 cm^{-1} in Figure 3.4.

In equation (3.2), it is often practical to use the dimensionless fluence of $It' = It / It_{av}$, where It_{av} is not the real average fluence of non-ideal reactors. Instead, the average fluence of ideal plug flow reactors is used, namely

$$It_{av} = I_{av} \times \tau_{av} = \frac{\int_0^{2\pi}\int_{R_1}^{R_2} I_0 R_1 \exp(-\alpha(r - R_1))\,\mathrm{d}\theta\mathrm{d}r}{\int_0^{2\pi}\int_{R_1}^{R_2} r\,\mathrm{d}\theta\mathrm{d}r} \frac{\pi(R_2^2 - R_1^2)L}{Q} \qquad (3.3)$$

The dimensionless fluence distribution function in Figures 3.5 and 3.6 corresponds to Figures 3.3 and 3.4, respectively.

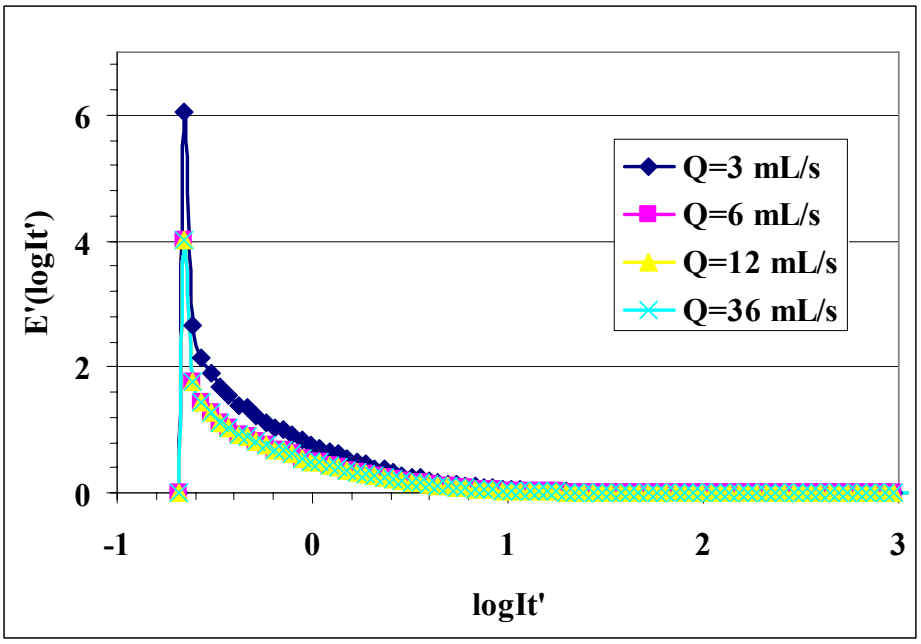

Figure 3.5 Dimensionless UV fluence distribution function with different flow rates and A=3 cm^{-1}

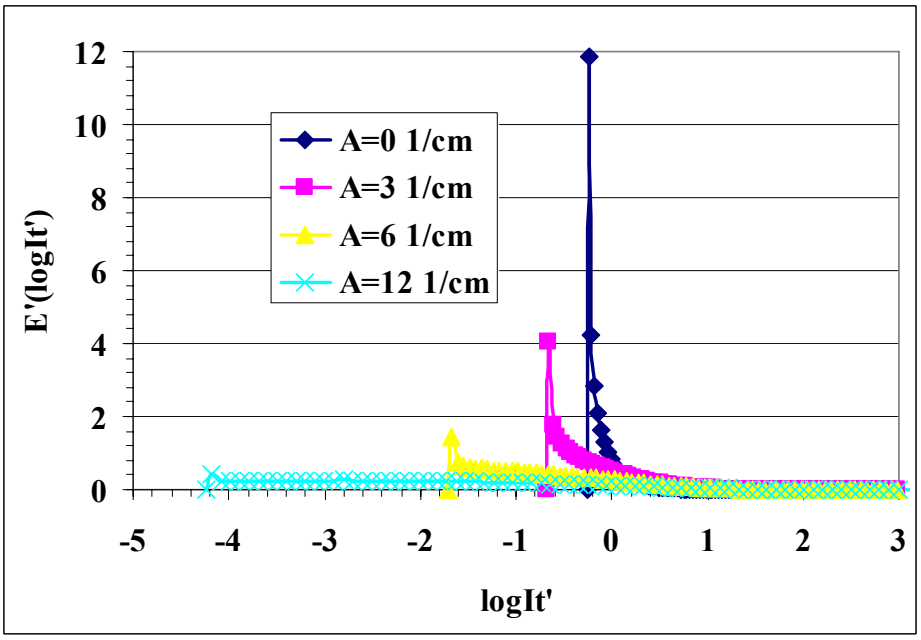

Figure 3.6 Dimensionless UV fluence distribution function with different absorption coefficients and Q=12 mL/s

The dimensionless UV fluence distribution function can easily demonstrate the deviation of real reactors from ideal plug flow reactors. For example, when juices do not absorb UV radiation (A=0 cm^{-1} in Figure 3.6), the performance of laminar reactors approaches that of ideal plug flow reactors. With the increase in absorption coefficients, the performance of laminar reactors deviates from that of ideal plug flow reactors very quickly. Moreover, according to Figure 3.3, decreasing the flow rates increases the inactivation levels in laminar UV reactors. However, it is an illusion because it is proven by Figure 3.5 that the deviation from ideal plug flow reactors is almost the same for different flow rates. The increased inactivation levels resulting from the decreased flow rates are at the cost of the decreased processing capability of laminar UV reactors.

In other words, decreasing the flow rates cannot overcome the disadvantage of broad fluence distributions when the absorption coefficients of the juices are high. The disadvantage of the broad fluence distributions for laminar reactors is alleviated only by decreasing the gap width or changing the flow pattern such as applying Taylor-Couette flow or turbulent flow. The dimensionless UV fluence distribution function will be used later and the prime representing dimensionless will be removed for convenience.

3.2 UV Disinfection of *E. Coli*

Figures 3.7 to 3.9 are the comparison of *E. coli* log reductions between experiments and theoretical predictions for reactors with different lengths. Operating parameters for experiments are the same as sub-section 2.4.1. The first order model with k=0.32494 cm^2/mJ and series-event model with k=0.67474 cm^2/mJ and n=4 are used for theoretical predictions. As expected, log reductions do not have a linear relationship with average residence times because of the non-uniform fluence distributions.

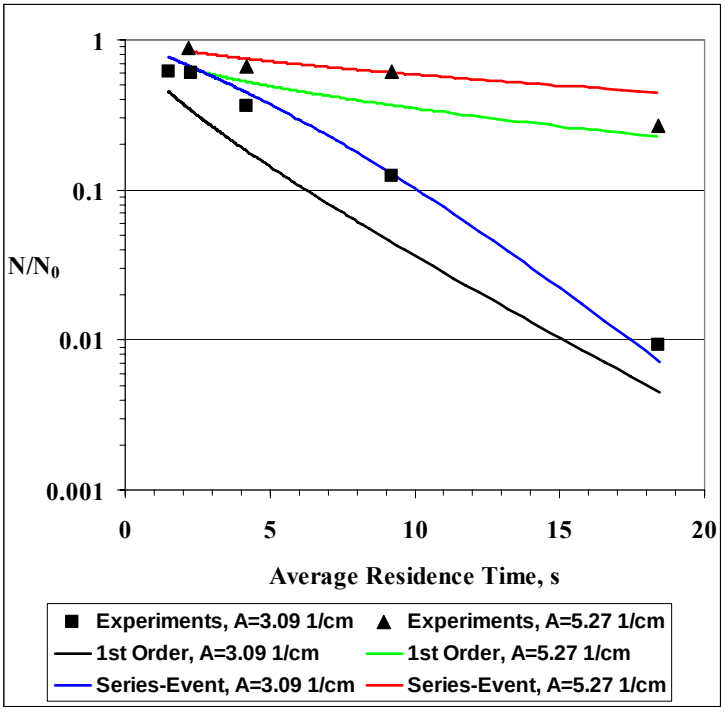

Figure 3.7 Comparison of *E. coli* log reductions between experiments and theoretical prediction for L=11.2 cm reactor

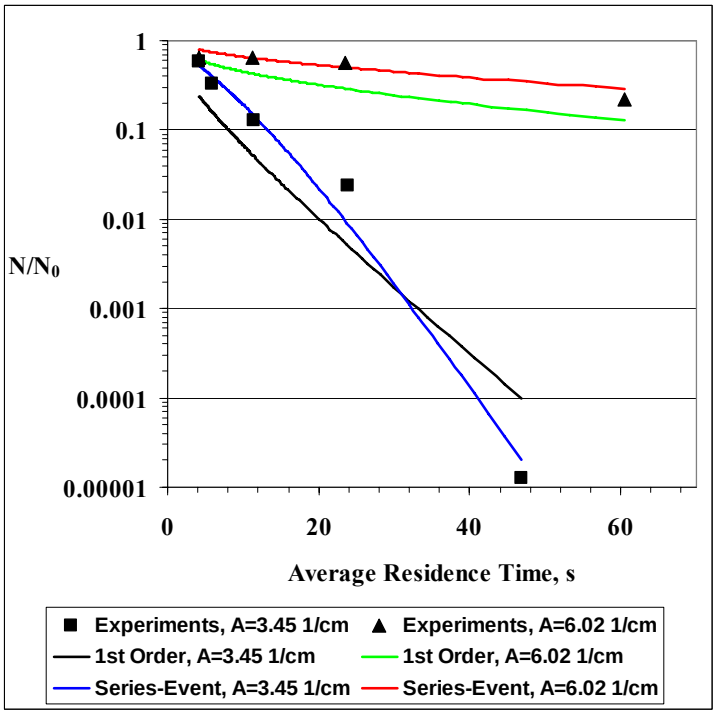

Figure 3.8 Comparison of *E. coli* log reductions between experiments and theoretical prediction for L=29.2 cm reactor

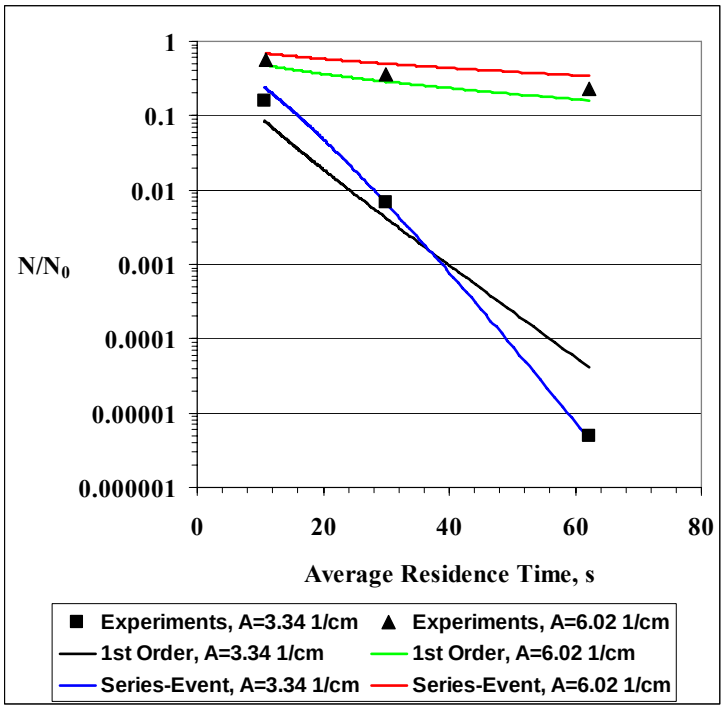

Figure 3.9 Comparison of *E. coli* log reductions between experiments and theoretical prediction for L=77.9 cm reactor

According to Figures 3.7 to 3.9, it can be seen that the first order model overestimates inactivation in regions with low fluence compared with experimental data. On the other hand, the first order model underestimates inactivation in regions with high fluence. This kind of error is avoided in the series-event model. Moreover, in Figures 3.7 to 3.9, the log reductions with $A \approx 6$ cm^{-1} are much less than half the log reductions with $A \approx 3$ cm^{-1} when the absorption coefficients are increased to about two times (from 3 cm^{-1} to 6 cm^{-1}). This is because fluence rates decrease exponentially with the path length from the radiation source and small increases in the absorption coefficient result in a large increase in under-irradiated volume.

3.3 Optimum Gap Width

3.3.1 Theoretical Analysis

Absorption coefficients of juices are different depending on brand and processing conditions. Their normal range is 10–40 cm^{-1} with values as high as 60 cm^{-1}. High absorption coefficients mean thin film annular UV reactors have to be used in inactivation of juices. In designing thin film annular UV reactors, one of the most important parameters is gap width. Because the velocity distribution along a narrow gap is not broad (the maximum velocity is about 1.5 times the average velocity), the residence time distribution does not significantly affect the overall disinfection efficiency.

If the processing capability or flow rate Q of the UV reactor is kept constant, the gap width has different effects in the overall disinfection efficiency. N_{av} is determined in the following form,

$$\frac{N_{av}}{N_0} = \frac{2\pi}{Q}\int_{R_1}^{R_2} f\left(\frac{I_0 R_1 \exp(-\alpha(r-R_1))L}{ru(r)}\right)u(r)rdr \,. \tag{3.4}$$

When the gap width is increased, the longer average residence time may increase the overall disinfection efficiency. On the other hand, a wide gap results in broader fluence distribution because fluence rate decreases exponentially with the path length from the radiation source. With large gap widths, the overall disinfection efficiency may become worse because of larger under-irradiated volumes. The final results are determined by the factor which is dominating. For each absorption coefficient, however, there is an optimum gap width.

3.3.2 Optimum Gap Width

Figures 3.10 and 3.11 show how log reductions change with gap width when the radius of inner cylinder stays constant at 1.225 cm, and radiation comes from the inner cylinder with fluence rate I_0=12 mW/cm^2 and UV lamp length L=77.9 cm. The first

order model with k=0.32494 cm^2/mJ and series-event model with k=0.67474 cm^2/mJ and n=4 are used for theoretical predictions. The radius of the outer cylinder is changed to create different gap widths. In Figure 3.10, the absorption coefficients vary from 3 cm^{-1} to 20 cm^{-1} and flow rate equals 12.5 mL/s. In Figure 3.11, the absorption coefficients vary from 30 cm^{-1} to 60 cm^{-1} and flow rate is decreased to 1.25 mL/s in order to achieve significant log reductions.

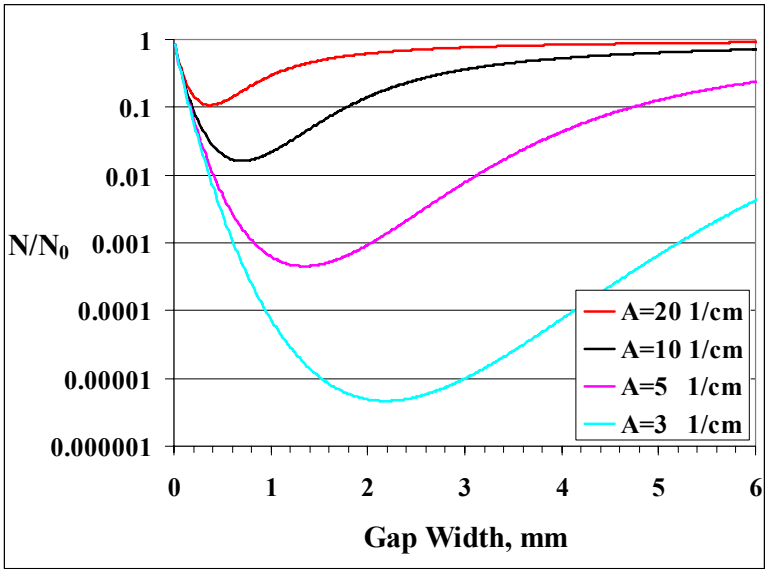

Figure 3.10 (a) Log reductions with the first order model when Q=12.5 mL/s

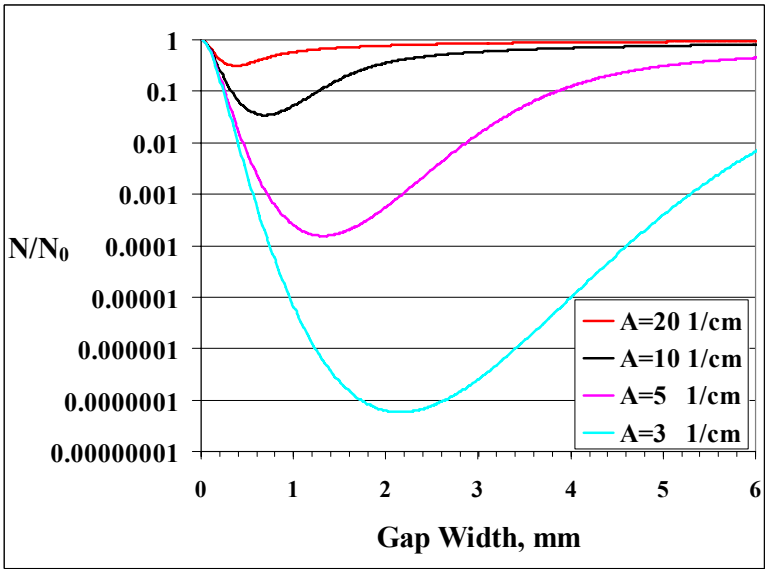

Figure 3.10 (b) Log reductions with the series-event model when Q=12.5 mL/s

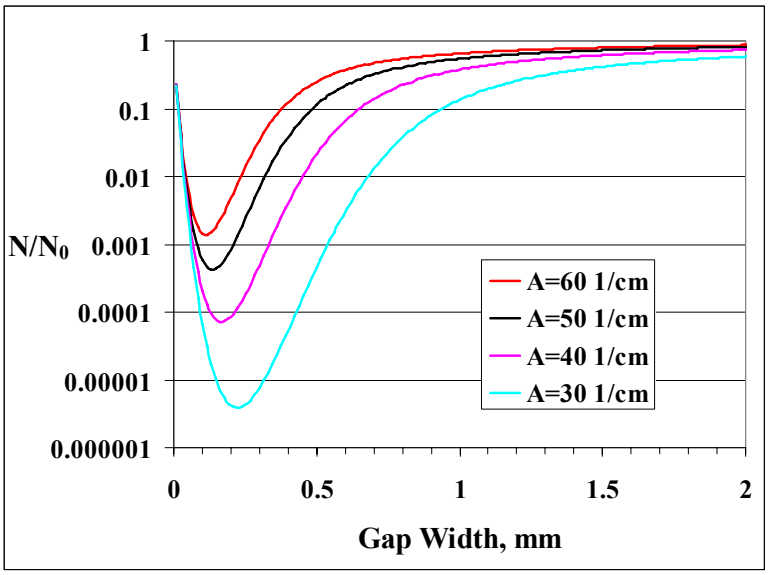

Figure 3.11 (a) Log reductions with the first order model when Q=1.25 mL/s

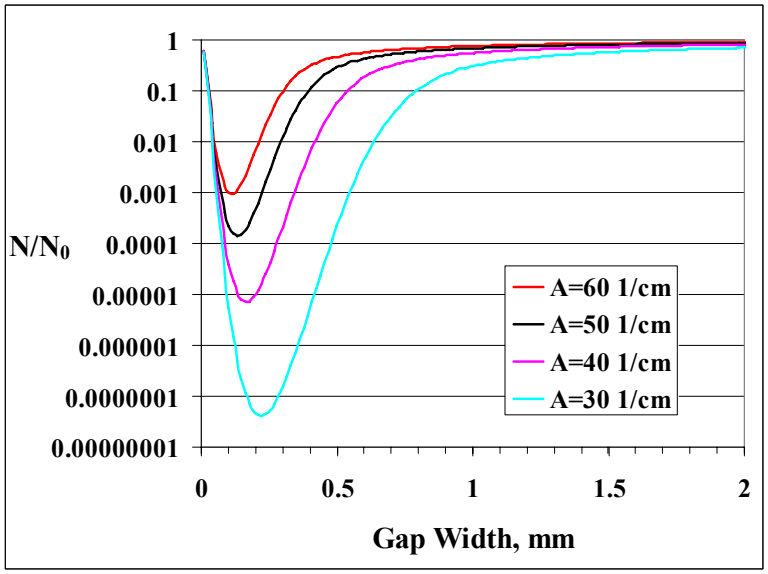

Figure 3.11 (b) Log reductions with the series-event model when Q=1.25 mL/s

It is proven by Figures 3.10 and 3.11 that there is an optimum gap width for each absorption coefficient. Different log reductions are predicted at the optimum gap width by the first order model and the series-event model. The log reductions at the optimum gap width are listed in Table 3.1. As expected, the series-event model predicts larger log reductions than the first order model when reduction levels are high, and the first order model predicts larger log reductions when reduction levels are low. However, the same

or very similar optimum gap widths are predicted by the first order model and series-event model. Therefore, only results with the series-event model will be provided and discussed below.

Table 3.1 Log reductions at optimum gap widths

A, cm^{-1}		3	5	10	20	30	40	50	60
1st order	Optimum d, mm	2.181	1.340	0.698	0.377	0.224	0.163	0.132	0.117
	N/N_0	5.331	3.344	1.792	0.969	5.410	4.140	3.373	2.856
Series Event	Optimum d, mm	2.150	1.325	0.698	0.377	0.224	0.163	0.132	0.117
	N/N_0	7.238	3.810	1.464	0.508	7.380	5.151	3.859	3.023

If the path length at which the fluence rate is 10% of the incident radiation fluence rate is defined as the penetration depth λ, or

$$\frac{I_\lambda}{I_0} = 10\% \tag{3.5}$$

the penetration depth will be the reciprocal of the absorption coefficient (10 base) or λ=1/A. A dimensionless group, the ratio of the penetration depth to gap width (λ/d), shows how far radiation can reach. If λ/d=1, the whole gap can be considered as an illuminated area. Then, Figures 3.10 (b) and 3.11 (b) can be modified to show how log reductions change with the ratio of the penetration depth to gap width (N/N_0 vs. λ/d, see Figures 3.12 and 3.13).

From Figures 3.12 and 3.13, it can be found that the difference between the optimum λ/d (λ/d with the largest log reduction) of different absorption coefficients is small. The optimum λ/d for a range of absorption coefficients is listed in Table 3.2. According to Table 3.2, the range of optimum λ/d is $1.33 \leq \lambda/d \leq 1.55$. Most of the optimum λ/d values oscillate around 1.5. When λ/d=1.5, the minimum fluence rate is 22% of the incident radiation fluence rate. This means that when $\lambda/d < 1.5$, pathogens are partially over-exposed to the radiation. However, disinfection of the over-exposed fraction cannot offset more surviving pathogens of the under-exposed fraction because of the wider gap width. According to Figures 3.12 and 3.13, inactivation levels decrease

greatly when λ /d < 1.0. When λ /d =0.2, log reduction is about 5% of the optimum log reduction. When λ/d is decreased to 0.1, the log reduction is only 1-2% of the optimum log reduction.

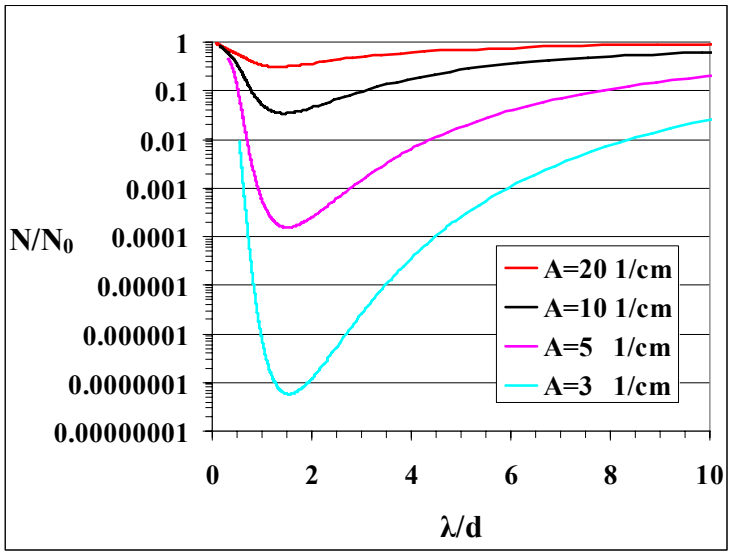

Figure 3.12 Log reductions change with λ/d when Q=12.5 mL/s

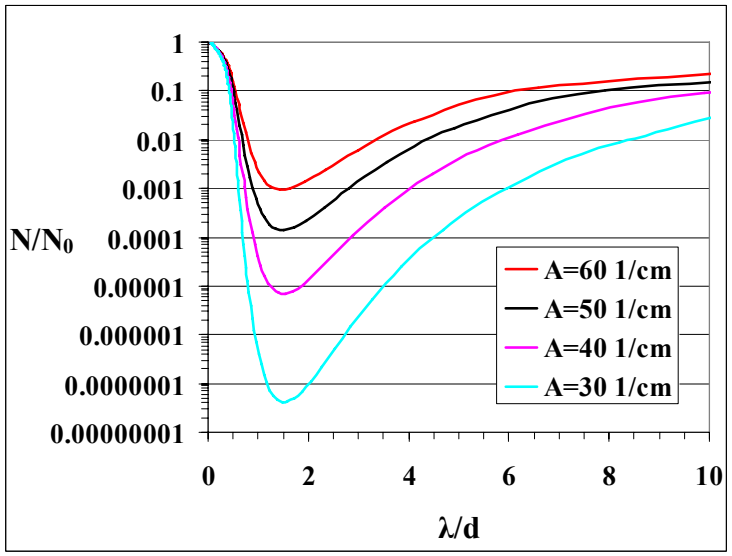

Figure 3.13 Log reductions change with λ/d when Q=1.25 mL/s

Table 3.2 Optimum λ/d at different absorption coefficients

A, cm^{-1}	3	5	10	20	30	40	50	60
Optimum λ/d	1.55	1.51	1.43	1.33	1.49	1.53	1.51	1.42

Normal absorption coefficients of juices are 10 – 40 cm^{-1} where optimum gap width is in the range of 0.17-0.67 mm. Therefore the gap width of laminar UV reactors used for juice disinfection should not be more than 1mm.

3.4 Correlation of UV Disinfection in Laminar Reactors

Theoretically, UV disinfection levels in laminar reactors can be obtained by integrating the following equation,

$$\frac{N_{av}}{N_0} = \frac{\int_0^{2\pi}\int_{R_1}^{R_2} f(\mathrm{It(r)})\mathrm{u(r)rd}\theta\mathrm{dr}}{\int_0^{2\pi}\int_{R_1}^{R_2} \mathrm{u(r)rd}\theta\mathrm{dr}} \tag{3.6}$$

However, it is desirable to find a simple correlation for log reductions and other parameters such as absorption coefficients. If the velocity profile is approximated by an average velocity and first order inactivation kinetics is used, then

$$\frac{N_{av}}{N_0} = \frac{2}{(R_2^2 - R_1^2)U_{av}}\int_{R_1}^{R_2} \exp\left(-kI_0\frac{R_1}{r}\exp(-\alpha(r-R_1))\frac{L}{U_{av}}\right)\mathrm{U_{av}rdr}. \tag{3.7}$$

Let the average residence time $\tau_{av} = L/U_{av}$, then

$$\frac{N_{av}}{N_0} = \frac{2}{R_2^2 - R_1^2}\int_{R_1}^{R_2} \exp\left(-\frac{kI_0\tau_{av}R_1}{r}\exp(-\alpha(r-R_1))\right)\mathrm{rdr}. \tag{3.8}$$

According to the mean value theorem, there is at least one radius R_m ($R_1 \le R_m \le R_2$) such that,

$$\frac{N_{av}}{N_0} = \frac{2}{R_2^2 - R_1^2}\exp\left(-\frac{kI_0\tau_{av}R_1}{R_m}\exp(-\alpha(R_m - R_1))\right)\bullet R_m(R_2 - R_1) \tag{3.9}$$

If conditions in Figure 3.9 are used to calculate the radius R_m (see Figure 3.14), it is found that the radius R_m is almost constant, especially with A=3.34 cm^{-1}, changing only from 0.89 to 0.92. Actually, there are two mean radii which satisfy the mean value theorem, but in Figure 3.14 only the radius near the outer cylinder is displayed.

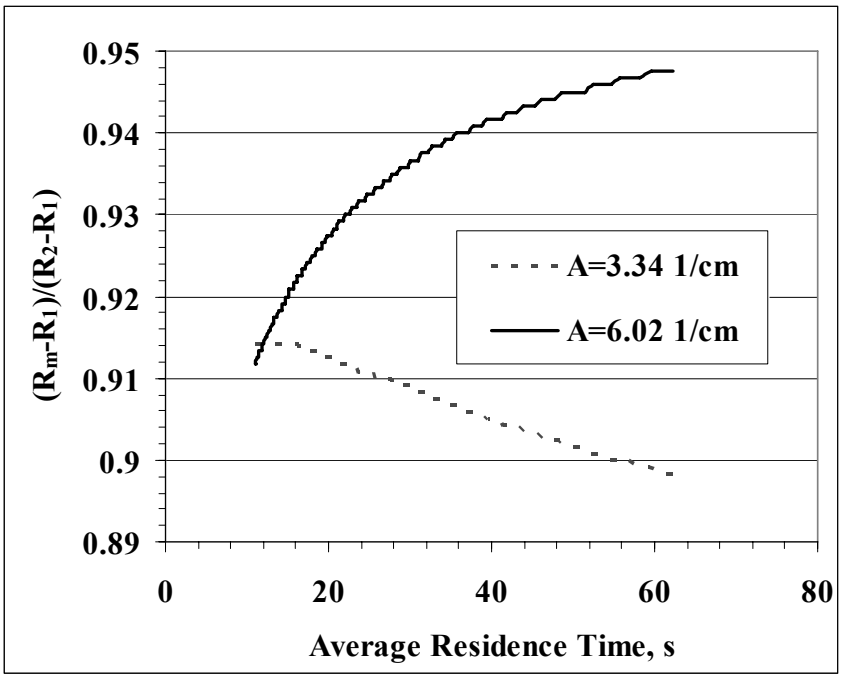

Figure 3.14 Mean radius R_m for L=77.9 cm reactor

Therefore, the radius R_m in equation (3.9) can be approximated as a constant. After the natural logarithm of both sides of equation (3.9) was taken,

$$\ln\left(\frac{N_{av}}{N_0}\right) = -\frac{kI_0\tau_{av}R_1}{R_m}\exp(-\alpha(R_m - R_1)) + \ln\left(\frac{2R_m}{R_2 + R_1}\right) \tag{3.10}$$

Assuming a dimensionless group $m = \frac{R_m - R_1}{R_2 - R_1} = \frac{R_m - R_1}{d}$, one obtains,

$$\ln\left(\frac{N_{av}}{N_0}\right) = -\frac{kI_0\tau_{av}}{1 + m(1/\kappa - 1)}\exp(-\alpha dm) + \ln\left(\frac{2R_m}{R_2 + R_1}\right). \tag{3.11}$$

Since $\frac{2R_m}{R_2 + R_1} \approx 1$ ($\frac{2R_m}{R_2 + R_1} = 1.146$ when R_1=1.225 cm, R_2=1.74 cm and $\frac{R_m - R_1}{R_2 - R_1} = 0.92$), the last term in the right side of equation (3.11) or $\ln\left(\frac{2R_m}{R_2 + R_1}\right)$ can be neglected. Finally, equation (3.11) reduces to,

$$\ln\left(\frac{N_{av}}{N_0}\right) = -\frac{kI_0\tau_{av}}{[1 + m(1/\kappa - 1)]\exp(\alpha dm)}. \tag{3.12}$$

Figure 3.15 is the correlation fitted according to equation (3.12). Experimental data of E. coli log reductions in Figure 3.15 are the same as those in Figure 2.9. The standard deviation of log reductions σ_y equals 0.224, and the coefficient of determination R^2 equals 0.962. Figure 3.15 shows that log reductions are proportional to 1/exp(αdm). In other words, log reductions decrease rapidly with the increase in absorption coefficients, especially when the gap is wide. Also, equation (3.12) confirms the results of the optimum gap width. When the gap is narrow, exp(αdm) is small. Increasing the gap width can improve the log reductions because the increase in average residence time is large enough to surpass the increase in the term exp(αdm). On the other hand, when the gap is wide initially, increasing the gap width makes the log reductions worse because the increase in average residence time is not large enough to offset the increase in the term exp(αdm).

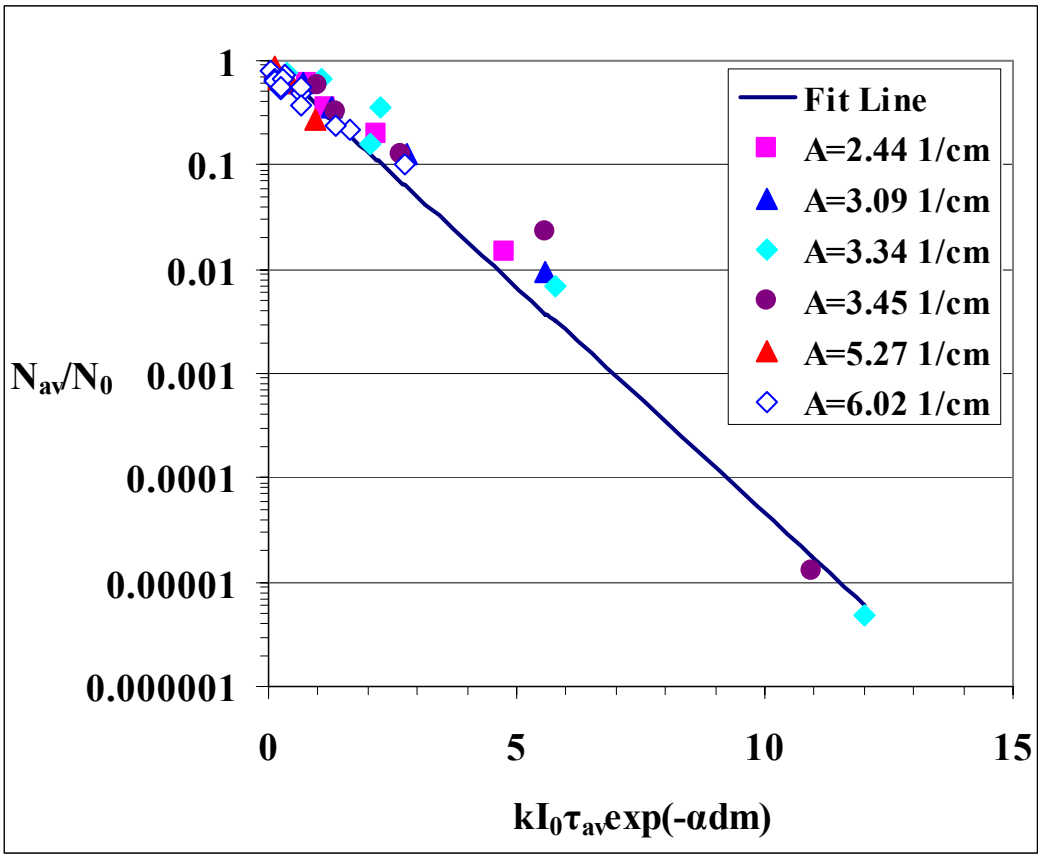

Figure 3.15 Correlation of UV Disinfection in Laminar Reactors

3.5 Conclusions

1. Increasing the fluence rate of the UV lamp and decreasing the flow rate will the increase fluence proportionally. However, these effects cannot overcome the disadvantage of a broad fluence distribution when the absorption coefficient of the fluid is high.
2. Compared with experimental data, the first order model overestimates inactivation in regions with low fluence and underestimates inactivation in regions with high fluence. This kind of error is avoided in the series-event model.
3. There is an optimum gap width for each absorption coefficient. The optimum λ/d for laminar UV reactors is about 1.5.
4. Because the normal absorption coefficients of juices are 10–40 cm^{-1}, the optimum gap width is in the range of 0.17-0.67 mm. Therefore, the gap width of laminar UV reactors used for juice disinfection should not be more than 1mm.
5. The log reduction in laminar reactors can be approximately correlated by

$$\ln\left(\frac{N_{av}}{N_0}\right) = -\frac{kI_0\tau_{av}}{\left[1+m(1/\kappa-1)\right]\exp(\alpha dm)}$$, where $m=(R_m- R_1)/d$.

CHAPTER 4

UV DISINFECTION IN TURBULENT REACTORS

4.1 Experimental Results

4.1.1 Solutions and Their Absorption Coefficients

The matrices that were used in this study were drinking water, and commercial clarified apple juices in order to examine the UV disinfection of *Y. pseudotuberculosis* in real fluids. Three brands of packaged apple juices (pasteurized, no preservatives) were purchased locally and stored at 4^{o}C for the trial.

- Ocean Spray, plastic bottle (Ocean Spray, Lakeville-Middleboro, MA, abbreviated as OS)
- Sahara Burst, aseptic box package (Sysco, Houston, TX, abbreviated as SB)
- Gordon Food Service, aseptic box package (Gordon Food Service, Grand Rapids, MI, abbreviated as GFS)

  Sahara Burst and Gordon Food Service brands were enriched with Vitamin C.

The absorption coefficients of the apple juices were determined from the slope of the absorbance at 254 nm versus the path length (Koutchma and Parisi, 2004a), as shown in Figure 4.1. The absorption coefficients of SB, GFS and OS were 39.093 cm^{-1}, 37.157 cm^{-1} and 7.155 cm^{-1}, respectively.

4.1.2 Flow Dynamics

Flow dynamics was evaluated for water and apple juices in the UV reactor. The axial Reynolds number (Re) was calculated using equation (4.1) based on the measured flow rate,

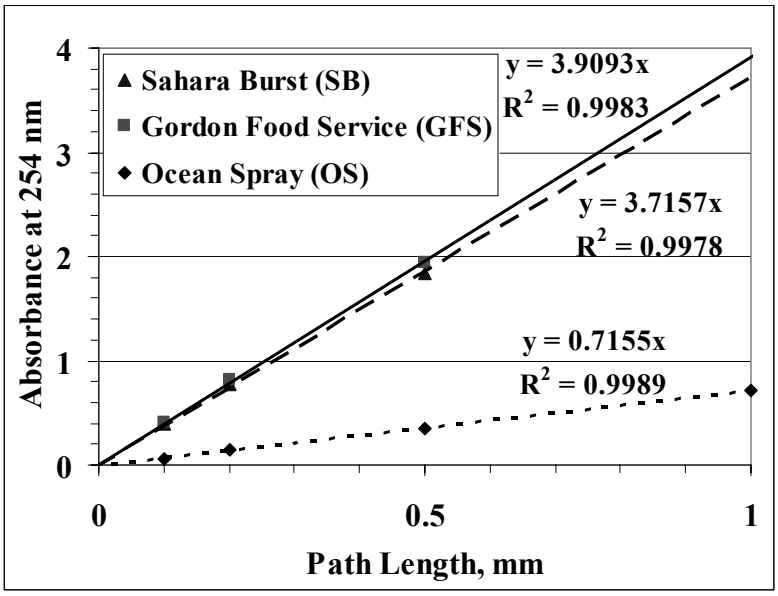

Figure 4.1 Absorbance of juices

$$\mathrm{Re} = \frac{Q}{\pi(R_2^2 - R_1^2)} L_c \rho / \mu \tag{4.1}$$

where the hydraulic diameter d_h was chosen as the characteristic length L_c. For annular gap, d_h =2d where d is gap width. The calculated Reynolds number and average residence time in each reactor are given in Table 4.1.

Table 4.1 Reynolds number and residence time in the annular UV reactors

Flow Rate, mL/s	Re	Average Residence Time, s		
		L=20cm V=89.7ml	L=40cm V=179.4ml	L=80cm V=358.9ml
Water at 20 ^{o}C: $\mu = 0.93 \times 10^{-3}$ Pa·s				
90	2077	0.99	1.99	3.99
180	4156	0.5	0.99	1.99
Apple juice at 20^{o}C: $\mu = 1.32 \times 10^{-3}$ Pa·s				
120	2000	0.75	1.49	2.99
240	4000	0.37	0.75	1.50

The turbulent UV-treatment system is shown in Figure 4.2. Reactors connected in series were used in order to increase the short residence time because of high flow rates. For pipe flow, the flow is turbulent when Re>2100 (Bird et al., 2002). The diameter of

the tube connecting the pump and the inlet of the reactor is 1.27 cm, and Re = 2467 when the flow rates of juices equal 120 mL/s. The transition Re is normally measured by flowing from a storage tank to a pipe and the system is free from large disturbances at the inlet. Because the flow at the inlets of the UV reactors is turbulent, 180 ml/s for water and 120 ml/s for apple juices can guarantee the turbulent flow in the annular gaps of UV reactors.

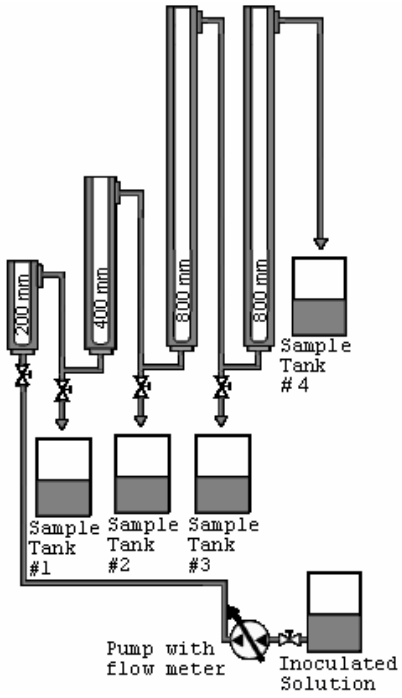

Figure 4.2 Schematic diagram of turbulent UV-treatment system

4.1.3 Numerical Modeling

The conservation equations of *Y. pseudotuberculosis* concentration in axisymmetrical coordinates can be written as (Bird et al., 2002),

$$u_r \frac{\partial N_i}{\partial r} + u_z \frac{\partial N_i}{\partial z} = \frac{\mu_t}{\rho Sc_t}\left(\frac{1}{r}\frac{\partial}{\partial r}\left(r\frac{\partial N_i}{\partial r}\right) + \frac{\partial^2 N_i}{\partial z^2}\right) + kI\left(N_{i-1} - N_i\right) \qquad (4.2)$$

where u_r and u_z are radial and axial velocity components and μ_t is turbulent viscosity. These three variables can be obtained by solving time-averaged *Navier-Stokes* equations by means of the k-ε two-equation model (Launder and Spalding, 1972). Sc_t is the

turbulent Schmidt number, which relates the turbulent momentum transport to the turbulent transport of the *Y. pseudotuberculosis* concentration N_i. The recommended Sc_t for most cases is 0.8 (Fox, 2003).

Turbulent Modeling

In FLUENT software, three k-ε models are provided: the standard k-ε model (Launder and Spalding, 1972), the RNG k-ε model (Yakhot and Orszag, 1986) and the realizable k-ε model (Shih, et al., 1995). All of the three k-ε models are tested. The difference among them is very small because both the realizable and RNG k-ε models were developed to take account of streamline curvature and swirling flows, and the streamlines in turbulent UV reactors are almost parallel. Therefore, the standard k-ε model is used for modeling turbulence.

In FLUENT software, user-defined scalars (UDS) are provided to solve the conservation equations of *Y. pseudotuberculosis* concentrations (4.2). However, since the source terms in equations (4.2) are not standard forms, user-defined functions (UDFs) are utilized to process the source terms in a special format. A UDF source C file is shown in APPENDIX A.1.

4.1.4 Comparison between Experiments and Numerical Simulations

UV inactivation of *Y. pseudotuberculosis* in water

The inactivation of *Y. pseudotuberculosis* in clear water in turbulent flow is shown in Table 4.2. The same case was run three times and log reductions with experiemtents are the averaged values. Because clear water is transparent to UV and the outer cylinder of the reactors is made of stainless steel, it is assumed in the numerical simulation that 19.5% of UV arriving at the surface of the stainless steel is reflected back into the reactors (Blatchely et al., 1997). It is proven by the results listed in Table 4.2 that

a UV treatment system is able to eliminate easily *Y. pseudotuberculosis* when the medium is water.

Table 4.2 UV inactivation of *Y. pseudotuberculosis* in clear water

Combination of Reactors	Experimental $\log(N_0/N)$	1st Order Model			Series-Event Model		
		$\log(N_0/N)$	Absolute error	Relative error, %	$\log(N_0/N)$	Absolute error	Relative error, %
20cm	1.8500	1.8344	-0.0156	-0.8	1.6082	-0.2418	-13.1
20cm+40cm	6.1800*	4.6148	-1.5652	-25.3	5.6101	-0.5699	-9.2
20cm+40cm+80cm	N/A**						

* Because initial concentration was $10^{6.18}$ and no detectable colony was seen on the plates, $\log(N_0/N)$ was assumed to be 6.18

** No detectable colony was seen on the plates.

UV inactivation of *Y. pseudotuberculosis* in apple juices

Tables 4.3 to 4.5 are the results for UV inactivation of *Y. pseudotuberculosis* in apple juices (SB, GFS and OS) in turbulent flow. The same case was run three times and log reductions with experiemtents are the averaged values. Because vitamin C strongly absorbs UV radiation at 254nm (Mellon, 1950) and increases the absorption coefficients of juices, the reduction in *Y. pseudotuberculosis* is severely limited when juices enriched with vitamin C are treated. For one complete pass (combination of reactors 20+40+80+80cm), the vitamin C-free juice yields ~0.6 log reduction, while juices enriched with vitamin C yield ~0.1 log reductions.

Table 4.3 UV inactivation of *Y. pseudotuberculosis* in SB apple juice

Combination of Reactors	Experimental $\log(N_0/N)$	1st Order Model			Series-Event Model		
		$\log(N_0/N)$	Absolute error	Relative error, %	$\log(N_0/N)$	Absolute error	Relative error, %
20cm	0.0267	0.0091	-0.0175	-65.8	0.0039	-0.0227	-85.2
20+40cm	0.0167	0.0207	0.0041	24.5	0.0084	-0.0083	-49.9
20+40+80cm	0.0500	0.0399	-0.0101	-20.2	0.0132	-0.0368	-73.7
20+40+80+80cm	0.0400	0.0590	0.0190	47.6	0.0182	-0.0218	-54.4

Table 4.4 UV inactivation of *Y. pseudotuberculosis* in GFS apple juice

Combination of Reactors	Experimental $\log(N_0/N)$	1st Order Model			Series-Event Model		
		$\log(N_0/N)$	Absolute error	Relative error, %	$\log(N_0/N)$	Absolute error	Relative error, %
20cm	0.0067	0.0100	0.0034	50.5	0.0041	-0.0026	-38.3
20+40cm	0.0367	0.0229	-0.0137	-37.5	0.0087	-0.0280	-76.4
20+40+80cm	0.0433	0.0447	0.0013	3.1	0.0137	-0.0296	-68.4
20+40+80+80cm	0.0700	0.0664	-0.0036	-5.1	0.0191	-0.0509	-72.7

Table 4.5 UV inactivation of *Y. pseudotuberculosis* in OS apple juice

Combination of Reactors	Experimental $\log(N_0/N)$	1st Order Model			Series-Event Model		
		$\log(N_0/N)$	Absolute error	Relative error, %	$\log(N_0/N)$	Absolute error	Relative error, %
20cm	0.1300	0.1385	0.0085	6.6	0.0487	-0.0813	-62.6
20+40cm	0.1567	0.3265	0.1698	108.4	0.1536	-0.0031	-2.0
20+40+80cm	0.2267	0.7312	0.5045	222.6	0.4418	0.2151	94.9
20+40+80+80cm	0.5867	1.1358	0.5491	93.6	0.8018	0.2151	36.7

Comparing experimental data with expected values, it is found that, though the absolute error is small, the relative error is large, up to 90% or more. Besides normal experimental errors and deviation between experiments and models, one possible reason is that log reduction levels as low as 0.1 introduce large relative errors. Another possible reason is that vitamin C, which strongly absorbs radiation at 254nm, is degraded during UV treatment. According to measurements, vitamin C decreases from 0.3 mg/mL to 0.12 mg/mL for SB apple juice after one complete pass. It is estimated that a 0.18 mg/mL loss of vitamin C will cause the absorption coefficient of the juice to decrease by 7.47 cm^{-1} (The absorption coefficient of vitamin C at 254 nm is about 41.5 cm^{-1} mL/mg, Mellon, 1950). However, the absorption coefficient of the juice is assumed to be constant in the numerical simulation. Overall, the inactivation data of the apple juices enriched with vitamin C are not very reliable because of low log reduction levels. Other methods such as increasing the incident fluence rate are needed to increase the log reduction levels.

There are two reasons why the log reduction levels are low in turbulent flow. One is the short residence time because high flow rates are required to sustain turbulent flow.

Another reason is the large absorption coefficients. Though the flow rate of water (180 mL/s) is 1.5 times those of juices (120 mL/s), the log reduction level with water can easily exceeds 6 after combination of reactors (20+40cm) because clear water is transparent to UV. In contrast, the log reduction level with the SB juice reaches less than 0.1 after one complete pass. Moreover, the gap width of 0.515 cm is too wide compared with the penetration depth of ~ 0.025 cm (the absorption coefficients ~ 40 cm^{-1}). The effect of the absorption coefficients and the optimum gap width will be investigated numerically in Sections 4.2 and 4.3.

4.2 Effect of Absorption Coefficients upon the Performance of UV Turbulent Reactors

Figure 4.3 shows the effect of absorption coefficients upon the performance of UV turbulent reactors when the series event model (k=0.984 cm^2/mJ and n=3) is used. The simulated object is an 80cm UV reactor as described in Sub-section 4.1.2. However, in the numerical simulation, the incident fluence rate is increased to 60 mW/cm^2 from the measured value 12 mW/cm^2. In Figure 4.3 the plug flow reactor (PFR) assumes a uniform velocity distribution $U_{av} = \frac{Q}{\pi(R_2^2 - R_1^2)}$ and uniform fluence rate distribution,

$$\mathrm{I_{av}} = \frac{\int_0^{2\pi}\int_{R_1}^{R_2} \mathrm{I_0}\,\frac{\mathrm{R_1}}{r}\exp(-\alpha(\mathrm{r}-\mathrm{R_1}))\mathrm{rd}\theta\mathrm{dr}}{\int_0^{2\pi}\int_{R_1}^{R_2}\mathrm{rd}\theta\mathrm{dr}} = \frac{\mathrm{R_1}[1-\exp(-\alpha(\mathrm{R_2}-\mathrm{R_1}))]}{0.5\alpha(\mathrm{R_2^2}-\mathrm{R_1^2})}\,\mathrm{I_0} \tag{4.3}$$

Correspondingly, the uniform fluence is

$$It_{av} = I_{av}\times\tau_{av} = \frac{\mathrm{R_1}[1-\exp(-\alpha(R_2-R_1))]}{0.5\alpha(R_2^2-R_1^2)}\,I_0\times\frac{L}{U_{av}} \tag{4.4}$$

The laminar flow in Figure 4.3 is an imaginary status where it is assumed that the flow having the same flow rate as turbulent flow continues as laminar flow and to have a laminar velocity profile.

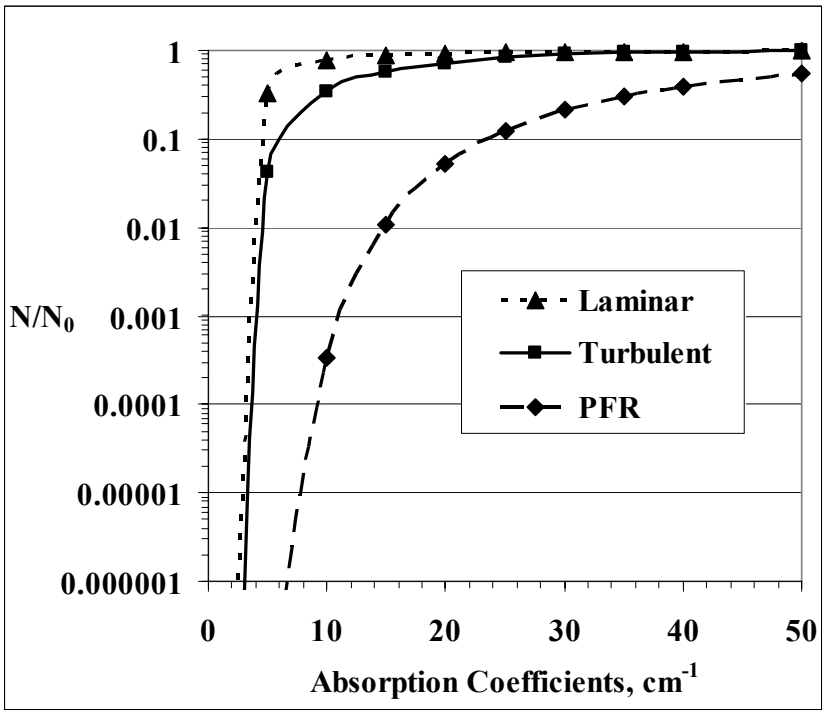

(a)

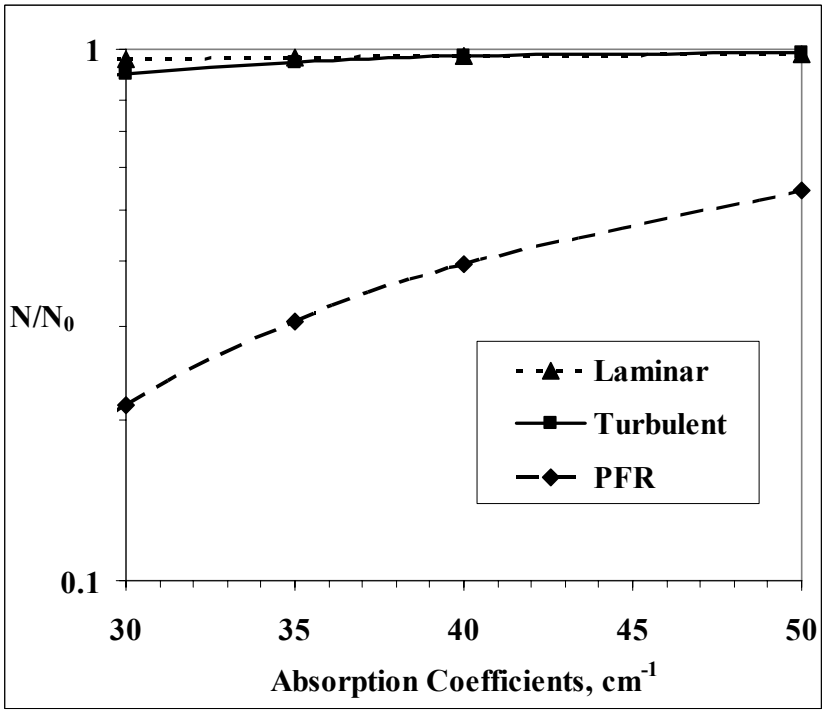

(b)

Figure 4.3 Effect of absorption coefficients upon the performance of UV turbulent reactors

From Figure 4.3, it can be seen that turbulent flow performs better than laminar flow because of the effect of turbulent mixing when absorption coefficients are low. However, when the absorption coefficients are high, e.g. more than 35 cm^{-1}, the log reductions in turbulent flow are almost the same as those in laminar flow. The main reason is the effect of the boundary layer. Turbulent theories and experiments have shown that the near-wall region can be subdivided into three layers (Davidson, 2004) as shown in Figure 4.4: (1) the viscous sublayer, y+ < 5; (2) the fully turbulent region, y+ > 40; and (3) the buffer layer between the viscous sublayer, 5< y+ <40. Here, y+ is a nondimensional parameter defined by the equation:

$$y^+ = \frac{\rho u_\tau y_P}{\mu} \tag{4.5}$$

where $u_\tau = \sqrt{\tau_w / \rho_w}$ is the friction velocity, and y_P is the distance from point P to the wall.

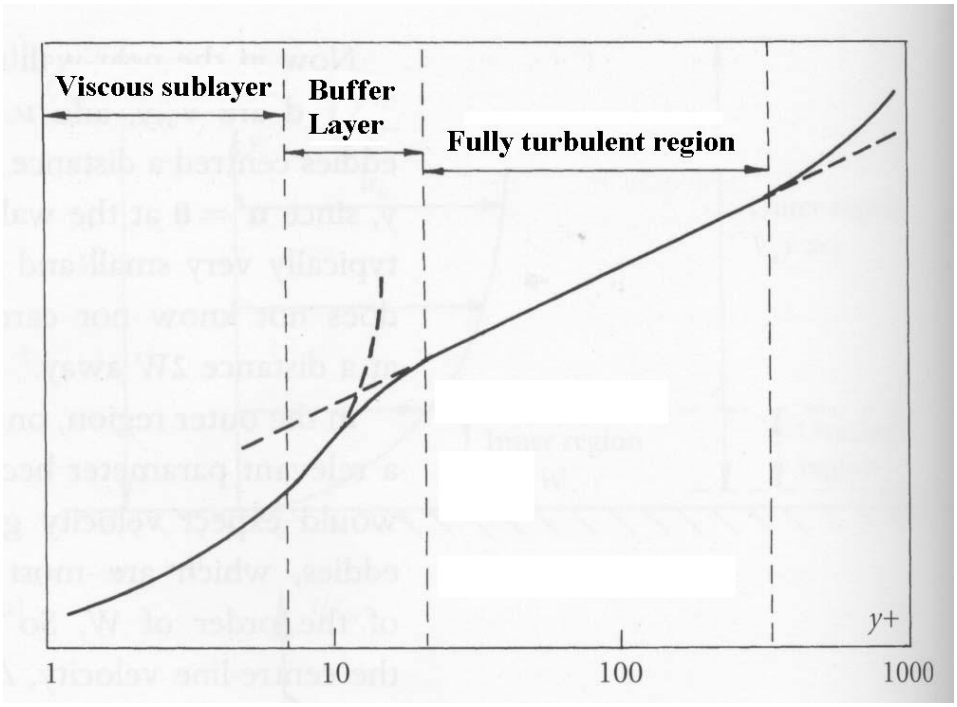

Figure 4.4 Subdivisions of the near-wall region

Since the flow is almost laminar in the viscous sublayer, turbulence plays a small role in momentum, heat and mass transfer. According to numerical simulations, the thickness of the viscous sublayer is 0.026 cm. When the absorption coefficient is 35 cm^{-1}, the penetration depth is about 0.029 cm which is almost the same as the thickness of the viscous sublayer. In this case, disinfection is largely restricted in the viscous sublayer, and improved performance expected from the turbulent flow does not occur.

4.3 Effect of Gap Width upon the Performance of UV Turbulent Reactors

When the juices to be processed have high absorption coefficients, there is an easy method to decrease the thickness of the viscous sublayer in turbulent flow in order to improve disinfection levels. The method is to decrease the gap width because the ratio of the thickness of the viscous sublayer to the gap width is almost constant. For example, the ratio is 0.0505 when the gap width is 0.515 cm, and the ratio is 0.0470 when the gap width is 0.1 cm according to numerical simulations.

When the effect of gap width upon the performance of UV turbulent reactors is investigated, all parameters are fixed except for the radius of the outer cylinder, which is decreased in order to decrease both the gap width and the thickness of the viscous sublayer, simultaneously. Figure 4.5 are numerical results of the GFS juice processed by a 40cm UV reactor (UV lamp length L=29.2 cm) with an 800 mW/cm^2 incident fluence rate.

When the gap width is decreased from 5.15 mm to 1 mm, the log reduction levels increase from 0.085 to 1.15 (series-event model), even though the average residence time in the radiation section is shortened from 1.17 s to 0.195 s. Figure 4.6 are the concentration profiles of surviving *Y. pseudotuberculosis* at the outlets of UV reactors with different gap widths. The effect of the viscous sublayer and turbulent mixing is obvious.

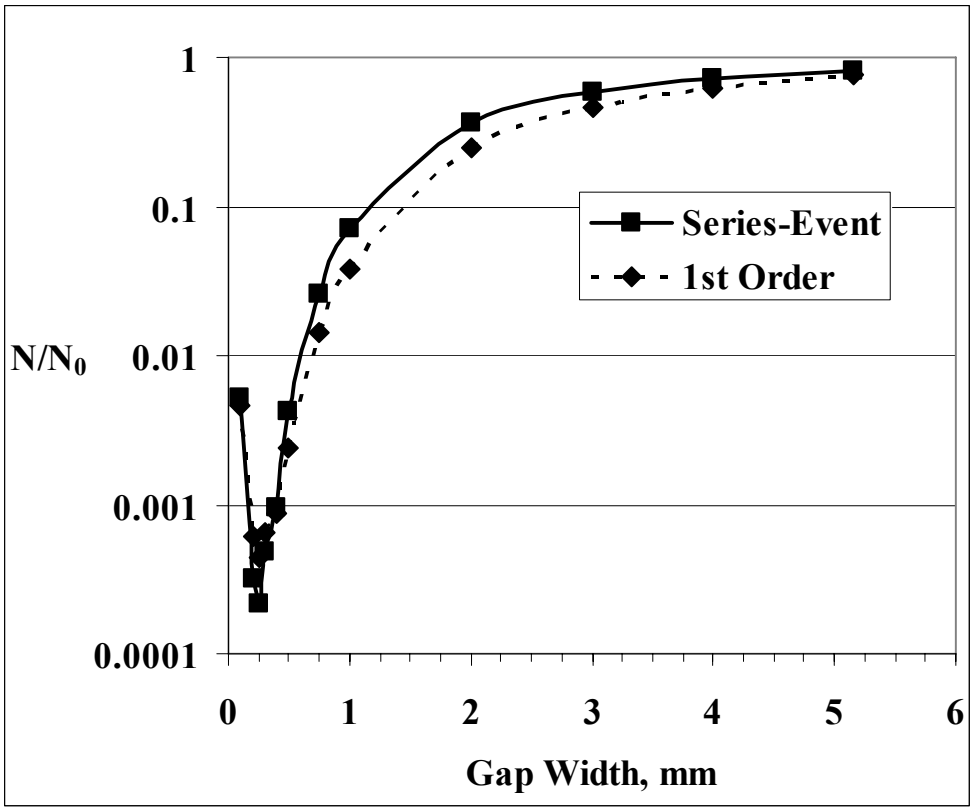

Figure 4.5 Disinfection results of the GFS juice processed by a 40cm UV reactor with an 800 mW/cm^2 incident fluence rate

According to the concentration profiles of surviving *Y. pseudotuberculosis*, the gap of the turbulent reactor can be divided into three regions:

(1) Over-irradiated region. This region is the viscous sublayer near the radiation source. Most of *Y. pseudotuberculosis* within this region is inactivated because of the high fluence rate and long residence time.

(2) Under-irradiated region. This region is the viscous sublayer on the opposite side of the radiation source. Most of *Y. pseudotuberculosis* within this region survives because UV is unable to penetrate the juices with high absorption coefficients and reach the viscous sublayer on the opposite side of the radiation source if the gap width is too large.

(3) Uniform-irradiated region. This region includes the fully turbulent region and the buffer layer between the viscous sublayer and the fully turbulent region. *Y. pseudotuberculosis* within this region receives an almost uniform radiation fluence because of turbulent mixing.

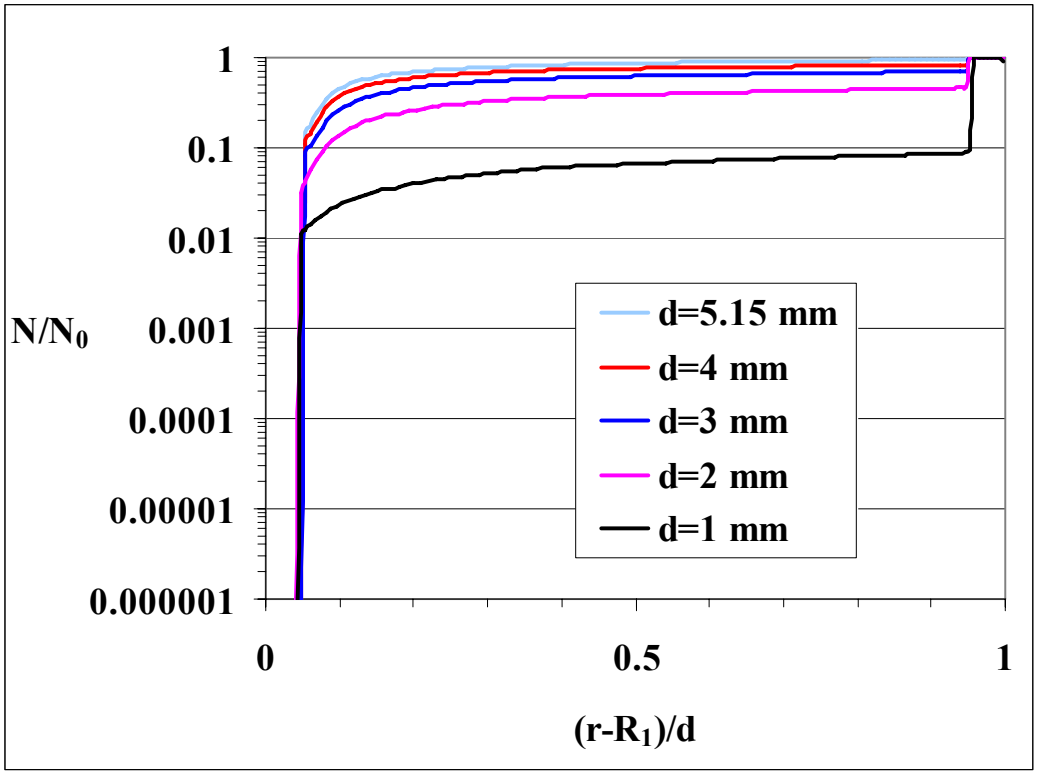

Figure 4.6 Concentration profiles of surviving *Y. pseudotuberculosis* at the outlets of UV reactors with different gap widths

Figures 4.5 and 4.6 show that it is much more important to guarantee that the penetration depth is larger than the thickness of the viscous sublayer than to increase the average residence time. In the former case with large penetration depths, disinfection occurs in the fully turbulent region.

4.4 Optimum Gap Width

Like laminar flow, there is an optimum gap width for each absorption coefficient in turbulent flow. Figure 4.7 shows how log reductions change with gap width when the radius of the inner cylinder keeps constant at 1.225 cm, and radiation comes from the inner cylinder with fluence rate I_0=800 mW/cm^2 and UV lamp length L=29.2 cm. The radius of the outer cylinder is changed to create different gap widths. The series event model (k=0.984 cm^2/mJ and n=3) is used in Figure 4.7.

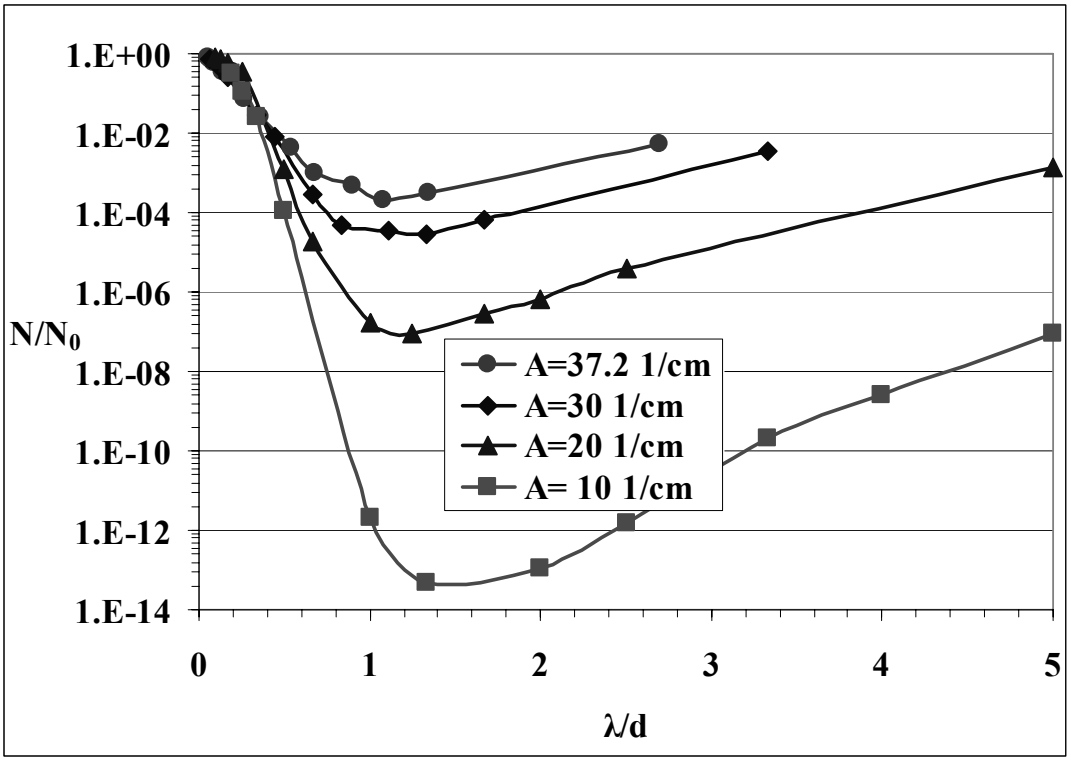

Figure 4.7 Log reductions change with λ/d in turbulent flow

From Figure 4.7, it can be found that the optimum λ/d does not change dramatically, varying from 1.1 to 1.3 for different absorption coefficients. Moreover, because log reductions do not decrease rapidly around the optimum λ/d, the optimum λ/d can be considered to be 1 in turbulent flow (the penetration depth equals the gap width). In other words, turbulent flow still requires that the radiation has to penetrate the whole gap to obtain optimum disinfection. This requirement is caused by the viscous sublayer

on the opposite side of the radiation source (under-irradiated region). Though the under-irradiated region occupies only a small fraction of the gap, about 5% or less, surviving pathogens in the under-irradiated region contribute the most to the surviving pathogens in the whole gap. Because most of pathogen in the under-irradiated region survives if $\lambda/d << 1$, the average concentration of the surviving pathogen at the outlet will be about 0.05 N_0. Then, the log reduction is still less than 2 ($\log_{10}0.05 = 1.3$) even if most of the pathogens in the fully turbulent regime and the viscous sublayer near the radiation source are inactivated. To release the restriction of gap width from the viscous sublayer, one method is to irradiate from both of the cylinders. Another method is to connect the UV reactors in series. Pathogens staying in the viscous sublayer in the first UV reactor may have a chance of entering a fully turbulent region in the next reactor and being inactivated. Moreover, the short residence time in turbulent flow conditions makes connecting reactors in series necessary.

4.5 Correlation of UV Disinfection in Turbulent Reactors

If tubular turbulent reactors can be approximated as plug flow reactors (PFRs), and the first order inactivation model is used,

$$\ln\left(\frac{N}{N_0}\right) = -kIt_{av} \tag{4.6}$$

Substitution of equation 4.4 gives

$$\ln\left(\frac{N}{N_0}\right) = -k\frac{R_1[1-\exp(-\alpha(R_2-R_1))]}{0.5\alpha(R_2^2-R_1^2)}I_0 \times \frac{L}{U_{av}} \tag{4.7}$$

Normally, if $\alpha(R_2-R_1)>5$, $\exp(-\alpha(R_2-R_1))<<1$. Then equation (4.7) can be simplified further.

$$\ln\left(\frac{N}{N_0}\right) = -\frac{kI_0\tau_{av}}{\alpha d}\frac{2R_1}{R_2+R_1} \tag{4.8}$$

In equation (4.8), $\frac{2R_1}{R_2 + R_1}$ is introduced because of the curvature effect. It can be defined as a new dimensionless group, Rc,

$$R_c = \frac{2R_1}{R_2 + R_1} \quad . \tag{4.9}$$

To correct for deviations between real reactors and PFRs, the ratio c/δ has to be added to equation (4.8). Thus, equation (4.8) is modified as,

$$\ln\left(\frac{N}{N_0}\right) = -\frac{\mathrm{ck}I_0\tau_{\mathrm{av}}R_c}{\alpha d\delta} \tag{4.10}$$

where c/δ represents the deviation between real reactors and PFRs. Here, the boundary layer thickness δ is calculated according to equation (4.11) (Middleman, 1998),

$$\delta = \frac{2\mu}{\rho U_{av} f} \tag{4.11}$$

where f is the dimensionless shear stress. According to boundary layer theory (Schlichting and Gersten, 2000),

$$f = 0.079\,\mathrm{Re}^{-0.25} \tag{4.12}$$

The numerical results in Figure 4.3 and the experimental results in Tables 4.3 to 4.5 are correlated to generate Figure 4.8, where c = 0.0158 cm is obtained by the least squares method. The standard deviation of log reductions σ_y equals 0.108, and the coefficient of determination R^2 equals 0.951 for exponential fit.

Figure 4.8 shows that the correlation equation (4.10) agrees with numerical and experimental results. Unlike the log reductions in laminar reactors, which are proportional to $1/[\exp(dm)]^{\alpha}$, the log reductions in turbulent reactors are proportional to $1/\alpha$. In other words, the log reductions in the turbulent reactors decrease with the increase in absorption coefficients much more slowly because of good turbulent mixing than similar results in laminar reactors.

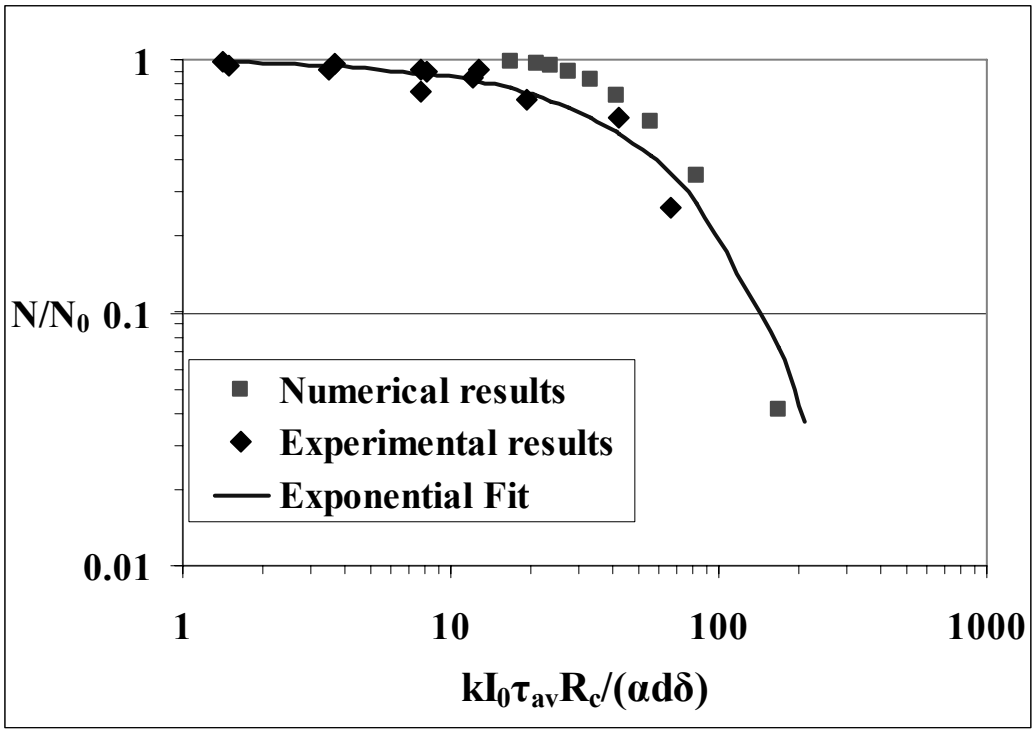

Figure 4.8 Correlation of UV disinfection in turbulent reactors

4.6 Conclusions

1. Compared with UV laminar flow reactors, UV turbulent flow reactors can perform better when the penetration depth of juices is larger than the viscous sublayer thickness.
2. When the penetration depth of juices is small, better disinfection can be obtained if the gap width is decreased, even though average residence time is reduced greatly.
3. There is an optimum gap width for each absorption coefficient. The optimum λ/d for turbulent UV reactors is about 1.
4. The log reduction in turbulent reactors can be correlated by the exponential formula $\ln\left(\frac{N}{N_0}\right) = -\frac{\mathrm{ck}I_0\tau_{\mathrm{av}}R_c}{\alpha d\delta}$, where c=0.0158 cm

CHAPTER 5

UV DISINFECTION IN TAYLOR VORTEX REACTORS

UV disinfection in laminar and turbulent reactors is discussed in previous chapters. In order to achieve good disinfection levels, the laminar reactors require very narrow gap widths when juices with high absorption coefficients are processed. Though turbulence can be introduced as a partial solution, unfortunately, the high flow rate to ensure turbulent flow is coupled with a reduced residence time. Achieving a 5 log reduction requires either a very long lamp in a thin-film annular reactor, or many thin-film annular reactors connected in series. Furthermore, turbulent flow increases the pressure drop across the reactors and the axial mixing resulting from turbulent flow broadens the fluence distribution. Taylor-Couette flow provides the possibility to decouple mixing and the device flow rates (Forney et al., 2002b, 2003a, Forney and Pierson, 2003c, Forney et al., 2004).

5.1 Experimental Results

5.1.1 Taylor Vortex Reactor Configuration and Experimental Procedure

The schematic figure of a Taylor vortex reactor is shown as Figure 5.1. The stator of the Taylor vortex UV reactor was constructed of 4.58 cm internal, fused quartz (Vycor, Corning Inc., Corning NY) with a Teflon rotor of 3.43 cm outer diameter corresponding to a gap width of 5.75 mm. The radiation source consisted of 6 medium-pressure, mercury UVC lamps with diameters of 0.95 cm and effective lengths of 5.34 cm (Pen-Ray Lamps, UVP, Upland, CA), which were distributed evenly around the quartz stator. At the same time the UV lamps were surrounded with an aluminum reflector as shown in Figure 5.1. The radiation fluence rate on the surface of the quartz was assumed to be uniform and equaled 25 mW/cm^2. The Taylor number is defined as,

$$Ta = \frac{R_1 \Omega_1 d}{\upsilon}\left(\frac{d}{R_1}\right)^{1/2} \tag{5.1}$$

where R_1 is the radius of the inner cylinder, Ω_1 is the angular velocity of the inner cylinder, d is the gap width, and ν is the kinematic viscosity.

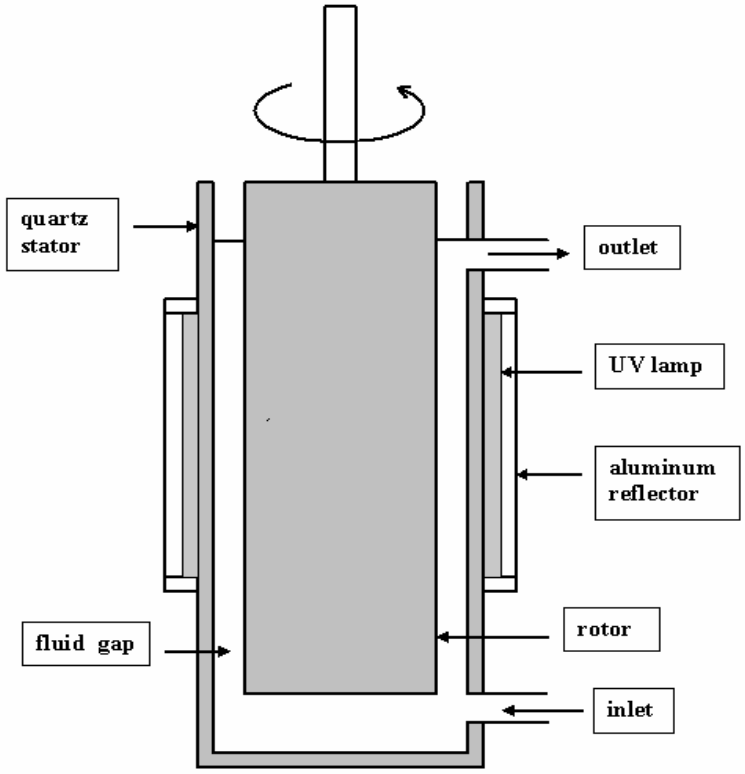

Figure 5.1 Schematic figure of a Taylor vortex UV reactor

The de-ionized water inoculated with *E. coli* K12 (ATCC 25253) was pumped into the reactor through the inlet by a positive displacement pump. Caramel 050 (D.D. Williamson & Co., Inc., Louisville, KY) was added to adjust the absorption coefficient of the de-ionized water. Samples for microbial analysis were taken and place plated before and after radiation exposure. Analysis procedures were similar to those in Chapter 2 and are not restated.

Though a Taylor vortex reactor meets the geometrical requirements of two dimensional (2D) axisymmetry, the fluid flow may be three dimensional flow because the axisymmetry of the flow will be destroyed when the Taylor number is larger than 1.2

times the critical Taylor number (Lueptow et al., 1992). Thus, the fluid flow in the above Taylor vortex reactor may be three dimensional (3D) flow. However, compared with 2D axisymmetrical simulations, 3D simulations occupy a much larger computer memory and require lengthy iterations. Both 2D axisymmetrical and 3D simulations will be given and compared with experimental results. If the difference between the 2D axisymmetrical and 3D simulations is small, the 2D axisymmetrical simulations will be used.

5.1.2 2D Axisymmetrical Simulation Results

The computational domain of the Taylor vortex reactor is shown in Figure 5.2. The inlet and outlet sections were modified so that the axisymmetry assumption was valid, and velocity inlet and outflow of FLUENT boundary conditions can be applied to the inlet and the outlet respectively.

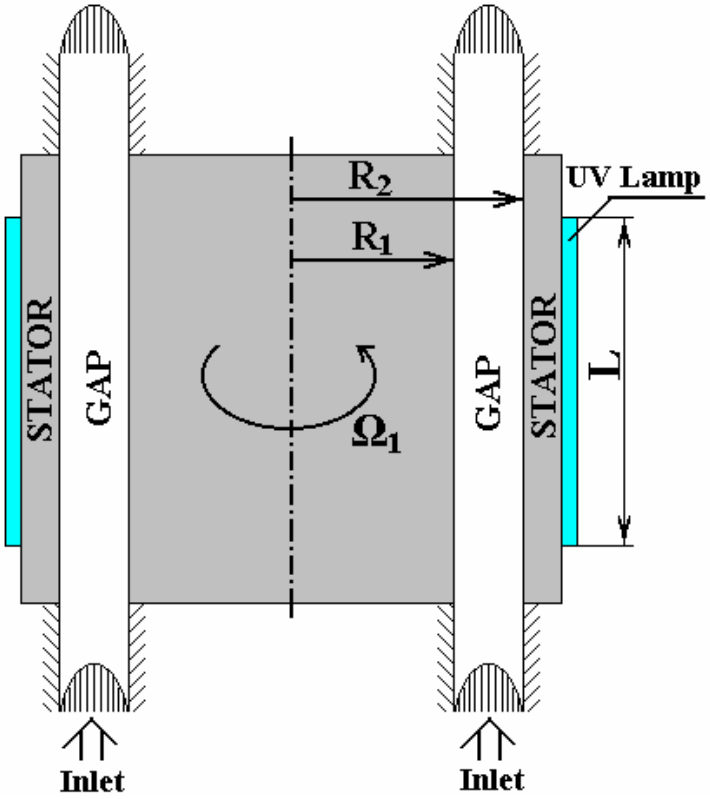

Figure 5.2 2D axisymmetrical computational domain

The governing equations for concentrations of *E. coli* K12 in axisymmetrical coordinates can be written as (Bird et al., 2002),

$$\frac{\partial N_i}{\partial t} + u_r \frac{\partial N_i}{\partial r} + u_z \frac{\partial N_i}{\partial z} = D\left(\frac{1}{r}\frac{\partial}{\partial r}\left(r\frac{\partial N_i}{\partial r} \right) + \frac{\partial^2 N_i}{\partial z^2} \right) + kI\left(N_{i-1} - N_i \right) \qquad (5.2)$$

where u_r and u_z are radial and axial velocity components, and N_i is the concentration of viable microorganisms at event level i. u_r and u_z can be obtained by solving laminar *Navier-Stokes* equations (1.9). Since the diffusion coefficient D is small, the diffusion term in equation (5.2) is neglected. The inactivation constant k of *E. coli* K12 was determined in Chapter 2. User-defined scalars (UDS) in FLUENT software are used to solve the governing equations of *E. coli* K12 concentrations (5.2). Like turbulent reactors, user-defined functions (UDFs) are utilized to process the source terms in a special format. A UDF source C file is given in APPENDIX A.2.

Cycle of Taylor-Couette Flow

Since Taylor-Couette-Poiseuille flow is caused by a hydrodynamic instability, the flow is not in steady state. Figure 5.3 is the stream function when the flow rate Q is 40 mL/min and Ta=150. In Figure 5.3, the left boundary is the outer cylinder and the right boundary is the inner cylinder. Only the part of the inner cylinder with the thick line is rotating. The number below each stream function figure represents the iteration number. It is shown by Figure 5.3 that vortices advance downstream (from the bottom to the top of the figure) with iteration (time).

On the upstream side, the evolution of vortices can be summarized as:

1. The first vortex becomes longer as it advances downstream.
2. The first vortex breaks up into three small vortices.
3. The three small vortices originating from the one vortex grow to normal size as they advance downstream.

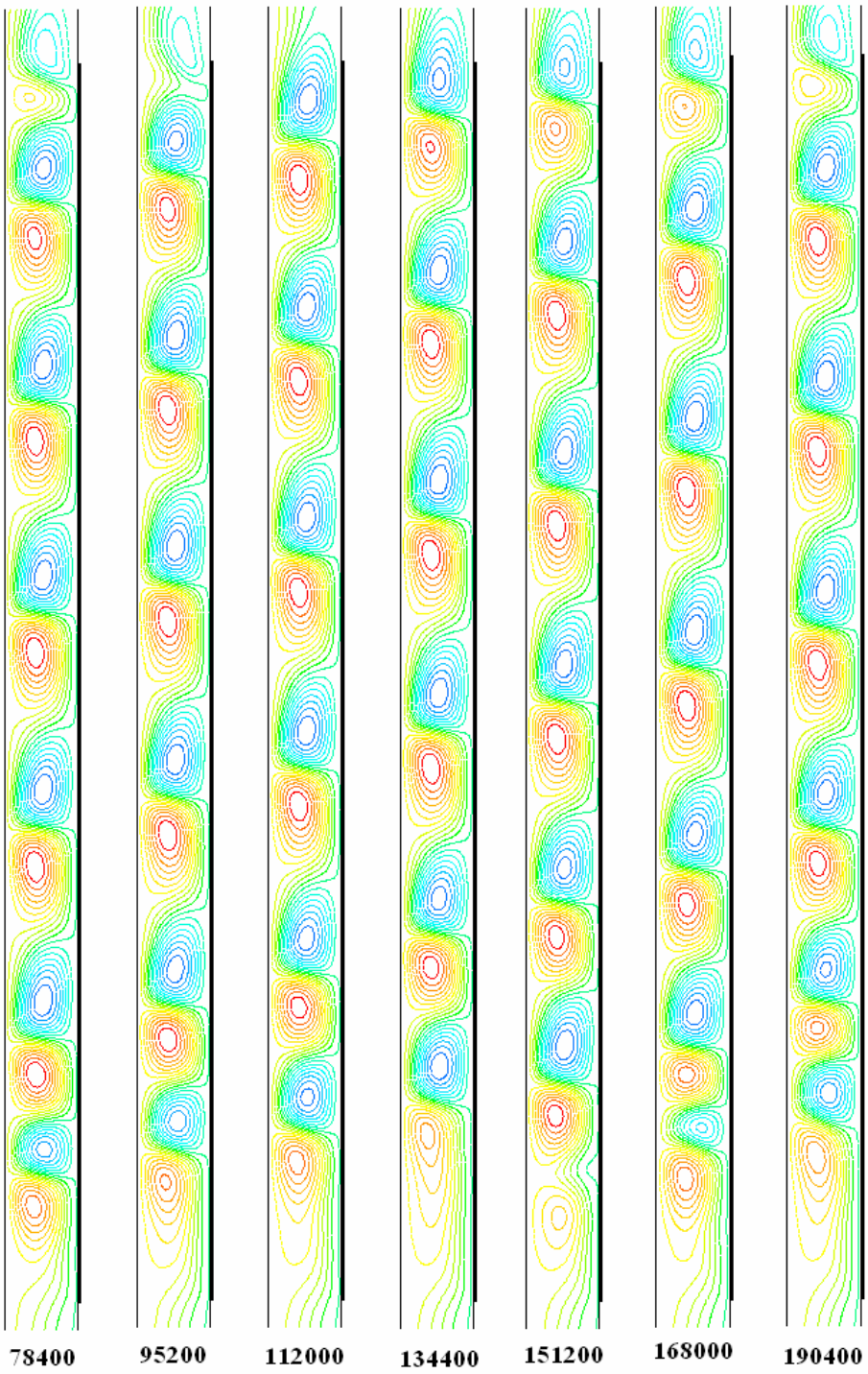

Figure 5.3 Stream function when Q=40 mL/min and Ta=150

On the downstream side, the evolution of vortices can be summarized as:

1. The vortex next to the last vortex becomes smaller as it advances downstream.

2. The vortex next to the last vortex is combined with the last vortex. A new last vortex forms.
3. The new last vortex becomes smaller. Finally it is combined with the vortex which is next to it.

All these steps form a cycle which is repeated. Correspondingly, the average pathogen concentration at the outlet oscillates with the positions of the vortices. Figure 5.4 is the average pathogen concentration at the outlet with Ta=150. Like the cycle of generation and disappearance of vortices, the average pathogen concentration at the outlet also has a cycle. By measuring the position and displacement velocity of a vortex, one cycle takes about 13.3 s. This means that 8.9 mL of fluid leaves the reactor within a cycle. Because these are 2D simulations, 3D results will reveal that one cycle takes a shorter time and the oscillation is smaller ($N_{max}/N_{min}\approx 2$). Considering $\log_{10} N_{\max} - \log_{10} N_{\min} = \log_{10} 2 \approx 0.3$ and that a 2 log reduction is obtained when Ta=150, the oscillation of pathogen concentration has little effect on sampling if the volume of the samples is not too small. Of course, the oscillation has little effect on the design of UV reactors. Moreover, all pathogen concentrations in the following sections are average values within a cycle.

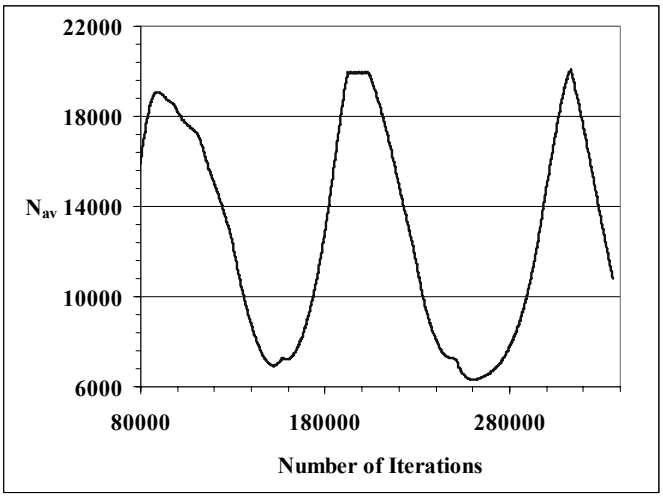

Figure 5.4 2D calculation of the average pathogen concentration at the outlet with Ta=150

Log Reduction with Different Taylor Numbers

Figure 5.5 is the comparison between experimental results and 2D simulations with different Taylor numbers when Q=40 mL/min. and A=11 cm^{-1}. Figure 5.5 shows that the series- event model generally agrees with experimental results. Also, the first order model over-estimates the log reductions compared to experimental results. Furthermore, the log reductions increase with the Taylor number, which is caused by a decrease in the boundary layer thickness with large Taylor numbers.

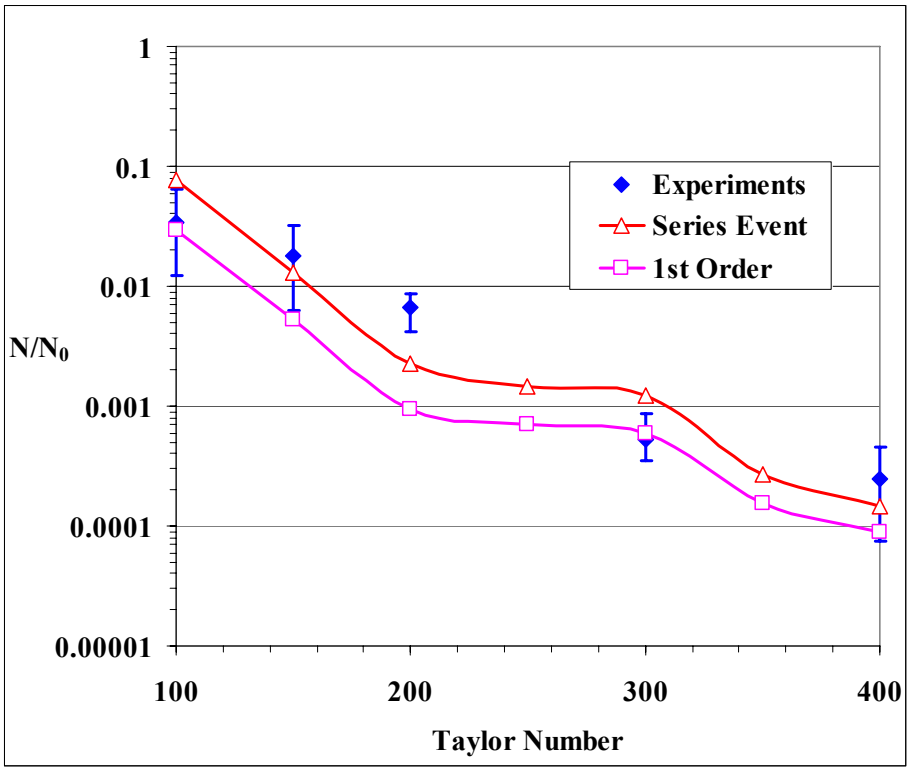

Figure 5.5 Comparison between experimental results and 2D simulations with different Taylor numbers when Q=40 mL/min. and A=11 cm^{-1}

Figure 5.6 is the stream function for different Taylor numbers. In Figure 5.6 the upper and lower boundaries are the outer and inner cylinders, respectively, and the vortices move from left to right. Pathlines of fluids in Taylor- Couette flow can be divided into two parts (Wereley and Lueptow, 1999). One part is within the vortices and advances downstream with a uniform velocity (it will be called the vortex part). Another

part is winding around the vortices and alternately flowing near the inner and outer cylinder (it will be called the winding part). From Figure 5.6 (a), it seems that the winding part occupies about 50% when Ta=100. Actually, this is an illusion because Taylor-Couette flow is unsteady flow and stream functions in Figure 5.6 are not real pathlines. It has been proven experimentally and numerically that the vortex displacement velocity is about 1.17 times the average axial velocity (Simmers and Coney, 1980, Gu and Fahidy, 1985, 1986, Haim and Pismen, 1994, Howes and Rudman, 1998).

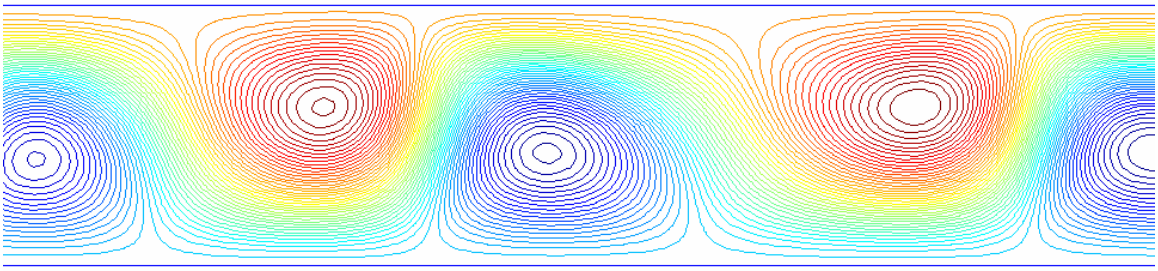

(a) Ta=100

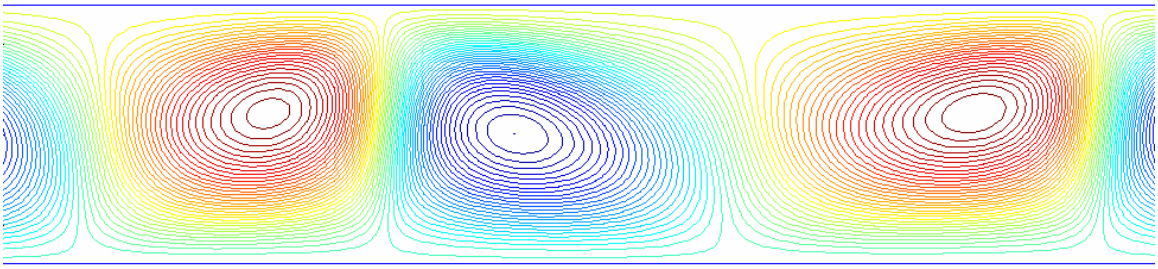

(b) Ta=200

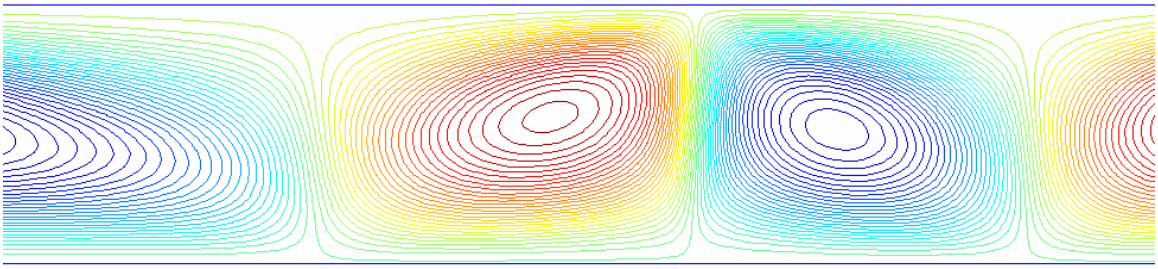

(c) Ta=400

Figure 5.6 Stream function for different Taylor numbers

Figure 5.7 is the stream function in a moving frame, namely, the original velocity is subtracted by 1.17 times the average axial velocity. It is clear in Figure 5.7 that the

winding part occupies a small percentage of the flow in the gap. However, because the vortex part advances downstream faster than average axial velocity, the winding part has to move slower than the average axial velocity. The winding part will receive a higher fluence than the average since the winding part flows alternately near the inner and outer cylinder (radiation source). Correspondingly, the vortex part will receive a lower fluence than the average. Therefore, the winding part should be as small as possible in order to achieve a narrow fluence distribution and better disinfection efficiency.

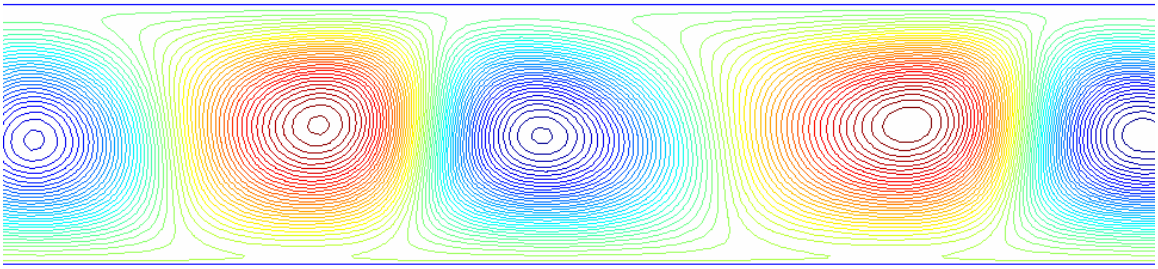

(a) Ta=100

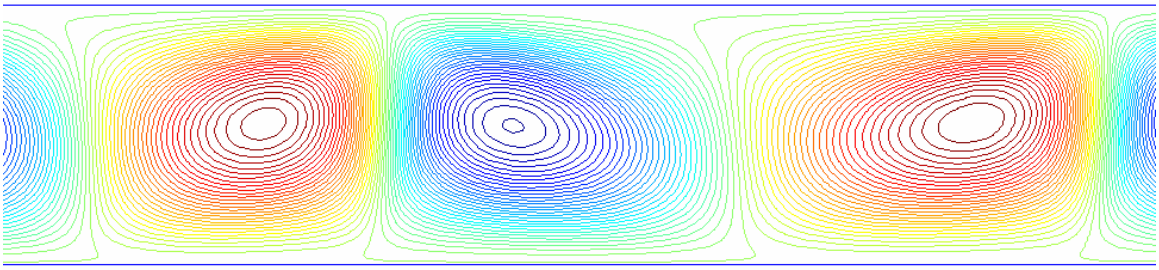

(b) Ta=200

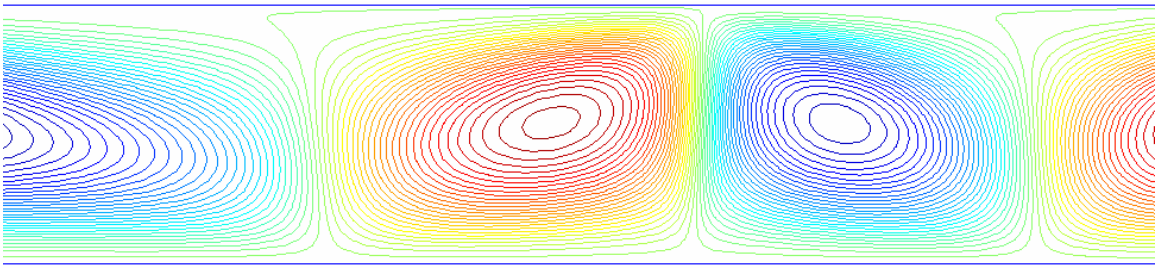

(c) Ta=400

Figure 5.7 Stream function for different Taylor numbers in the moving frame (subtracted by 1.17 times the average axial velocity)

According to Figure 5.7, the winding part decreases with the increase in Taylor number. The latter results in the increase in log reduction. Moreover, the fluence distribution function in Figure 5.8 confirms these results since the fluence distribution function becomes narrower and higher with the increase in Taylor number.

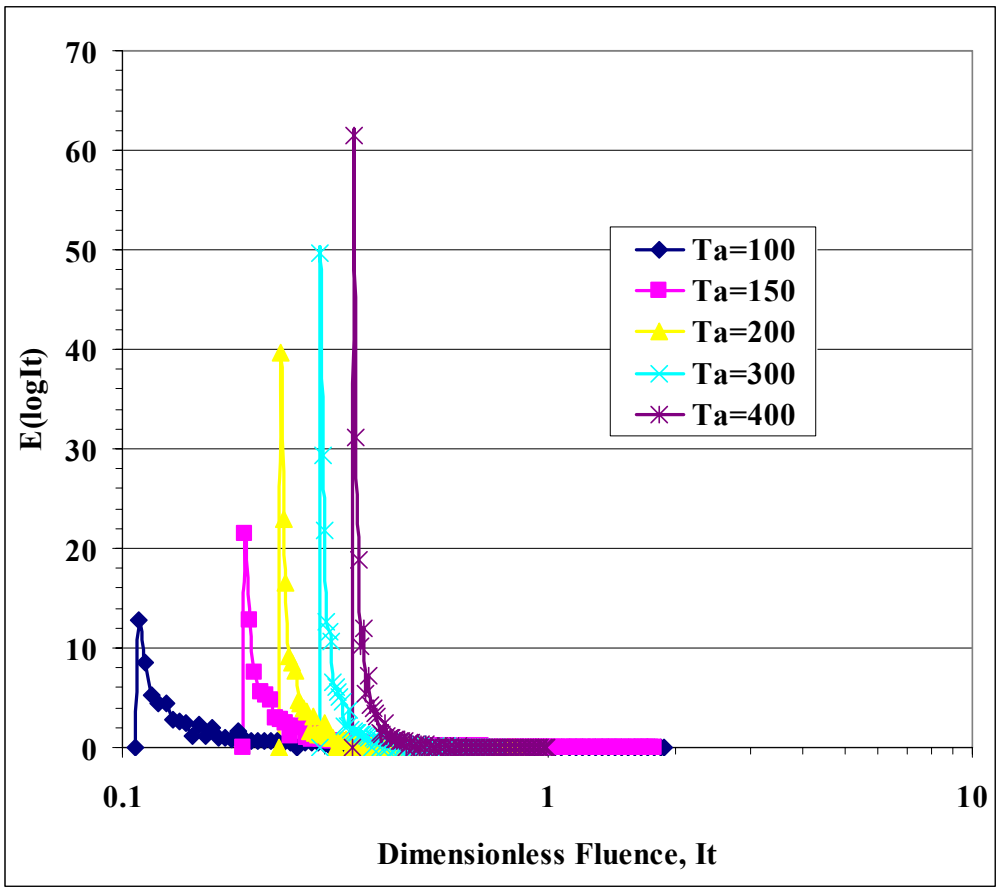

Figure 5.8 Dimensionless fluence distribution function for different Taylor numbers

Log Reduction with Different Flow Rates

Figure 5.9 is the comparison between experimental results and 2D simulations at Ta=300 with different flow rates (or average residence times) when the Taylor number is fixed and an absorption coefficient A=11 cm^{-1}. Figure 5.9 shows that 2D simulations agree well with experimental results when the average residence time is shorter than 58 seconds (or flow rate is larger than 40 mL/min). However, when the average residence time is longer than 58 seconds, there is a large deviation between 2D simulations and

experiments. Besides experimental errors, the deviation is caused by the difference between 2D and 3D simulations and the varying viscosity of water.

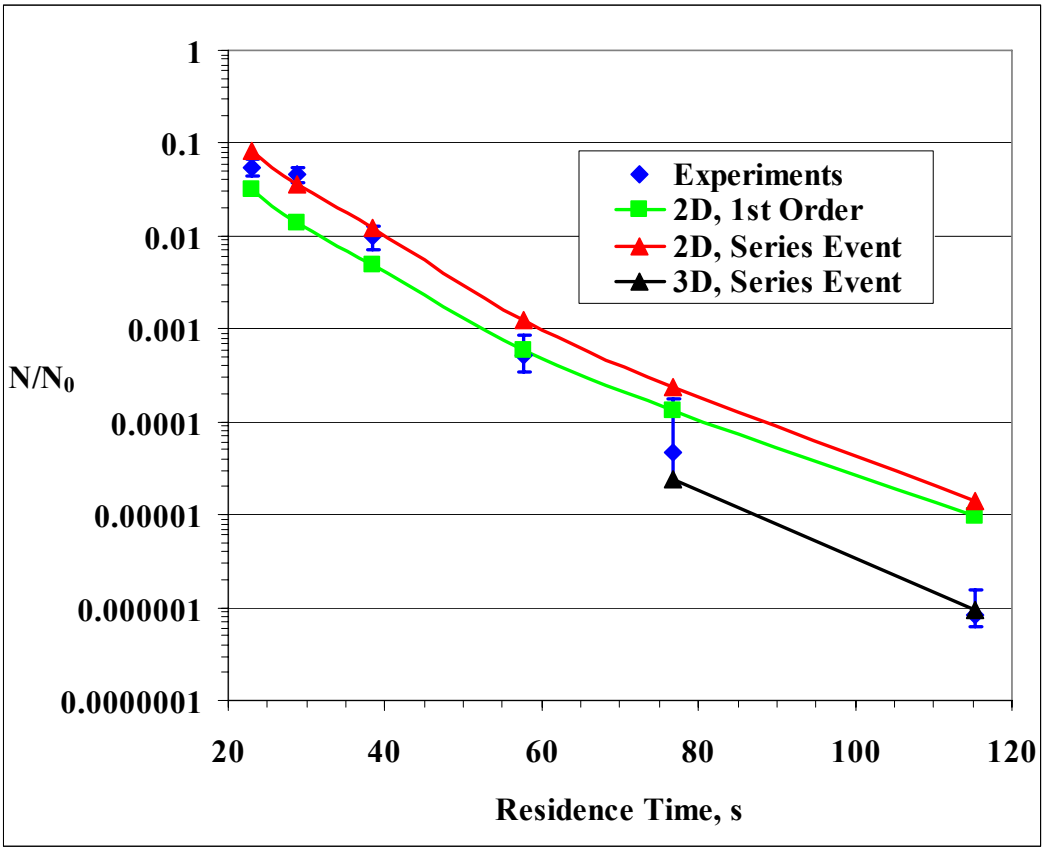

Figure 5.9 Comparison between experimental results and 2D simulations with different residence times when Ta=300 and A=11 cm^{-1}

To elaborate, the first cause of the deviation may be the difference between 2D and 3D simulations. The 3D simulation results prove that the log reduction is 6.03 when Q=20 mL/min. (residence time 115 s). The latter result can be compared with the average log reduction of experimental results which is 6.08. When Q=30 mL/min. (residence time 77 s), similar results can be obtained. The log reduction of the 3D simulation with Q=30 mL/min. is 4.61 while the average log reduction of experimental results is 4.32.

Another possible cause of the deviation is the varying viscosity of water. In the numerical simulation, the viscosity of water is assumed to be a constant, 0.001003 Pa · s

at 68 ^{o}F. Actually, the viscosity of water strongly depends on temperature. When Q=20 mL/min and the inlet temperature was 68 ^{o}F, the measured temperature at the outlet was about 90 ^{o}F. If an average temperature of 79 ^{o}F and an average viscosity of 0.8773E-3 Pa · s are used, the log reduction with reduced viscosity increases by about 0.1. Therefore, the deviation caused by the varying viscosity of water is insignificant in the prediction of inactivation levels.

Figure 5.10 is the fluence distribution function with different flow rates. It is shown that the fluence distribution is nearly independent of the flow rates. This confirms the results in Figure 5.9 where the log reduction has a nearly linear relationship with average residence time.

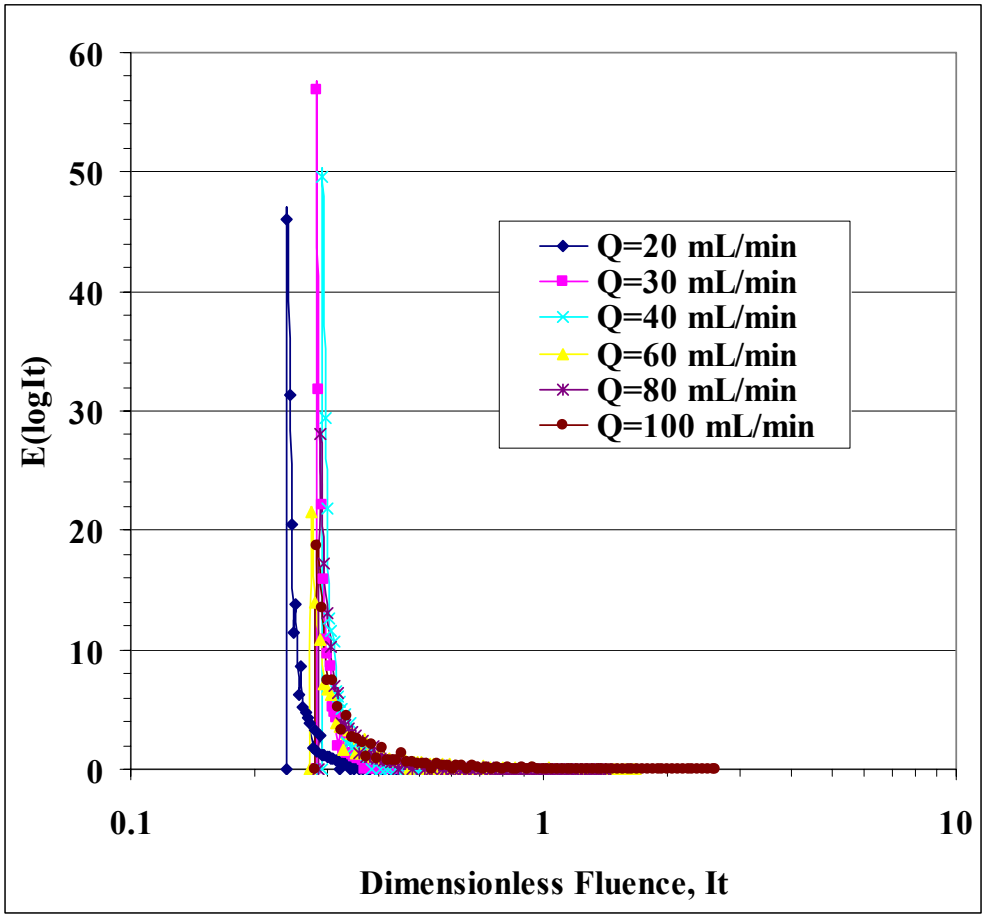

Figure 5.10 Dimensionless fluence distribution function with different flow rates

Log Reduction with Different Absorption Coefficients

Figure 5.11 is the comparison between experimental results and 2D simulations with different penetration depths (the reciprocal of the absorption coefficient) when Ta=300 and Q=40 mL/min. The resulting fluence distribution function is shown in Figure 5.12. It is shown in Figure 5.12 that the fluence distribution becomes narrower and higher with the decrease in the absorption coefficient. Moreover, it can be observed from Figure 5.11 that the log reduction is almost proportional to the penetration depth.

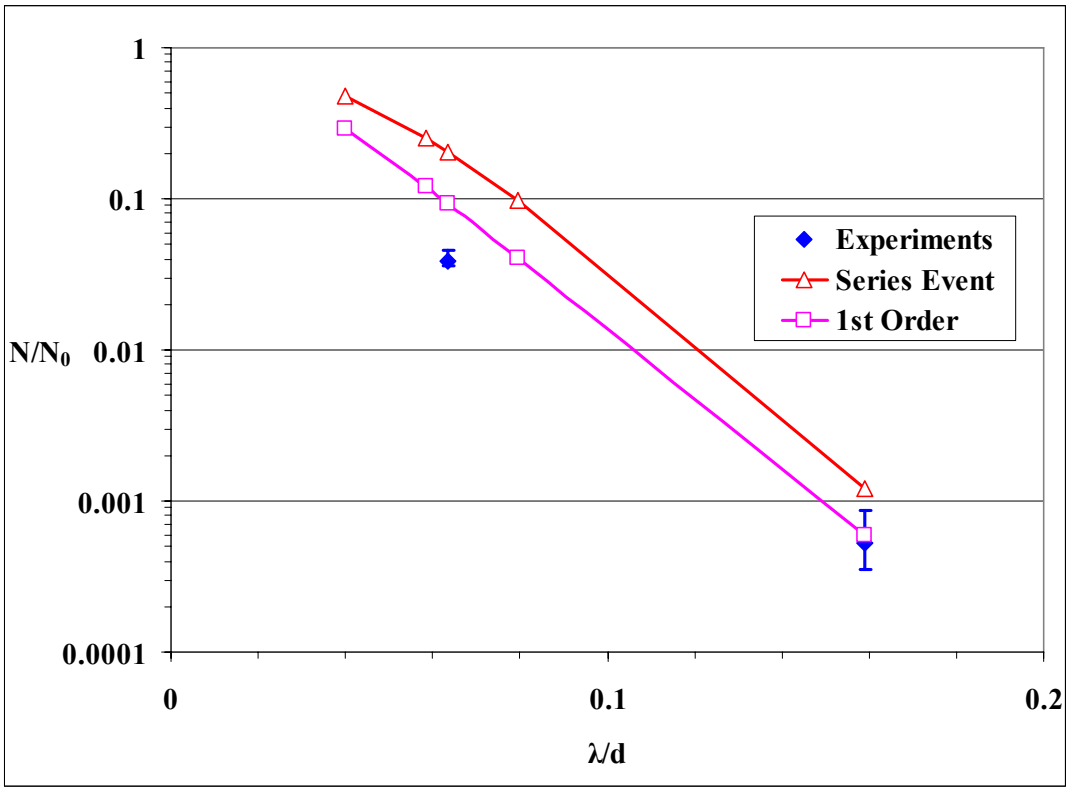

Figure 5.11 Comparison between experimental results and 2D simulations with different absorption coefficients when Ta=300 and Q=40 mL/min.

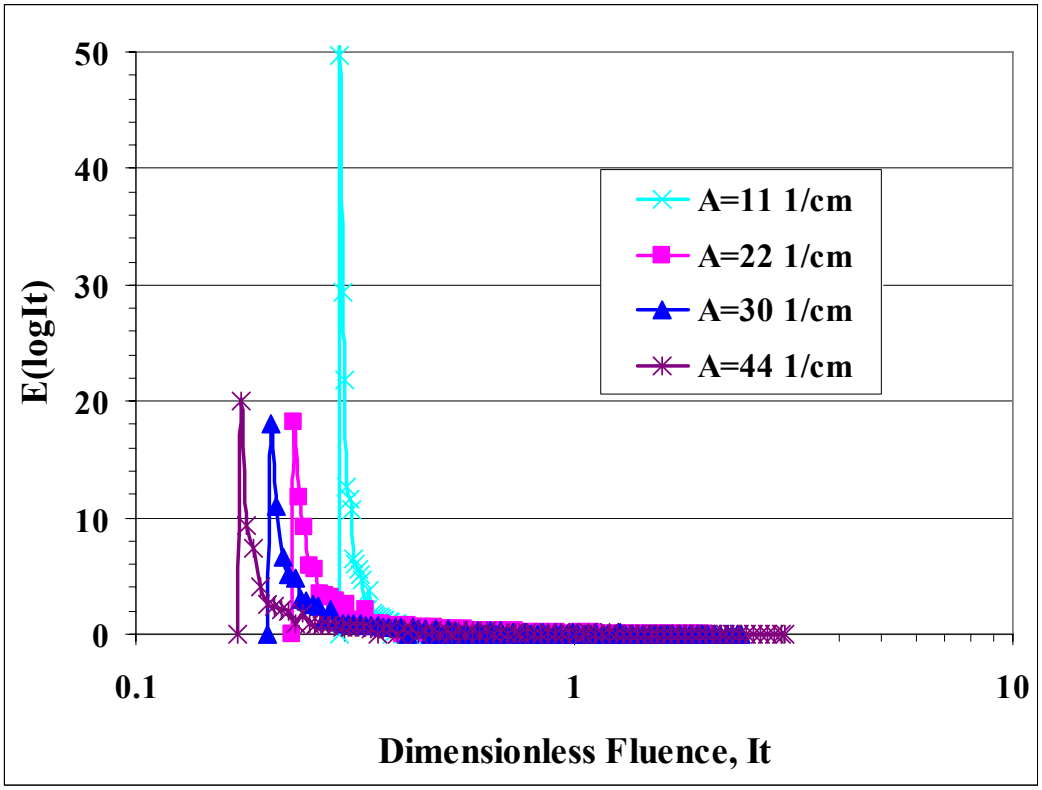

Figure 5.12 Dimensionless fluence distribution function for different absorption coefficients

5.1.3 3D Simulation Results

Although most 2D simulations agree with experimental results, there are some exceptions. 3D simulations of some example cases were conducted to compare their difference.

Cycle of Taylor-Couette Flow

Because the steam function cannot be used to show pathlines of 3D flow, the contour of axial velocities is employed. Figure 5.13 are the contours of the axial velocity of different vertical sections located around the axis of the reactor. Figure 5.14 is the contour of the axial velocity of a horizontal section in the middle of the reactor.

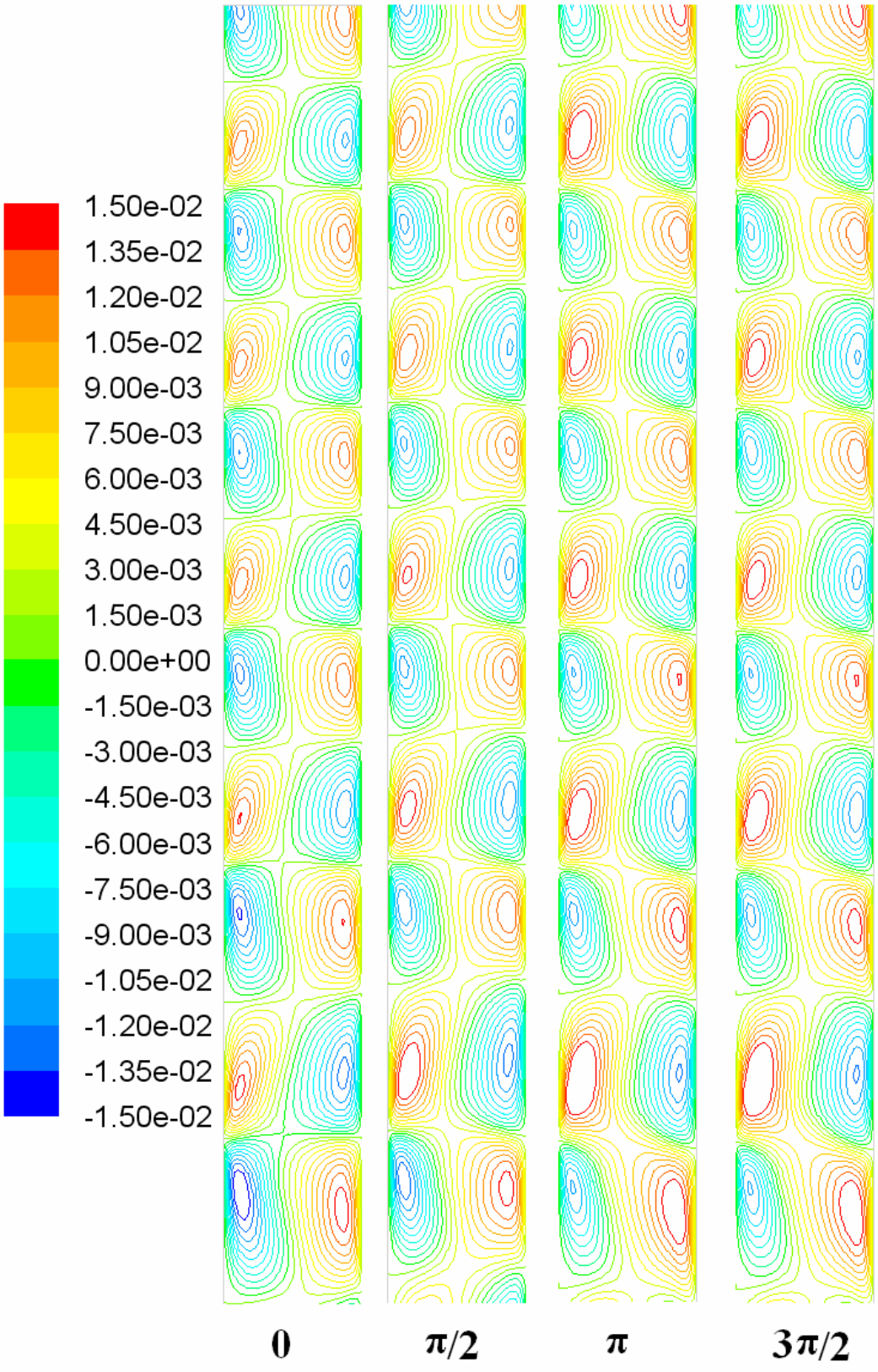

Figure 5.13 Contours of axial velocity of different vertical sections

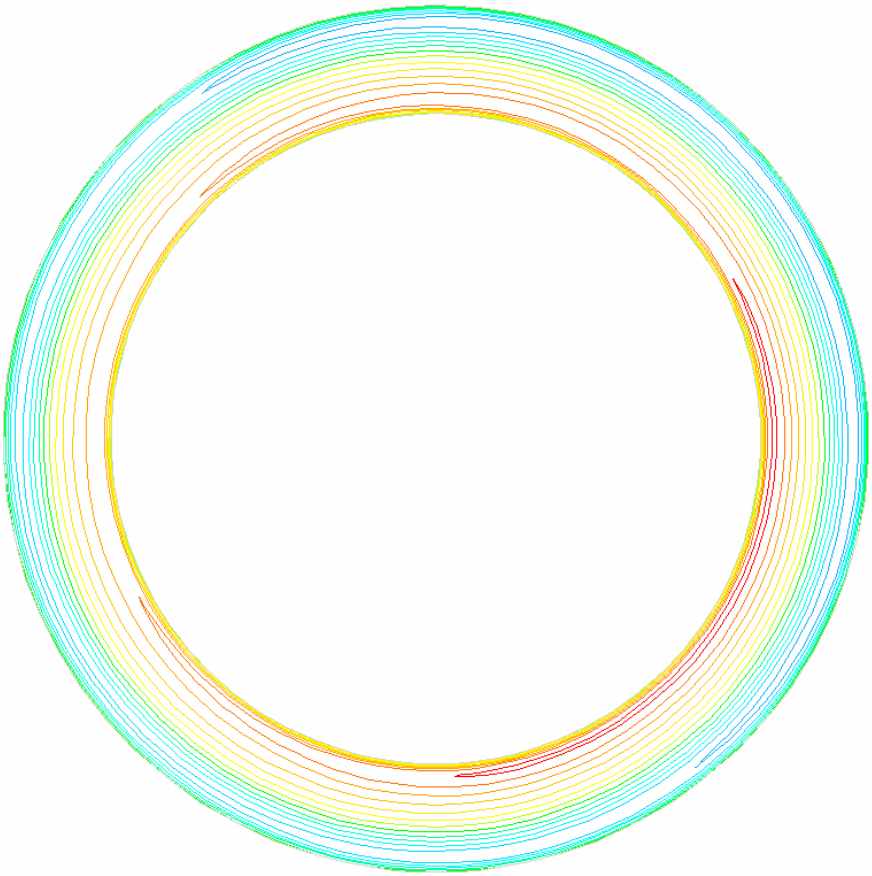

Figure 5.14 Contour of the axial velocity of the horizontal section in the middle of the reactor

According to Figures 5.14, the difference of the axial velocities among different azimuthal angles is small. Compared with the 2D flow pattern, the flow pattern of each vertical section in Figure 5.13 is similar. However, there are small differences among the vortex centers at different vertical sections. Therefore, the flow pattern at the vertical section of 3D simulations can be thought of as a 2D flow pattern at a fixed time of the 2D flow cycle, and the whole flow pattern of the 3D simulation can be thought of as combinations of 2D flow patterns at different times of the 2D flow cycle.

As in the 2D simulations, the average pathogen concentrations of the 3D simulations at the outlet of the reactor also oscillate. Figure 5.15 is the 3D average pathogen concentration at the outlet with Ta=150. As expected, one cycle of a 3D

simulation takes a shorter time than that of a 2D simulation and the oscillation becomes smaller ($N_{max}/N_{min}<2$).

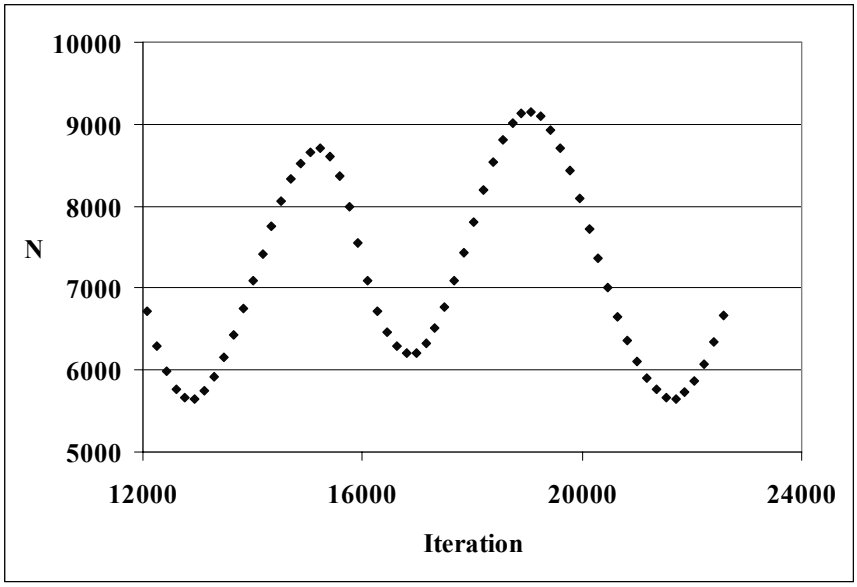

Figure 5.15 3D calculation of the average pathogen concentration at the outlet with Ta=150

Log Reduction with Different Taylor Numbers

Figure 5.16 is the comparison of log reductions among experimental results, 2D simulations and 3D simulations for different Taylor numbers when flow rates are fixed at Q = 40 mL/min. and A=11 cm^{-1}. Figure 5.16 shows that 2D and 3D simulations predict similar log reductions. The log reductions of 3D simulations are slightly higher than the 2D simulations. A possible reason is that the deviation from axisymmetrical flow for 3D flow improves the mixing in the reactor. Overall, the difference between the 2D and 3D simulations is small. Both 2D and 3D simulations give the correct qualitative predictions even when the difference is large. Therefore, 2D simulations will be used for the rest of this thesis.

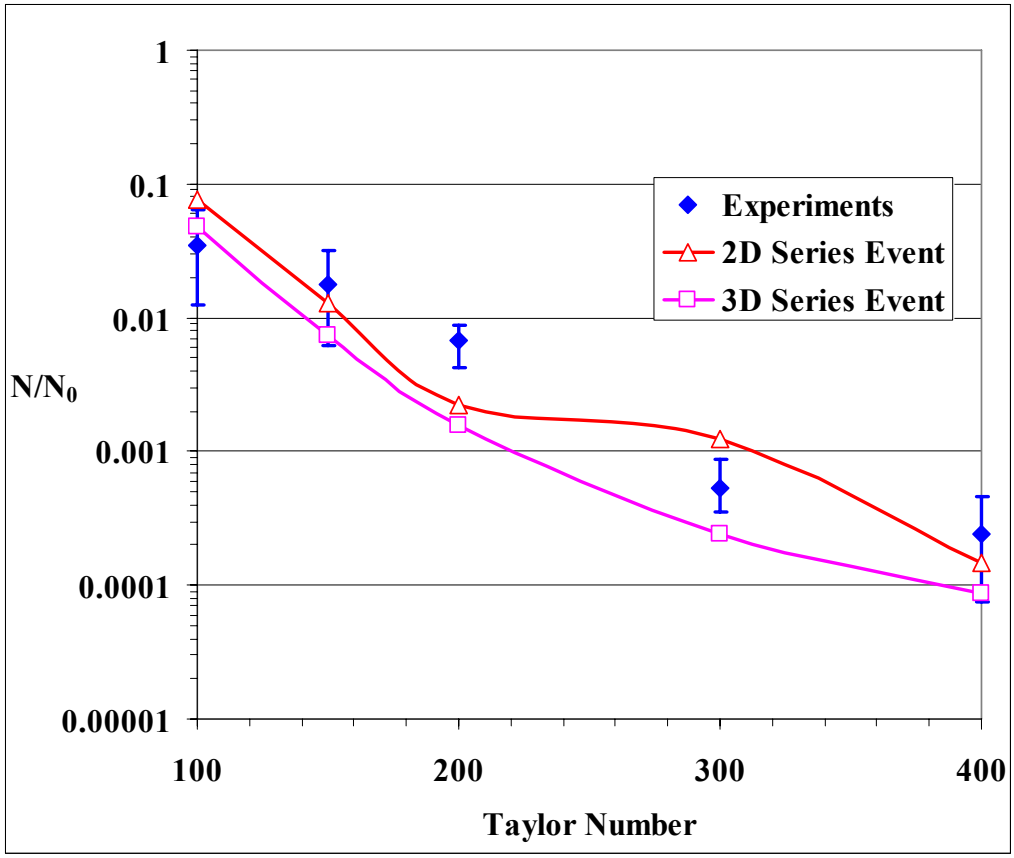

Figure 5.16 Comparison of log reduction among experimental results, 2D and 3D simulations for different Taylor numbers when Q = 40 mL/min. and A=11 cm^{-1}

5.2 Optimum Gap Width

As in the case of laminar and turbulent flow, there is an optimum gap width for each absorption coefficient in Taylor-Couette flow. Figure 5.17 shows how the log reductions change with the gap width when the length of the UV lamp is L=11.2 cm, the radius of the inner cylinder is 1.225 cm, and the radius of the outer cylinder is changed to create different gap widths. The radiation comes from the inner cylinder. In order to keep the log reductions within a comparable range for different absorption coefficients, different incident fluence rates are used, namely, I_0=4 mW/cm^2 for A=10 cm^{-1}, I_0=8 mW/cm^2 for A=20 cm^{-1}, I_0=12 mW/cm^2 for A=30 cm^{-1} and I_0=16 mW/cm^2 for A=40 cm^{-1}.

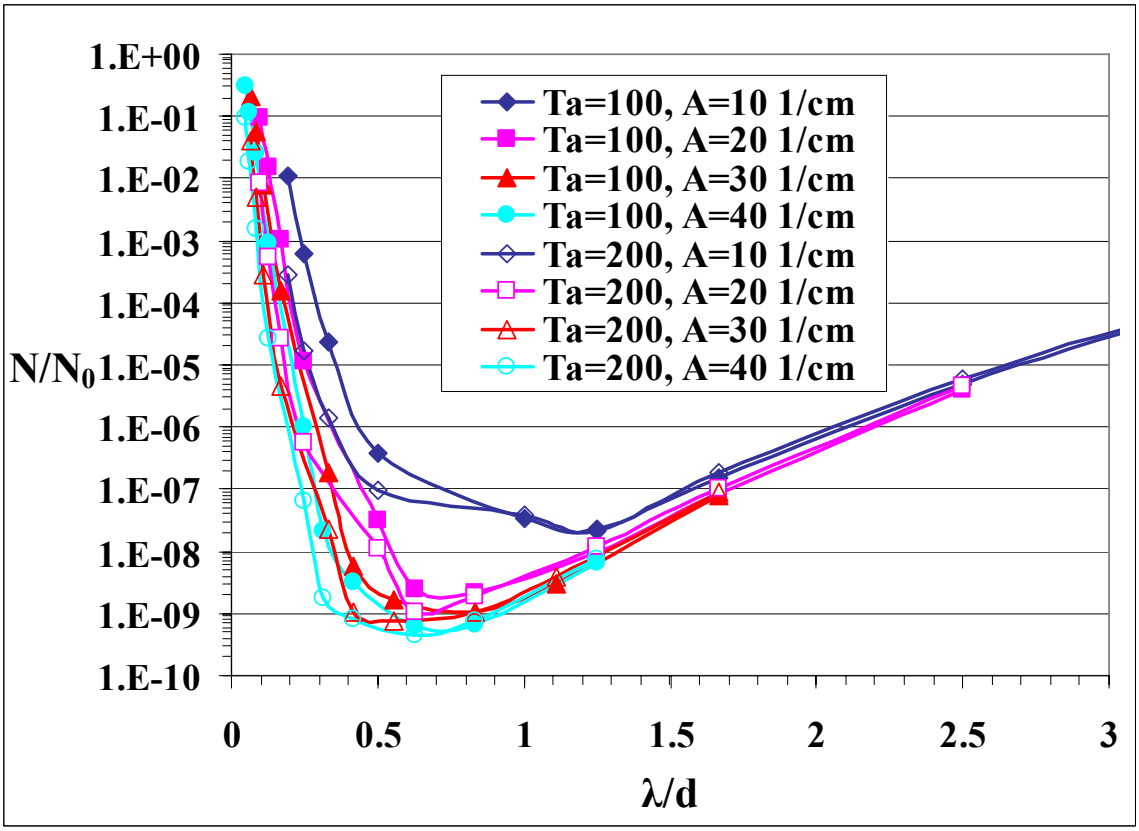

Figure 5.17 Log reduction changes with λ/d in Taylor-Couette flow

From Figure 5.17, it is shown that the optimum λ/d is similar for different absorption coefficients and Taylor numbers. Compared with 1.5 for laminar flow and 1.0 for turbulent flow, the optimum λ/d for Taylor-Couette flow decreases to around 0.5. In other words, Taylor-Couette flow requires that the radiation has to reach the middle of the gap for maximum inactivation. Moreover, if one requires an inactivation level of $N/N_0 = 10^{-5}$, the radiation penetration depth must vary over the range $0.15 < \lambda/d < 0.3$ for Ta=200. For example, if Ta=200 and A = 40 cm^{-1} ($\lambda = 0.25$ mm), then the gap width required is $d \approx 1.7$ mm.

If mixing resulting from nearly square Taylor vortices is approximately considered as the mixing between the fluid at r ($R_1 \le r \le R_2$) and the fluid at R_1+R_2-r, the profile of the fluence rate along the gap is shown in Figure 5.18. When $\lambda/d<0.5$, UV disinfection cannot benefit from mixing in the middle of vortices because mixing only

happens among regions with low fluence rates instead of between regions with both low fluence and high fluence rates.

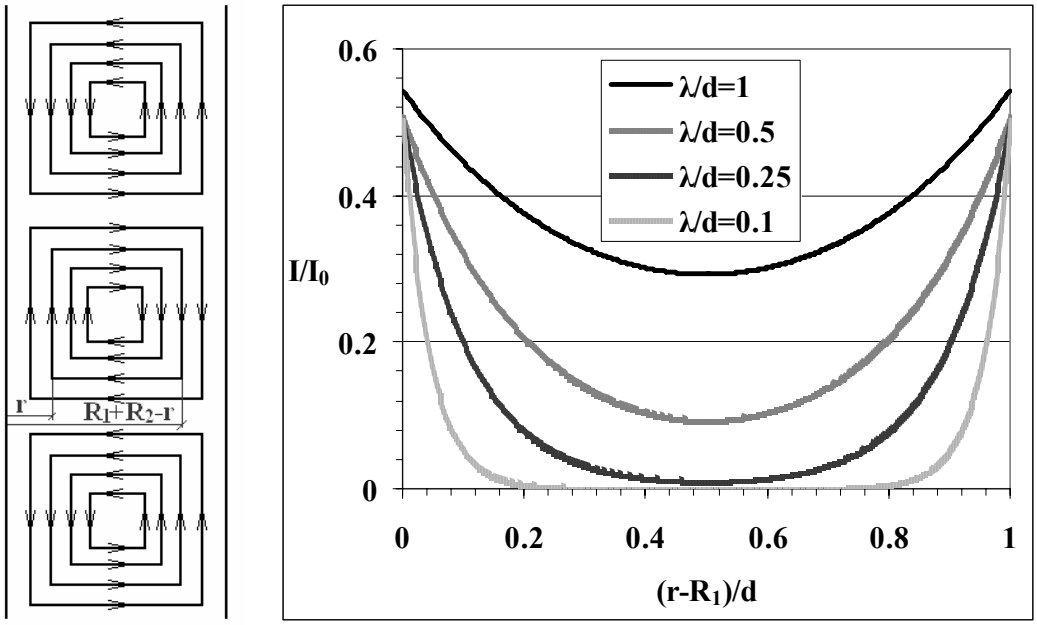

Figure 5.18 Profile of fluence rate along the gap in Taylor-Couette flow

5.3 Correlation of UV Disinfection in Taylor Vortex Reactors

A Taylor vortex reactor can be approximated as a plug flow reactor (Kataoka et al., 1975). The correlation, which is similar to equation (4.8), can be used to predict the log reduction in Taylor vortex reactors.

$$\ln\left(\frac{N}{N_0}\right) = -\frac{kI_0\tau_{av}}{\alpha d}\frac{2R_2}{R_2 + R_1} \tag{5.3}$$

In equation (5.3), a new dimensionless group Rc is introduced because of curvature effects where,

$$R_c = \frac{2R_2}{R_2 + R_1} \tag{5.4}$$

The boundary thickness δ in Taylor-Couette flow is proportional to $Ta^{-1/2}$ (Baier et al., 1999, Forney et al., 2003a, Forney and Pierson, 2003b) where,

$$\delta = \frac{2d}{\sqrt{Ta}} \tag{5.5}$$

A constant, c/δ, can be added to correct the deviation between Taylor vortex reactors and ideal PFRs where one obtains,

$$\ln\left(\frac{N}{N_0}\right) = -\frac{\mathrm{ck}I_0\tau_{\mathrm{av}}R_c}{\alpha d\delta}. \tag{5.6}$$

The experimental data are correlated according to equation (5.6) and shown in Figure 5.19, where c = 0.0125 cm is obtained by the least square method. The standard deviation of log reductions σ_y equals 0.33, and the coefficient of determination R^2 equals 0.953. Figure 5.19 shows that the correlation equation (5.5) agrees well with experimental results. This confirms what is shown in Section 5.1, that the log reduction is nearly proportional to the average residence time and the reciprocal of the absorption coefficient (the penetration depth).

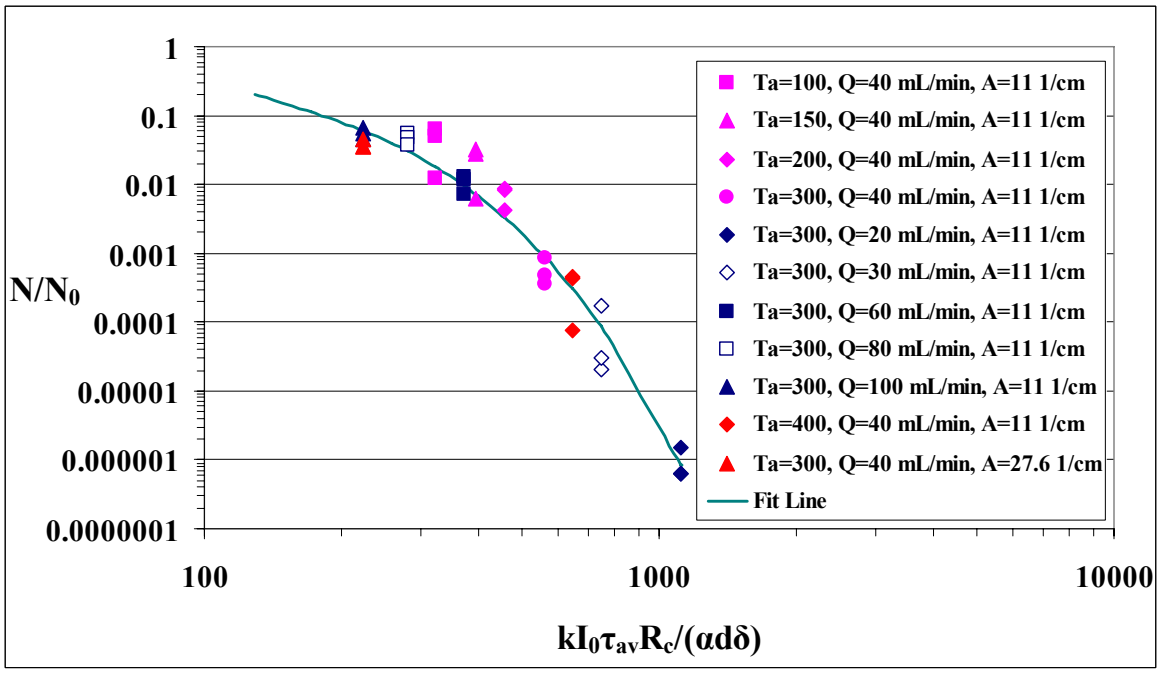

Figure 5.19 Correlation of UV disinfection in Taylor vortex reactors

Compared with the correlation equation (4.10) for UV disinfection in turbulent reactors, the correlation equation (5.6) for UV disinfection in laminar Taylor vortex reactors has the same form. The only difference is the definition for the boundary layer thickness where δ is defined by equation (4.11) for turbulent flow and equation (5.5) for laminar Taylor-Couette flow. The experimental data of both turbulent reactors and laminar Taylor vortex reactors are correlated with the same dimensionless group and shown in Figure 5.20, where the constant c = 0.0125 cm in equation (5.6) for the solid line is obtained by the least squares method. The standard deviation of log reductions σ_y equals 0.283, and the coefficient of determination R^2 equals 0.973.

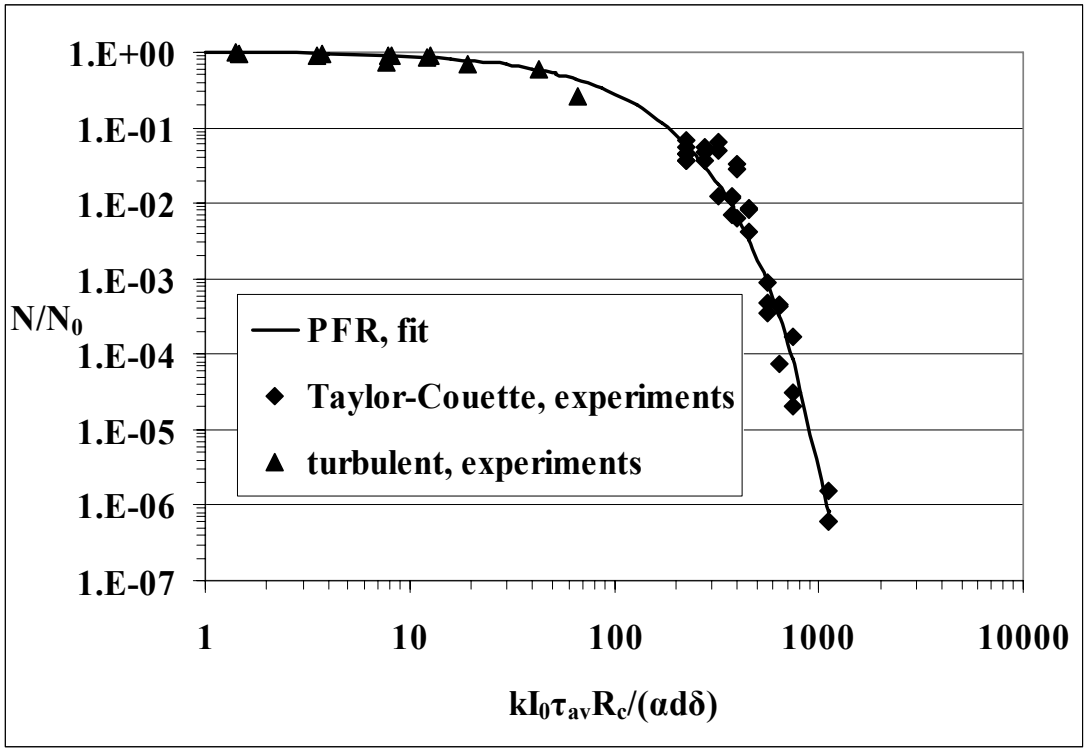

Figure 5.20 Correlation of experimental data of UV disinfection in turbulent reactors and laminar Taylor vortex reactors

Figure 5.20 shows that the same correlation equation can be applied to UV disinfection in turbulent reactors and laminar Taylor vortex reactors. Similarly, the

numerical results of both turbulent reactors and laminar Taylor vortex reactors are correlated with equation (5.6) and are shown in Figure 5.21.

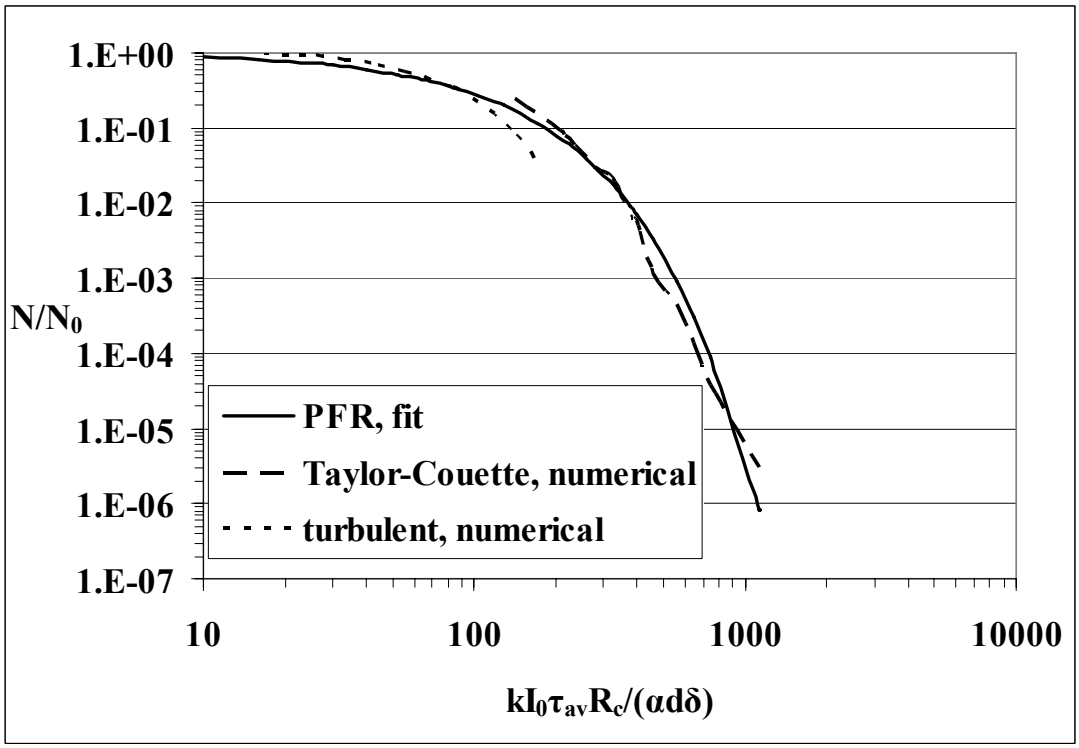

Figure 5.21 Correlation of numerical results of UV disinfection in turbulent reactors and laminar Taylor vortex reactors

5.4 Comparison among the Three Flow Patterns

5.4.1 Log Reductions

Because of the different requirements for the three flow patterns (laminar, turbulent and Taylor-Couette), it is impossible to compare log reductions under the same conditions such as the flow rate. However, if the same cylinder radii, absorption coefficient, pathogen and $I_0\tau_{av}$ are used, the same log reduction should be achieved if the behavior of all reactors approaches that of a PFR. The log reduction is of the form,

$$\ln\left(\frac{N}{N_0}\right) = f\left(\frac{kR_c I_0 \tau_{av}}{\alpha d}\right) \tag{5.7}$$

Figure 5.22 is the comparison of log reductions among the three flow patterns, where the radius of the inner cylinder is 1.225 cm and series-event inactivation model of of *E. coli* is used. The radius of the outer cylinder is changed from 1.235 cm to 1.74 cm in order to create different gap widths.

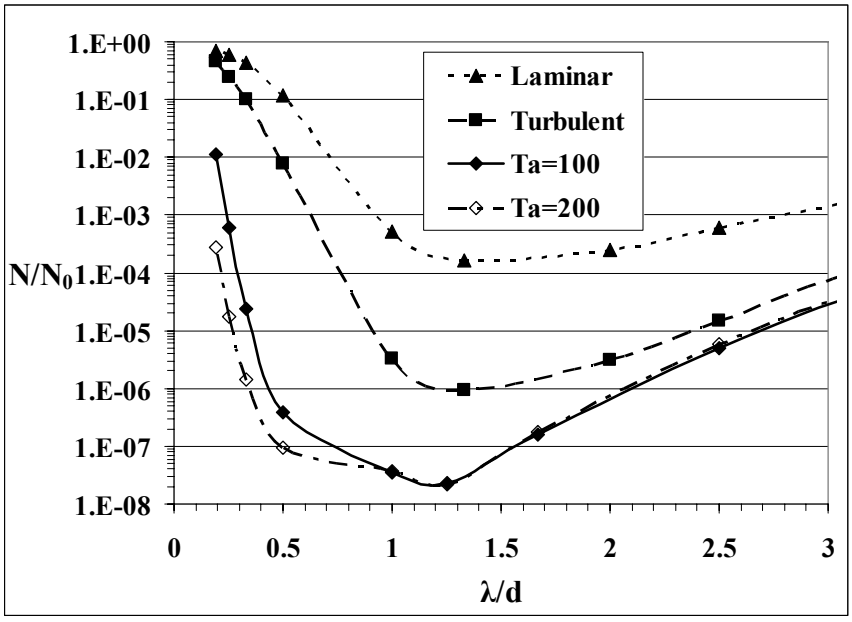

(a) A=10 cm^{-1}, $I_0\tau_{av}$=716.4 mJ/cm^2

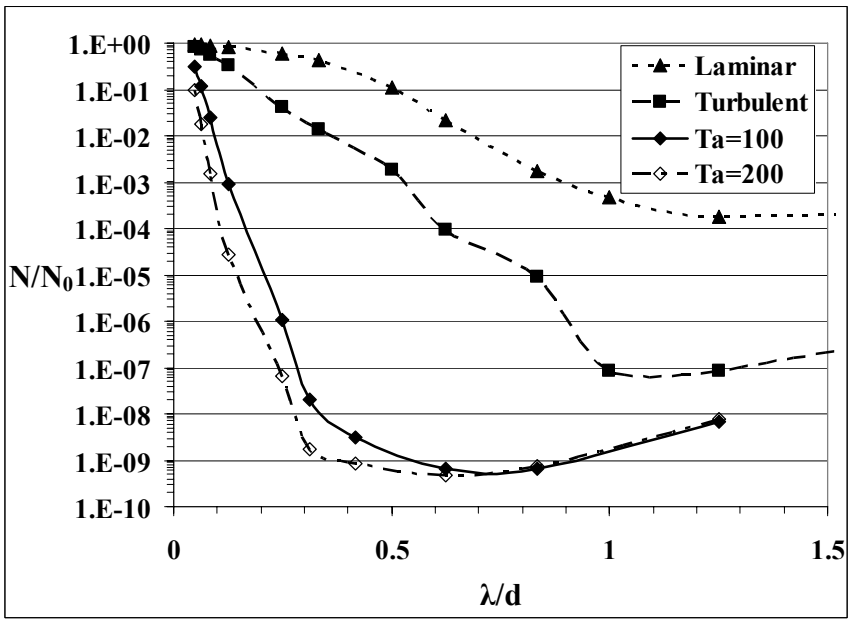

(b) A=40 cm^{-1}, $I_0\tau_{av}$=2865.6 mJ/cm^2

Figure 5.22 Comparison of log reductions among three flow patterns

According to Figure 5.22, laminar Taylor-Couette flow is superior to either turbulent or laminar flow in the following aspects:

1. Taylor-Couette flow always achieves a higher log reduction than either laminar or turbulent flow with the same $I_0\tau_{av}$ and other conditions. For example, when A=40 cm^{-1} and $\lambda/d=0.417$, the inactivation levels N/N_0 are 8.2×10^{-10}, 8.1×10^{-3} and 0.27 for Taylor-Couette flow (Ta=200), turbulent flow and laminar flow, respectively. Both turbulent and laminar flows achieve very low inactivation levels when the absorption coefficients of juices are high and λ/d is small. For example, when A=40 cm^{-1} and $\lambda/d=0.049$, the inactivation levels N/N_0 are 0.81 and 0.95 for turbulent flow and laminar flow, respectively. However, $N/N_0 = 0.097$ for Taylor-Couette (Ta=200).
2. The optimum λ/d for Taylor-Couette flow is reduced to 0.5. However, the optimum λ/d is 1.5 for laminar flow and 1.0 for turbulent flow, respectively. The two advantages of Taylor-Couette flow are: (1) The pressure drop of Taylor-Couette flow is decreased. (2) Taylor-Couette flow is suitable for disinfecting juices with high absorption coefficients.

Figure 5.23 is the fluence distribution function of the three flow patterns when $\lambda/d=0.25$ and the absorption coefficient equals 10 cm^{-1}. According to this figure, Taylor vortex reactors approach the characteristics of a PFR. For turbulent flow, there are three peaks. The left one corresponds to the viscous sublayer on the opposite side of the radiation source, the right one corresponds to the viscous sublayer near the radiation source, and the middle one corresponds to the fully turbulent region and the buffer layer between the viscous sublayer and the fully turbulent region.

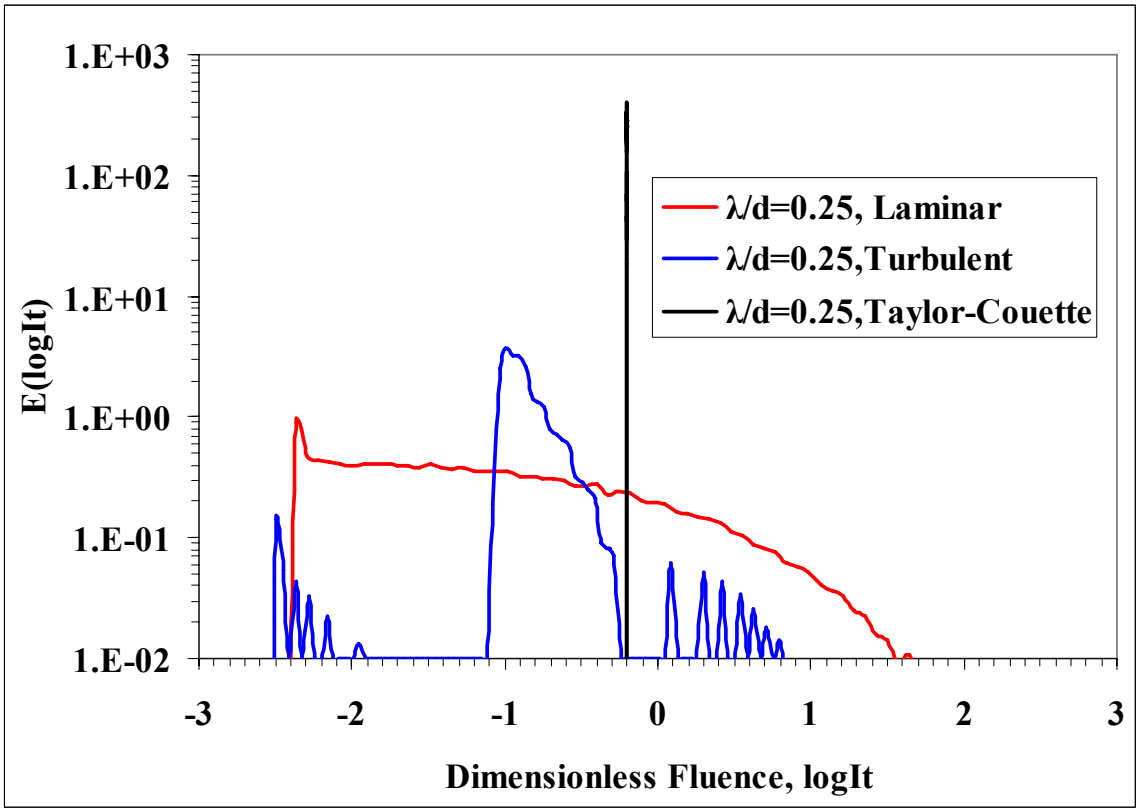

Figure 5.23 Fluence distribution function of the three flow patterns when λ/d=0.25 and absorption coefficient equals 10 cm^{-1}

5.4.2 Comparison of the Three Flow Patterns

Laminar Reactors

Laminar reactors are simple structures because there are no moving parts. However, because there is no radial mixing in laminar Poiseuille flow, the optimum gap width is very narrow. Inactivation levels decrease sharply if the gap width of the reactor is wider than the optimum. Therefore, laminar reactors are suitable only for water or wastewater, where the absorption coefficient is low and relatively constant.

Turbulent Reactors

Turbulent reactors have no moving parts similar to laminar designs. The disadvantage of turbulent reactors is that the high flow rate to ensure turbulent flow is

coupled with a reduced residence time. Achieving a 5 log reduction requires a very long lamp in a single-lamp turbulent reactor, or many turbulent reactors connected in series. Thus, capital investment is increased. Turbulent reactors only perform well when the radiation penetration depth of juices is larger than boundary layer thickness. Furthermore, in most situations the absorption coefficients of juices are so high that the radiation is unable to penetrate the whole gap and inactivate pathogens in the viscous sublayer on the opposite side of the radiation source. One solution is to connect UV reactors in series. Pathogens within the sublayer in the first UV reactor may be mixed into the fully turbulent regime in the next UV reactor. Given these facts, turbulent reactors are only suitable for processing large quantities of juice where the penetration depth is larger than the boundary layer thickness.

Taylor Vortex Reactors

Rotation of the fluid along with the creation of Taylor vortices reduces the boundary layer thickness which improves inactivation levels. Laminar Taylor-Couette flow makes it possible to decouple mixing and fluid residence times. Numerical results indicate that the optimum gap width is twice as large as the penetration depth of juice. Moreover, the inactivation level of Taylor vortex reactors does not decrease sharply if the gap width deviates from the optimum value. Taylor vortex reactors are suitable for processing juices with high absorption coefficients. The only disadvantage of the Taylor vortex reactor is that there is one moving part, namely the rotor (the inner cylinder).

5. 5 Turbulent Taylor-Couette Flow

As introduced in Section 1.2, the flow pattern in the annular gap will change from laminar Taylor-Couette flow to turbulent Taylor-Couette flow with the increase in Taylor number. Figure 5.24 are the log reductions including laminar and turbulent Taylor-Couette flow. In Figure 5.24, the axial Reynolds numbers are 6.41 and 12.82 for flow

rates 0.3 mL/s and 0.6 mL/s, respectively. The radii of the inner and outer cylinder are 1.225 cm and 1.74 cm, respectively. The length of the UV lamp is 11.2 cm and UV is irradiated from the inner cylinder with an intensity of 12 mW/cm^2. The series-event inactivation model of *E. coli* is used, and the absorption coefficient is assumed to be A=20 cm^{-1}. When Ta=600, the conditions are close to the transition point from laminar to turbulent Taylor-Couette flow. According to Figure 1.9, it is difficult to determine the exact Taylor number at which the transition from laminar to turbulent flow occurs. In this study both laminar and turbulent simulation results are provided.

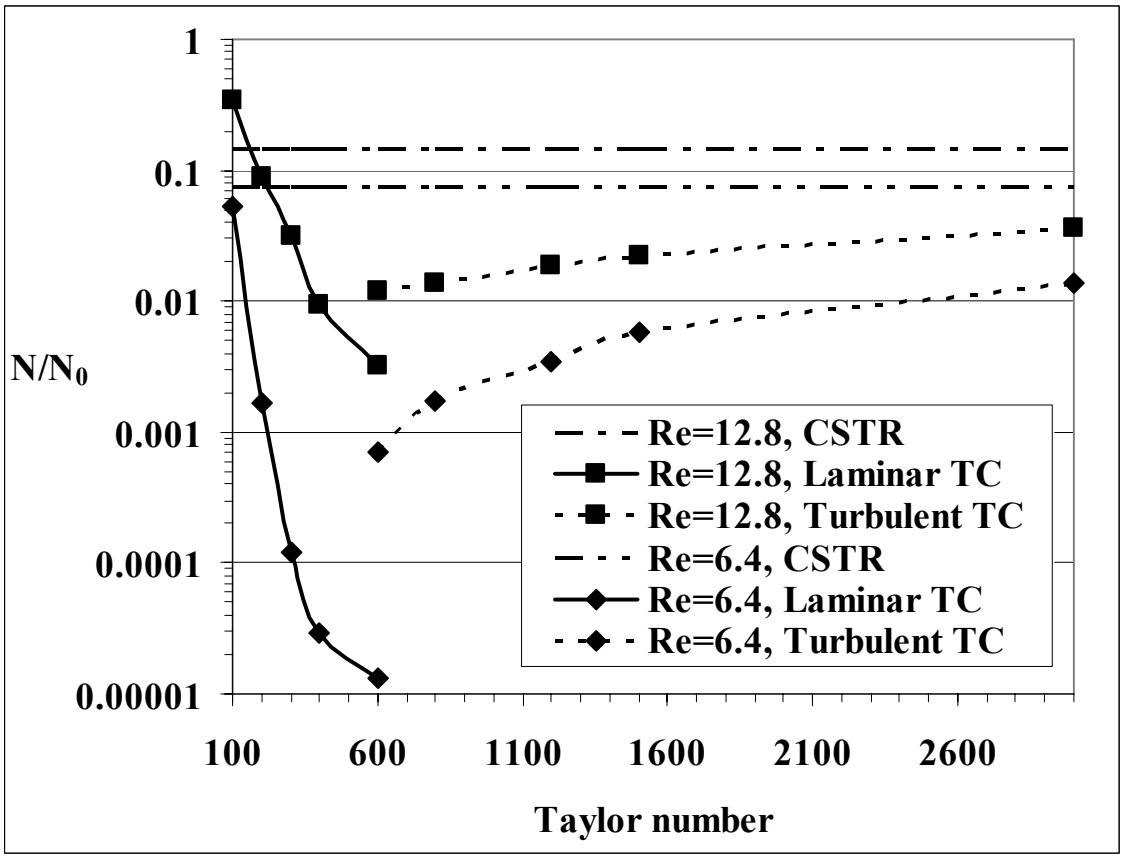

Figure 5.24 Log reductions including laminar and turbulent Taylor-Couette flow

In laminar Taylor-Couette flow, the inactivation levels increase with Taylor number as shown in Section 5.1. From Figure 5.24, it is shown that log reductions in turbulent Taylor-Couette flow do not increase with Taylor number. On the contrary, the log reduction in turbulent Taylor-Couette flow will decrease with an increase in Taylor

number. The latter is caused by axial turbulent mixing. Turbulent flow is a three dimensional flow and intensifies mixing along all directions. Radial mixing is absolutely necessary to improve the performance of thin film annular reactors. However, turbulent Taylor-Couette flow increases both the radial and axial mixing where the latter should be avoided in the thin film annular reactors.

The axial mixing at large Ta number is a kind of back mixing and will reduce disinfection results. With the increase in Taylor number in turbulent Taylor-Couette flow, the flow pattern is approaching that of a continuous stirred tank reactor (CSTR) (Resende et al., 2004). By contrast, the axial mixing is negligible in laminar Taylor-Couette flow which can be approximated by a plug flow reactor (PFR) (Kataoka et al., 1975). Therefore, the Taylor vortex reactors should be operated in laminar Taylor-Couette flow and with Taylor numbers as high as possible.

5. 6 Modified Taylor-Couette Flow

Recently a number of modifications to classical Taylor vortex reactors have been investigated in order to improve the performance. These studies involve modification to the shape of the rotor (Rotz and Suh, 1979, Ikeda and Maxworthy, 1994, Wiener et al., 1997, Rafique and Lami, 2001), for example, a V-grooved rotor, or a rotor with sinusoidal modulations. In this study, the wavy rotor (see Figure 5.25) will be investigated. In Figure 5.25, the average radius of the rotor is defined as the nominal radius which is used to calculate the Taylor number in equation (5.1). The distance between the highest point of the rotor and the nominal radius of the rotor is defined as the wave amplitude, h, and the distance between the two highest points as the wavelength of the rotor, Lw.

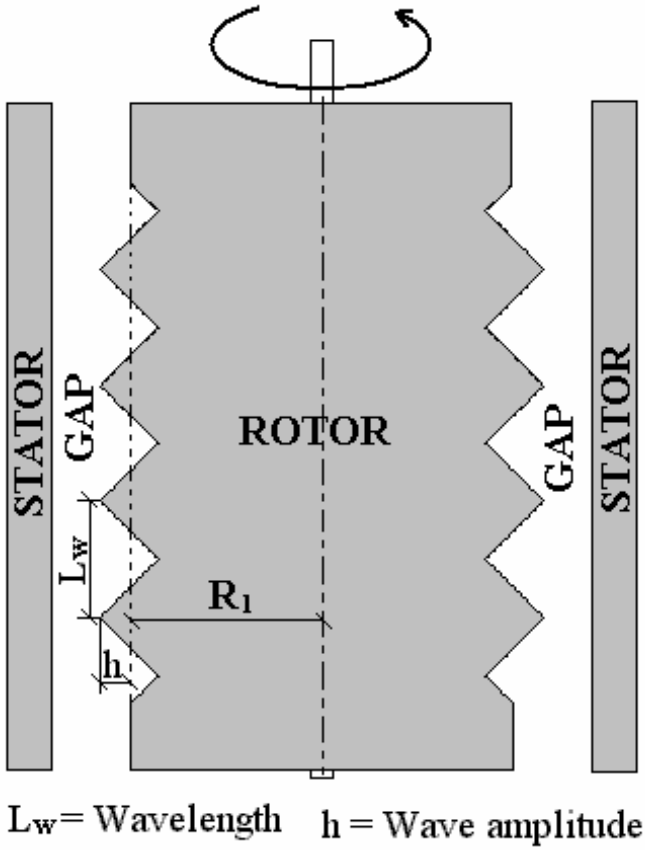

Figure 5.25 Schematic figure of a wavy rotor

5.6.1 Stream Function of Wavy Rotors

Figure 5.26 is the stream function of wavy rotors. The radius of the stator is 2.275 cm, and the nominal radius of the rotor is 2.075 cm corresponding to a nominal gap width of 2 mm. The flow rate equals 13.1 mL/min.

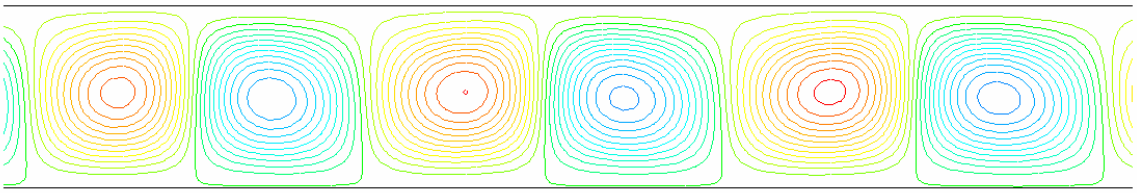

(a) Flat Rotor --- continued

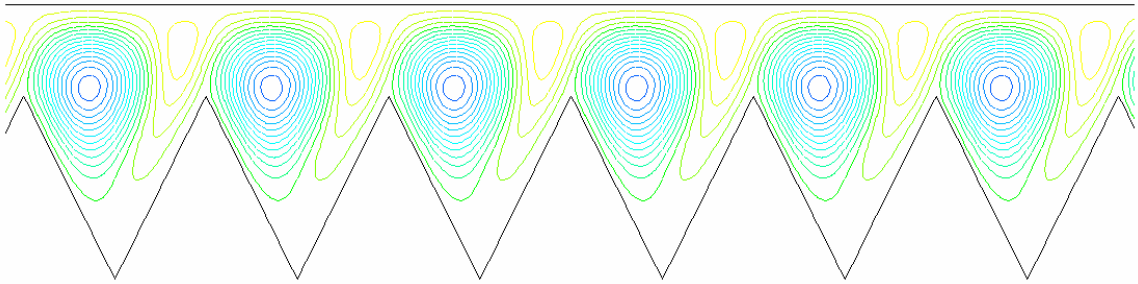

(b) Wavelength = 2mm and wave amplitude = 1mm

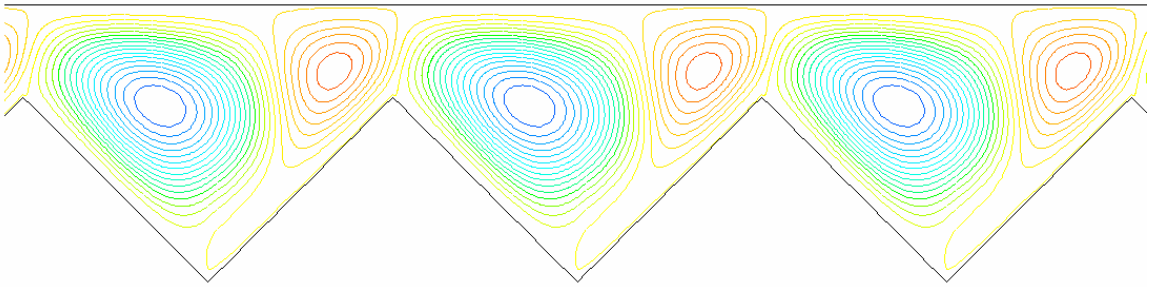

(c) Wavelength = 4mm and wave amplitude = 1mm

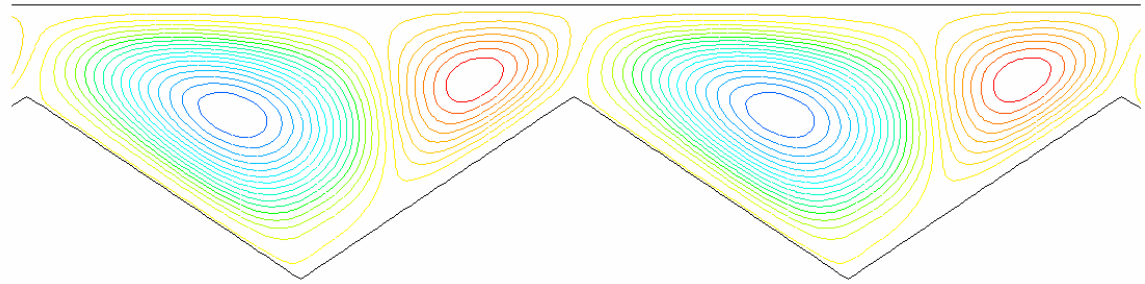

(d) Wavelength = 6mm and wave amplitude = 1mm
Figure 5.26 Stream function of wavy rotors

For flat rotors, vortices are nearly square and appear periodically in the form of counter-rotating pairs. The number of vortices within a radiation section for flat rotors is approximately the ratio of the UV lamp length to the gap width, namely L/d. When wavy rotors are used, vortices still appear periodically according to Figure 5.26. However, unlike flat rotors, the number of vortices with wavy rotors within the radiation section is no longer determined by the ratio of the UV lamp length to the gap width. Instead, the number of vortices for a wavy rotor equals two times the ratio of the UV lamp length to the wavelength of the rotor, namely 2L/Lw. Another interesting flow pattern is that there

are two vortices within one rotor wavelength period: one is relatively large, another relatively small.

5.6.2 Log Reductions of Wavy Rotors

Figure 5.27 are the log reductions of different wavy rotors. Straight lines are the log reductions with flat rotors. In order to keep log reductions within a comparable range for different absorption coefficients in Figure 5.27, different incident fluence rates are used, namely, I_0=1.5 mW/cm^2 for A=5 cm^{-1}, I_0=3 mW/cm^2 for A=10 cm^{-1} and I_0=9 mW/cm^2 for A=30 cm^{-1}. The fluid is irradiated from the outer cylinder, and the series-event inactivation model of *E. coli* is used. Other fixed parameters are Ta=100, and the length of UV lamp equals 5.7 cm.

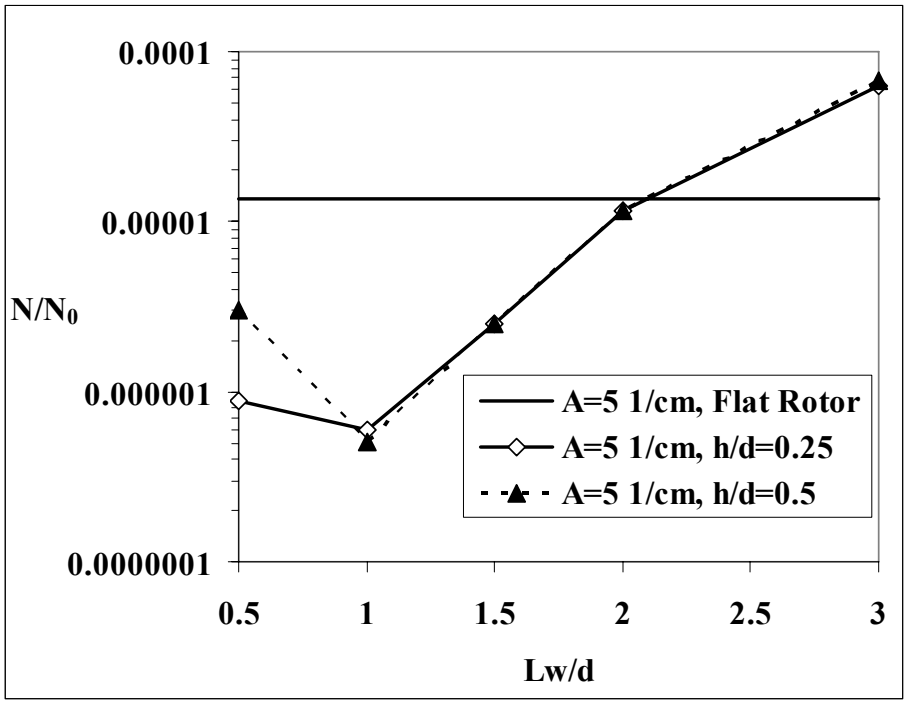

(a) A=5 cm^{-1} --- continued

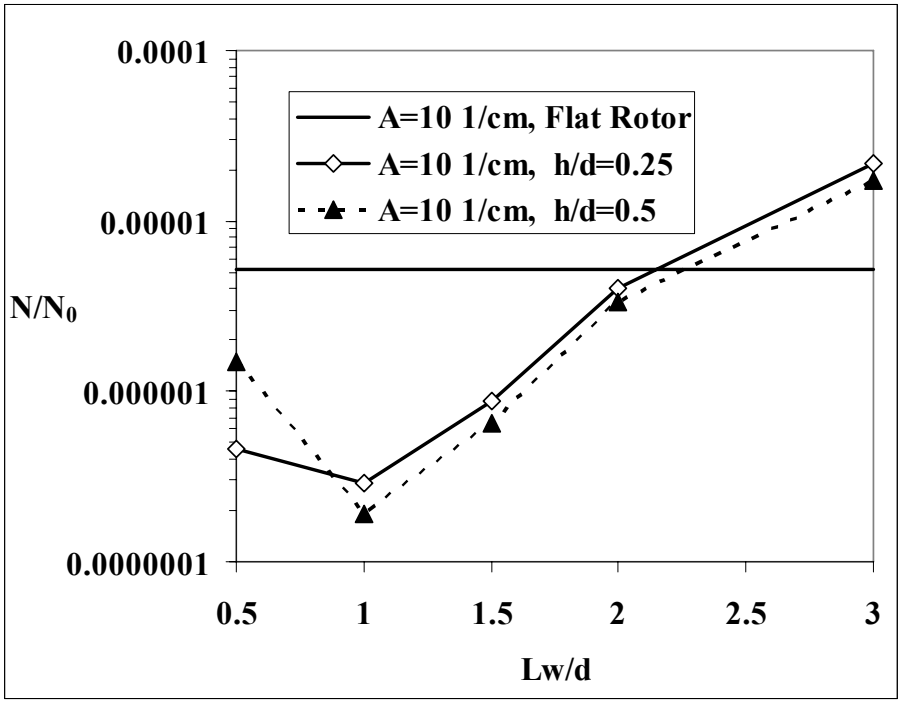

(b) A=10 cm^{-1}

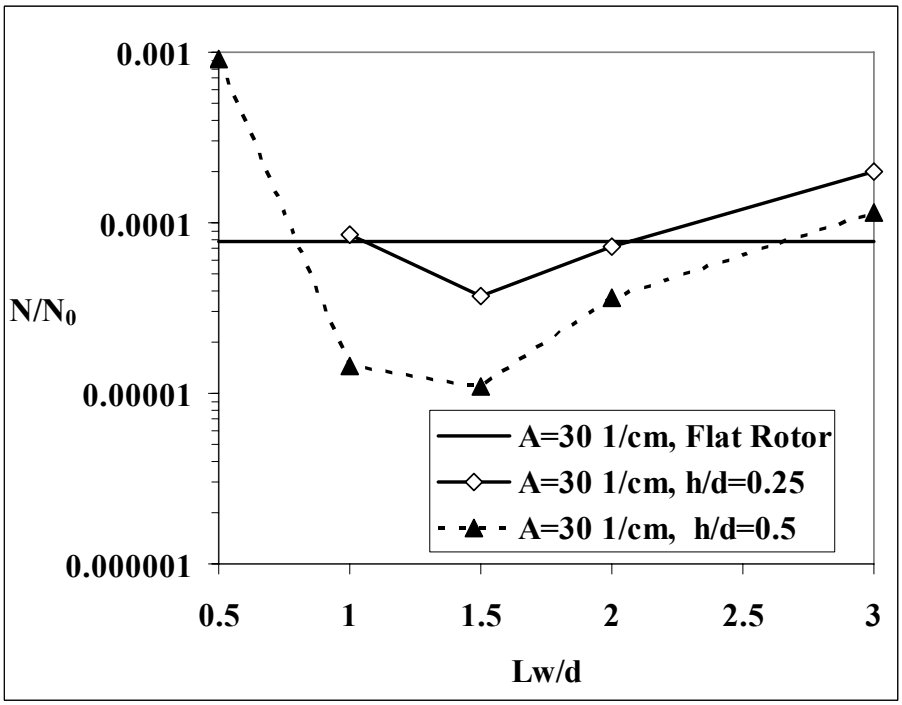

(c) A=30 cm^{-1}

Figure 5.27 Log reductions of different wavy rotors

Because the vortices improve radial mixing, more vortices imply better radial mixing. The number of vortices with the wavy rotor within a radiation section equals 2L/Lw, and the number of the vortices with the flat rotor equals L/d. When Lw/d = 2, the number of vortices with the wavy rotor is the same as that with the flat rotor (2L/Lw = L/d), which results in similar log reductions for the wavy rotor and the flat rotor as shown in Figure 5.27. When Lw/d > 2, 2L/Lw will be less than L/d. For example, when Lw/d = 3, Figure 5.27 shows that the log reduction levels with the wavy rotor will be lower than those of the flat rotor because of fewer vortices. Therefore, Lw/d should be less than 2 for the wavy rotor in order to achieve higher log reduction levels than the flat rotor.

However, decreasing wavelengths cannot increase log reductions indefinitely. For example, Figure 5.27 shows that the log reductions with Lw/d = 0.5 are less than those with Lw/d =1. One important reason is that the rule, the number of vortices equals 2L/Lw, is no longer valid when Lw/d is less than a certain value. An example is Figure 5.28 where the stream function is shown for a wavy rotor with Lw/d =0.5. Normally, there are two vortices within one wavelength period. However, Figure 5.28 shows there is only one vortex within each wavelength period.

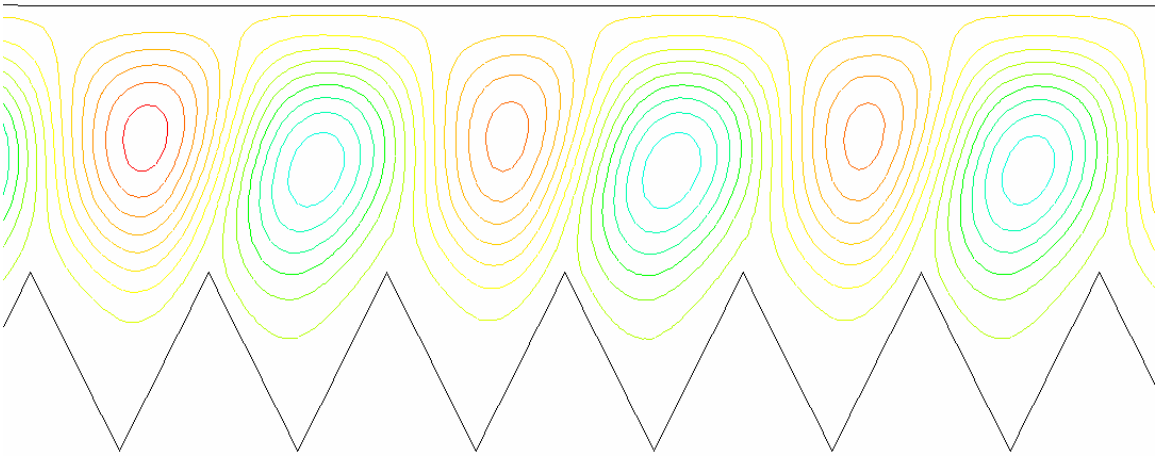

Figure 5.28 Stream function of a wavy rotor with Lw/d = 0.5

From Figure 5.27, one observes that decreasing wavelengths and increasing wave amplitudes can improve the performance of reactors even if the gap width is not near the optimum width. Figure 5.29 is the fluence distribution function with A=10 cm^{-1}. With either the decrease in the wavelength or the increase in the wave amplitude, the fluence peak is large. One observes that decreasing the rotor wavelength is more effective than increasing the wave amplitude because the number of vortices with wavy rotors is proportional to the reciprocal of the wavelength of the wavy rotors. Decreasing the wavelength changes the flow pattern more dramatically than increasing the wave amplitude, which means more vortices and better radial mixing. For example, when A=5 cm^{-1} and A=10 cm^{-1}, similar log reductions are predicted for different wave amplitudes. Increasing wave amplitudes is effective only when the gap width is relatively large. For example, when A=30 cm^{-1} in Figure 5.27, the larger log reductions are predicted for the larger wave amplitudes.

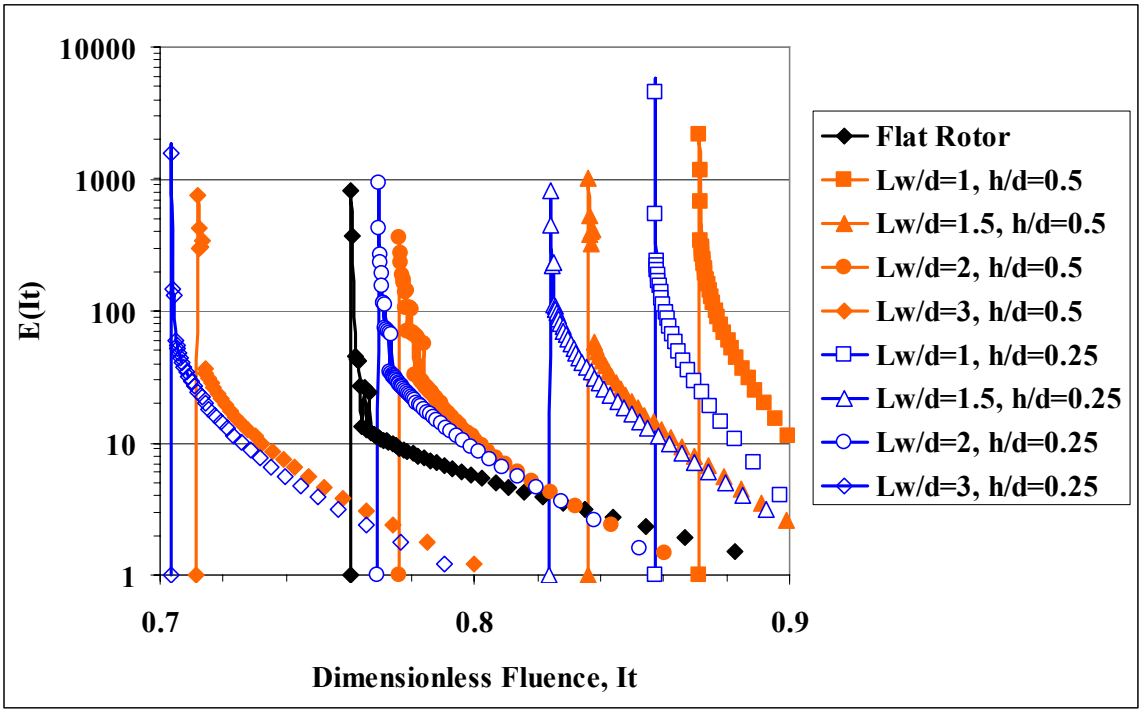

Figure 5.29 Fluence distribution function with A=10 cm^{-1}

5. 7 Conclusions

1. Compared with laminar flow reactors, laminar Taylor vortex reactors have superior performance especially when fluids with high absorption coefficients are treated. Laminar Taylor vortex reactors reduce the boundary layer thickness and the width of the fluence distribution. Moreover the log reduction increases with Taylor number.
2. Taylor vortex reactors have an optimum gap width for each absorption coefficient. The optimum λ/d is about 0.5.
3. The log reduction in Taylor vortex reactors can be correlated by

   $$\ln\left(\frac{N}{N_0}\right) = -\frac{\mathrm{ck}I_0\tau_{\mathrm{av}}R_c}{\alpha d\delta}$$ where c = 0.0125 cm.

4. Turbulent Taylor-Couette flow is not as effective as laminar Taylor-Couette flow because of strong turbulent axial mixing. Moreover, the log reductions in turbulent Taylor-Couette flow decrease with the increase in Taylor number and approach those of a CSTR.
5. Laminar Taylor vortex reactors also demonstrate superior performance compared with turbulent flow reactors when fluids with high absorption coefficients are treated.
6. Wavy rotors will improve the performance of Taylor vortex reactors when the wavelength of the rotor is less than two times the gap width. In addition, decreasing the wavelength is more effective to improve the performance of the reactors than increasing the wave amplitude.

CHAPTER 6

SUMMARY AND FUTURE WORK

6. 1 Summary

This is the first systematic research done on UV disinfection between concentric cylinders in three flow patterns: laminar Poiseuille flow, turbulent flow and both laminar and turbulent Taylor-Couette flow. The present work provides new experimental data for pathogen inactivation in each of the three flow patterns. In addition, the present study constitutes the first systematic numerical CFD predictions of expected inactivation levels. The results suggest optimum gap widths for each flow pattern. It is concluded that laminar Poiseuille flow provides inferior (small) inactivation levels while laminar Taylor-Couette flow provides superior (large) inactivation levels. The relative inactivation levels are: laminar Poiseuille flow < turbulent flow < laminar Taylor-Couette flow.

The principal results obtained can be summarized as:

- A novel method to measure inactivation kinetics with a thin-film annular reactor is proposed. The method can overcome the disadvantages of traditional methods for highly absorptive liquids. Moreover, because many UV devices in industry are continuous flow annular reactors, the parameters of inactivation kinetics obtained from the novel method are more reliable and accurate than those obtained from the traditional methods.
- Compared with the first order inactivation model, the series-event inactivation model is better suited to fit experimental UV inactivation data of *E. coli* K12 and *Y. pseudotuberculosis*.
- Experimental UV inactivation data of *E. coli* K12 were calculated with the series-event inactivation model, and the values of the inactivation constant k=0.67474 cm^2/mJ and threshold n=4 with the coefficient of determination R^2=0.987 and the

standard deviation σ_y=0.133 were obtained. These parameters are compared to a value of k=0.32494 cm^2/mJ with R^2= 0.907 and σ_y=0.354 for the first order inactivation model.

- Experimental UV inactivation data of *Y. pseudotuberculosis* were calculated with the series-event inactivation model, and the values of the inactivation constant k=0.984 cm^2/mJ and threshold n=3 with the coefficient of determination R^2=0.972 and the standard deviation σ_y=0.212 were obtained. These parameters are compared to a value of k=0.557 cm^2/mJ with R^2= 0.916 and σ_y=0.402 for the first order inactivation model.
- There is an optimum gap width for each absorption coefficient. The optimum λ/d for laminar flow reactors, turbulent flow reactors and laminar Taylor vortex reactors are 1.5, 1 and 0.5 respectively.
- The log reduction in laminar reactors can be correlated by

$$\ln\left(\frac{N}{N_0}\right) = -\frac{kI_0\tau_{av}}{\left[1+m(1/\kappa-1)\right]\exp(\alpha dm)}.$$

- The log reduction in turbulent reactors (irradiated from the inner cylinder) can be correlated by $\ln\left(\frac{N}{N_0}\right) = -\frac{\mathrm{ck}I_0\tau_{\mathrm{av}}R_c}{\alpha d\delta}$ with a value of c = 0.0158 cm
- The log reduction in Taylor vortex reactors (irradiated from the outer cylinder) can be correlated by $\ln\left(\frac{N}{N_0}\right) = -\frac{\mathrm{ck}I_0\tau_{\mathrm{av}}R_c}{\alpha d\delta}$ with a value of c = 0.0125 cm
- Turbulent Taylor-Couette flow is not as effective as laminar Taylor-Couette flow because of strong turbulent axial mixing. Moreover, the log reductions in turbulent Taylor-Couette flow decrease with the increase in Taylor number and approach those of a CSTR. Therefore, the Taylor vortex reactors should be operated in laminar Taylor-Couette flow and with Taylor numbers as high as possible.

- Wavy rotors can improve the performance of laminar Taylor vortex reactors when the wavelength of the rotor is less than two times the gap width. In addition, decreasing wavelengths is more effective than increasing wave amplitudes.

6. 2 Future Work

Possible extensions of current work can be summarized as,

Experiments with Wavy Rotors

In Section 5.6, UV inactivation with wavy rotors is investigated numerically and it should be confirmed by experiments. Moreover, it is desirable to find a new and simple correlation equation for wavy rotors like equation (5.3) for flat rotors. The new equation for wavy rotors should provide a prediction for log reductions with dimensionless groups such as Lw/d and h/d.

Research in Dean Flow

The focus of the present study is disinfection between concentric cylinders with the three flow patterns considered. Laminar Taylor-Couette flow introduces a circumferential vortex that reduces the boundary layer thickness and improves bulk mixing. Future work could compare laminar Taylor-Couette flow with Dean flow where the latter introduces an axial vortex.

When the flow is driven by a pressure gradient through a curved tube (or a channel) where the radius of curvature is much larger than the radius of the tube, hydrodynamic instability will cause a secondary flow as a pair of counter-rotating vortices if the Dean number exceeds a certain value (Dean 1927, 1928, Fellouah et al., 2006). The Dean number is defined by

$$De = \frac{U_{av} d_h}{\nu} \left(\frac{d_h}{R_{cuvr}} \right)^{1/2} \tag{6.1}$$

where U_{av} is the average velocity, d_h is the hydraulic diameter, ν is the kinematic viscosity, and R_{curv} is the mean radius of curvature. Figure 6.1 is the schematic figure of Dean vortices in a channel.

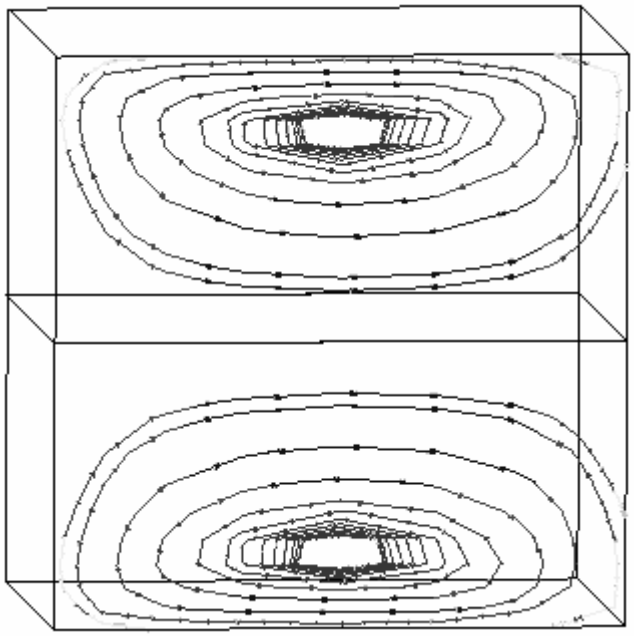

Figure 6.1 Schematic figure of Dean vortices in a channel

In Taylor-Couette flow, an axial flow always stabilizes the circular Couette flow. Higher Taylor numbers are required to maintain Taylor vortices if larger flow rates are necessary to increase processing capability. However, in Dean flow, the axial flow is the origin of Dean vortices. The Dean flow may be subject to the same problems discussed earlier for turbulent Taylor-Couette flow when the axial flow rate is large.

Nonuniform Fluence Rates

In the current work, it is assumed that the fluence rate on the surface of the inner or outer cylinder is uniform. However, if multiple UV lamps are used, there may be a difference between the assumption of uniform and nonuniform fluence rates.

APPENDIX A

UDF SOURCE C CODE

A.1 UDF for UV Inactivation in Turbulent Reactors

```
/************************************************************/
/* Implementation of the Y. pseudotuberculosis model using user-defined scalars  */
/************************************************************/

#include "udf.h"
#include "math.h"
#define R1 0.01225       /* radius of inner cylinder, rotating*/
#define R2 0.0174       /* radius of outer cylinder, stationary*/
#define alpha (3716*log(10))       /* absorbance coefficient       1/m */
/*  I/I0=0.1 @3/4 gap distance when absorbance coefficient alpha=768 */
/*  I/I0=0.1 @1/2 gap distance when absorbance coefficient alpha=1152 */
/*  I/I0=0.1 @1/5 gap distance when absorbance coefficient alpha=2878 */
#define I0 (16.0E+01)         /* Initial radition intensity, W/m2  */
          /* I/I0= R1/y*exp(-alpha*(y-R1))   */
#define keff1 0.572836E-01      /* first order inactiviation constant, m2/(W S) */
#define keffSE 0.983663E-01         /* Series Event inactiviation constant, m2/(W S) */
#define ScT 0.8           /* Turbulent Schmit number */


DEFINE_SOURCE(UDS_1stOrder, cell, thread, dS, eqn)
{
double x,y,source;
double coor[ND_ND];

    C_CENTROID(coor,cell,thread);
    x=coor[0];
    y=coor[1];

    if(x>0.0)
          {
                dS[eqn]=-keff1*I0*R1/y*exp(-alpha*(y-R1))*C_R(cell,thread);
                source=-keff1*I0*R1/y*exp(-alpha*(y-
R1))*C_UDSI(cell,thread,0)*C_R(cell,thread);
          }
    else
          {       dS[eqn]=0.0; source=0.0;}
          return source;
```

```
}

DEFINE_SOURCE(SE_N0, cell, thread, dS, eqn)
{
double x,y,source;
double coor[ND_ND];

    C_CENTROID(coor,cell,thread);
    x=coor[0];
    y=coor[1];

    if(x>0.0)
        {
            dS[eqn]=-keffSE*I0*R1/y*exp(-alpha*(y-R1))*C_R(cell,thread);
            source=-keffSE*I0*R1/y*exp(-alpha*(y-
R1))*C_UDSI(cell,thread,1)*C_R(cell,thread);
        }
    else
        {   dS[eqn]=0.0; source=0.0;}
        return source;
}

DEFINE_SOURCE(SE_N1, cell, thread, dS, eqn)
{
double x,y,source;
double coor[ND_ND];

    C_CENTROID(coor,cell,thread);
    x=coor[0];
    y=coor[1];

    if(x>0.0)
        {
            dS[eqn]=-keffSE*I0*R1/y*exp(-alpha*(y-R1))*C_R(cell,thread);
            source=keffSE*I0*R1/y*exp(-alpha*(y-
R1))*C_R(cell,thread)*(C_UDSI(cell,thread,1)-C_UDSI(cell,thread,2));
        }
    else
        {   dS[eqn]=0.0; source=0.0;}
        return source;
}

DEFINE_SOURCE(SE_N2, cell, thread, dS, eqn)
{
double x,y,source;
double coor[ND_ND];
```

```
    C_CENTROID(coor,cell,thread);
    x=coor[0];
    y=coor[1];

    if(x>0.0)
        {
            dS[eqn]=-keffSE*I0*R1/y*exp(-alpha*(y-R1))*C_R(cell,thread);
            source=keffSE*I0*R1/y*exp(-alpha*(y-
R1))*C_R(cell,thread)*(C_UDSI(cell,thread,2)-C_UDSI(cell,thread,3));
        }
    else
        {   dS[eqn]=0.0; source=0.0;}
        return source;
}

DEFINE_DIFFUSIVITY(diff,cell,thread,i)
{
double x,y,coor[ND_ND],wall_distance;

/* Yplus=0.293306@y=0.0122652 and R1=0.01225*/
/* Yplus=0.293306/(0.0122652-0.01225)*wall_distance=19296*wall_distance*/

    C_CENTROID(coor,cell,thread);
    x=coor[0];
    y=coor[1];
        if((y-R1)<(R2-y))
        {wall_distance=y-R1;}
        else{wall_distance=R2-y;}
    if(x>0.0)
        {
            if((19296*wall_distance)>5.0)
            {return (C_MU_T(cell,thread)/ScT);}
            else{return 0.0;}
        }
    else {return 0.0;}
}
```

A.2 UDF for UV Inactivation in Taylor Vortex Reactors

```
/************************************************************/
/* Implementation of the E-Coli model using user-defined scalars  */
/************************************************************/

#include "udf.h"
```

```
#include "math.h"
#define R1 0.01717       /* radius of inner cylinder, rotating, m*/
#define R2 0.022885      /* radius of outer cylinder, stationary, m*/
#define Q 40           /* Flow rate, mL/min */
#define alpha (1100*log(10))       /* absorbance coefficient       1/m */
#define I0 25.0E+01          /* Initial radition intensity, W/m2  */
          /* I/I0=R2/y*exp(-alpha*(R2-y)), radiation from outer cylinder   */
#define L0 5.34E-02          /* Length of UV lamp, m  */
#define keff1  0.32494E-01        /* first order inactiviation constant, m2/(W S) */
#define keffSE 0.674742E-01       /* Series Event inactiviation constant, m2/(W S) */


DEFINE_PROFILE(velocity_profile,thread,position)
{
  double coor[ND_ND];                    /* this will hold the position vector */
  double y,kappa,temp,Uav;
  face_t f;

  Uav=Q*1.0E-6/60/(3.1416*(R2*R2-R1*R1));
  kappa=R1/R2;
  temp=2.0*Uav/((1-pow(kappa,4))/(1-kappa*kappa)-(1-kappa*kappa)/log(1.0/kappa));
  begin_f_loop(f, thread)
    {
      F_CENTROID(coor,f,thread);
      y = coor[1];
      F_PROFILE(f,thread,position)=temp*(1.0-(y/R2)*(y/R2)+(1.0-
kappa*kappa)/log(1.0/kappa)*log(y/R2));
    }
  end_f_loop(f, thread)
}

DEFINE_SOURCE(UDS_1stOrder, cell, thread, dS, eqn)
{
double x,y,source;
double coor[ND_ND];

     C_CENTROID(coor,cell,thread);
     x=coor[0];
     y=coor[1];

     if(x>0.0&&x<L0)
          {
               dS[eqn]=-keff1*I0*R2/y*exp(-alpha*(R2-y))*C_R(cell,thread);
               source=-keff1*I0*R2/y*exp(-alpha*(R2-
y))*C_UDSI(cell,thread,0)*C_R(cell,thread);
          }
```

```
    else
        {       dS[eqn]=0.0; source=0.0;}
        return source;
}

DEFINE_SOURCE(SE_N0, cell, thread, dS, eqn)
{
double x,y,source;
double coor[ND_ND];

    C_CENTROID(coor,cell,thread);
    x=coor[0];
    y=coor[1];

    if(x>0.0&&x<L0)
        {
            dS[eqn]=-keffSE*I0*R2/y*exp(-alpha*(R2-y))*C_R(cell,thread);
            source=-keffSE*I0*R2/y*exp(-alpha*(R2-
y))*C_UDSI(cell,thread,1)*C_R(cell,thread);
        }
    else
        {       dS[eqn]=0.0; source=0.0;}
        return source;
}

DEFINE_SOURCE(SE_N1, cell, thread, dS, eqn)
{
double x,y,source;
double coor[ND_ND];

    C_CENTROID(coor,cell,thread);
    x=coor[0];
    y=coor[1];

    if(x>0.0&&x<L0)
        {
            dS[eqn]=-keffSE*I0*R2/y*exp(-alpha*(R2-y))*C_R(cell,thread);
            source=keffSE*I0*R2/y*exp(-alpha*(R2-
y))*C_R(cell,thread)*(C_UDSI(cell,thread,1)-C_UDSI(cell,thread,2));
        }
    else
        {       dS[eqn]=0.0; source=0.0;}
        return source;
}

DEFINE_SOURCE(SE_N2, cell, thread, dS, eqn)
```

```
{
double x,y,source;
double coor[ND_ND];

    C_CENTROID(coor,cell,thread);
    x=coor[0];
    y=coor[1];

    if(x>0.0&&x<L0)
        {
            dS[eqn]=-keffSE*I0*R2/y*exp(-alpha*(R2-y))*C_R(cell,thread);
            source=keffSE*I0*R2/y*exp(-alpha*(R2-
y))*C_R(cell,thread)*(C_UDSI(cell,thread,2)-C_UDSI(cell,thread,3));
        }
    else
        {   dS[eqn]=0.0; source=0.0;}
        return source;
}

DEFINE_SOURCE(SE_N3, cell, thread, dS, eqn)
{
double x,y,source;
double coor[ND_ND];

    C_CENTROID(coor,cell,thread);
    x=coor[0];
    y=coor[1];

    if(x>0.0&&x<L0)
        {
            dS[eqn]=-keffSE*I0*R2/y*exp(-alpha*(R2-y))*C_R(cell,thread);
            source=keffSE*I0*R2/y*exp(-alpha*(R2-
y))*C_R(cell,thread)*(C_UDSI(cell,thread,3)-C_UDSI(cell,thread,4));
        }
    else
        {   dS[eqn]=0.0; source=0.0;}
        return source;
}
```

REFERENCES

Andereck, C. D., Liu, S. S. and Swinney, H. L. (1986) Flow regimes in a circular Couette system with independently rotating cylinders. *Journal of Fluid Mechanics* **164**, 155-183

Baier, G. and Graham, M. D. (1998) Two-fluid Taylor-Couette flow: experiments and linear theory for immiscible liquids between corotating cylinders. *Physics of Fluids* **10**, 3045-3055

Baier, G., Grateful, T. M., Graham, M. D. and Lightfoot, E. N. (1999) Prediction of mass transfer in spatially periodic systems. *Chemical Engineering Science* **54**, 343-355

Becker, K. M. and Kaye, J. (1962) Measurements of diabatic flow in an annulus with an inner rotating cylinder. *Journal of Heat Transfer* **84**, 97.

Bioinformatics Educational Resource (2006) *Bacteria Genomes: Yersinia Pseudotuberculosis* [Online], Available www.ebi.ac.uk/2can/genomes/bacteria/Yersinia_pseudotuberculosis.html

Bird, R. B., Stewart, W. E. and Lightfoot, E. N. (2002) *Transport Phenomena*, Wiley, New York

Blatchley, E. R., Dumoutier, N., Halaby, T. N., Levi, Y. and Laine J. M. (2001) Bacterial responses to ultraviolet irradiation, *Water Science and Technology* **43**, 179-186

Buhler, K. and Polifke, N. (1990) Dynamical behavior of Taylor vortices with superimposed axial flow, in Nonlinear Evolution of Spatio-Temporal Structures in Dissipative Continuous Systems (Editors Busse, F. H. and Kramer, L.), Plenum, New York

Cairns, W. L. (1991) *Ultraviolet disinfection: An alternative to Chlorine disinfection*, Trojan Technologies, Inc., London, Ontario, Canada

Canada Communicable Disease Report (1999) Outbreak of *Yersinia Pseudotuberculosis* on British Columbia - November 1998, 25, 97-100. Also available: http://www.phac-aspc.gc.ca/publicat/ccdr-rmtc/99vol25/dr2511ea.html

Chandrasekhar, S. (1960) The hydrodynamic stability of viscid flow between coaxial cylinders. *Proceedings of the National Academy of Sciences of the United States of America*, **46**, 141-143

Chiu, K., Lyn, D. A., Savoye, P. and Blatchley, E. R. (1999) Effect of UV system modification on disinfection performance. *Journal of Environmental Engineering*, **125**, 7-16

Chung, K. C. and Astill, K. N. (1977) Hydrodynamic instability of viscous-flow between rotating coaxial cylinders with fully developed axial flow, *Journal of Fluid Mechanics* **81**, 641-655

Coeuret, F. and Legrand, J. (1981) Mass transfer at the electrodes of concentric cylindrical reactors combining axial flow and rotation of the inner cylinder. *Electrochimica Acta.* **26**, 865-872

Cohen S. and Marom, D. M. (1983) Experimental and Theoretical study of a rotating annular flow reactor. *Chemical Engineering Journal* **27**, 87-97

Coles, D. (1965) Transition in circular Couette flow. *Journal of Fluid Mechanics* **21**, 385-425

Collins, H. F. and Selleck, R. E. (1972) Process kinetics of wastewater chlorination, *SERL Report*, Univ. of Calif., Berkeley, 72-75

Couette, M. (1890) Etudes sur le frottement des liquids. *Ann. de Chim. et de Phys*. **21**, 433-510

Davey, A., DiPrima, R. C. and Stuart, J. T. (1968) On the instability of Taylor vortices. *Journal of Fluid Mechanics* **31**, 17-52

Davidson, P. A. (2004) *Turbulence: An Introduction for Scientists and Engineers*, Oxford University Press

Dean, W. R. (1927) Note on the motion of fluid in a curved pipe. *Philosophical Magazine* **4**, 208-223 Sp. Iss. 7th Series

Dean, W. R. (1928) The stream-line motion of fluid in a curved pipe (Second paper). *Philosophical Magazine* **5**, 673-695 Sp. Iss. 7th Series

DiPrima, R. C. (1960) The stability of a viscous fluid between rotating cylinders with an axial flow. *Journal of Fluid Mechanics* **9**, 621-631

DiPrima, R. C. and Pridor A. (1979) The stability of viscous-flow between rotating concentric cylinders with an axial flow. *Proceeding of the Royal Society of London. Series A, Mathematical and Physical Sciences* **366**, 555-573

Donnelly, R. J. (1958) Experiments on the stability of viscous flow between rotating cylinders. I. Torque measurements. *Proceeding of the Royal Society of London. Series A, Mathematical and Physical Sciences* **246**, 312-325

Donnelly, R. J. (1960) Experiments on the stability of spiral flow between rotating cylinders. *Proceedings of the National Academy of Sciences of the United States of America* **46**, 1150

Fasel, H. and Booz, O. (1984) Numerical investigation of supercritical Taylor-vortex flow for a wide gap. *Journal of Fluid Mechanics* **138**, 21-52

Favier, G., Escudero, M. and De Guzman, A. (2001) Effect of Clorine, Sodium Chloride, Trisodium Phosphate and Ultraviolet Radiation on the Reduction of *Yersinia enterocolitica* and Mesophilic Aerobic Bacteria from Eggshell Surface. *Journal of Food Protection*, **64**, 1621-1623

FDA/Center for Food Safety & Applied Nutrition (2005) *Yersinia enterocolitica* [Online], Available: http://www.foodsafety.gov/~mow/chap5.html

Fellouah, H., Castelain, C., Moctar, A. O. E. and Peerhossaini, H. (2006) A criterion for detection of the onset of Dean instability in Newtonian fluids. *European Journal of Mechanics B/Fluids* **25**, 505-531

Fenstermacher, P. R., Swinney, H. L. and Gollub, J. P. (1979) Dynamical instabilities and the transition to chaotic Taylor vortex flow. *Journal of Fluid Mechanics* **94**, 103-128

Forney, L. J., Skelland, A. H. P., Morris, J. F. and Holl, R. A. (2002a) Taylor vortex column: Large shear for liquid-liquid extraction. *Separation Science and Technology* **37**, 2967-2986

Forney, L. J., Pierson, J. A. and Goodridge, C. F. (2002b) Development of an advanced UV disinfection technology. *Ann. Rep. for Food-PAC*, Atlanta, GA

Forney, L. J., Goodridge, C. F. and Pierson, J. A. (2003a) Ultraviolet disinfection: Similitude in Taylor-Couette and channel flow. *Environmental Science and Technology* **37**, 5015-5020

Forney, L. J. and Pierson, J. A. (2003b) Optimum photolysis in Taylor-Couette flow. *AIChE Journal* **49**, 727-733

Forney, L. J. and Pierson, J. A. (2003c) Photolytic reactors: Similitude in Taylor-Couette and channel flows. *AIChE Journal* **49**, 1285-1292

Forney, L. J., Pierson, J. A. and Ye, Z. (2004) Juice irradiation with Taylor-Couette flow: UV inactivation of *Escherichia coli*. *Journal of Food Protection* **67**, 2410-2415

Forney, L. J., Pierson, J. A. and Giorges, A. (2005a) Photon absorption in modified Taylor-Couette flow: Theory and experiment. *Industrial & Engineering Chemistry Research* **44**, 5193-5198

Forney, L. J., Ye, Z. and Giorges, A. (2005b) Fast competitive reactions in Taylor-Couette flow. *Industrial & Engineering Chemistry Research* **44**, 7306-7312

Fox, R. O. (2003) *Computational Models for Turbulent Reacting Flows*. Cambridge University Press

Froment, G. F. and Bischoff, K. B. (1990) *Chemical Reactor Analysis and Design*, John Wiley & Sons, New York

Goldstein, S. (1937) The stability of viscous fluid flow between rotating cylinders. *Proceedings of the Cambridge Philosophical Society* **33**, 41-61

Gravas, N. and Martin B. W. (1978) Instability of viscous axial-flow in annuli having a rotating inner cylinder. *Journal of Fluid Mechanics* **86**, 385

Gu, Z. H., and Fahidy, T. Z. (1985) Characteristics of Taylor vortex structure in combined axial and rotating flow. *The Canadian Journal of Chemical Engineering* **63**, 710-715

Gu, Z. H., and Fahidy, T. Z. (1986) The effect of geometric parameters on the structure of combined axial and taylor-vortex flow. *The Canadian Journal of Chemical Engineering* **64**, 185-189

Haim, D. and Pismen, L. M. (1994) Performance of a photochemical reactor in the regime of Taylor-Gortler vortical flow. *Chemical Engineering Science* **49**, 1119-1129

Harm, W. (1980) *Biological Effects of Ultraviolet Radiation*, Cambridge University Press

Harris, G. D., Adams, V.D., Sorensen, D. L. and Curtis, M. S. (1987) Ultraviolet inactivation of selected bacteria and viruses with photoreactivation of the bacteria. *Water Research* **21**, 687-692

Hasoon, M. A. and Martin, B. W. (1977) The stability of viscous axial flow in an annulus with a rotating inner cylinder. *Proceedings of the Royal Society of London Series A, Mathematical and Physical Sciences* **352**, 351-380

Howes, T. and Rudman, M. (1998) Flow and axial dispersion simulation for traveling axisyrnrnetric Taylor vortices. *AIChE Journal* **44**, 255-262

Hoyer, O. (1998) Testing performance and monitoring of UV systems for drinking water disinfection. *Water Supply* **16**, 424-429

Ikeda, E. and Maxworthy, T. (1994) Spatially forced corotating Taylor-Couette flow. *Physical Review E* **49**, 5218-5224

Jagger, J. (1967) Introduction to Research in Ultra-Violet Photobiology. *Prentice-Hall, Inc.*, Englewood Cliffs, NJ

Jones, C. A. (1985) The transition to wavy Taylor vortices. *Journal of Fluid Mechanics* **157**, 135-162

Kataoka, K., Doi, H., Hongo, T. and Futagawa, M. (1975) Ideal plug-flow properties of Taylor vortex flow. *J. Chem. Eng. Japan* **8**, 472-476

Kataoka, K., Doi, H. and Komai, T. (1977) Heat-mass transfer in Taylor vortex flow with constant axial-flow rates. *International Journal of Heat and Mass Transfer* **20**, 57

Kaye, J. and Elgar, E. C. (1958) Modes of adiabatic and diabatic fluid flow in an annulus with an inner rotating cylinder. *Transactions of ASME* **80**, 753-765

Koschmieder, E. L. (1979) Turbulent Taylor vortex flow. *Journal of Fluid Mechanics* **93**, 515-527

Koutchma, T. and Parisi, B. (2004a) Biodosimetry of *Escherichia coli* UV inactivation in model juices with regard to dose distribution in annular UV reactors. *Journal of Food Science* **69** E14-E22

Koutchma, T., Keller, S., Chirtel, S., and Parisi, B. (2004b) Ultraviolet disinfection of juice products in laminar and turbulent flow reactors. *Innovative Food Science & Emerging Technologies* **5** 179-189

Kowalski, W. J. (2001) *Design and optimization of UVGI air disinfection system*, PhD thesis, Pennsylvania State University

Launder, B. E. and Spalding, D. B. (1972) *Lectures in Mathematical Models of Turbulence*. Academic Press, London, England

Lueptow, R. M., Dotter, A. and Min, K. (1992) Stability of axial flow in an annulus with a rotating inner cylinder. *Physics of Fluids* **4**, 2446-2455

Lyn, D. A., Chiu, K., and Blatchley, E. R. (1999) Numerical modeling of flow and disinfection in UV disinfection channels. *Journal of Environmental Engineering*, **125**, 17-26

Lyn, D. A. and Blatchley, E. R. (2005) Numerical computational fluid dynamics-based models of ultraviolet disinfection channels. *Journal of Environmental Engineering*, **131**, 838-849

Mallock, A. (1896) Experiments of fluid viscosity. *Proceeding of the Royal Society of London. Series A, Mathematical and Physical Sciences* **183**, 41-56

March, J. (1985) *Advanced Organic Chemistry*. John Wiley & Sons, Inc., New York, 3rd edition

Marchisio D. L., Barresi A. A. and Fox R. O. (2001) Simulation of turbulent precipitation in a semi-batch Taylor-Couette reactor using CFD. *AIChE Journal* **47**, 664-676

Mellon, M. G. (1950) Analytical Absorption Spectroscopy, John Wiley & Sons, Inc., New York

Middleman, S. (1998) An Introduction to Mass and Heat Transfer: Principles of Analysis and Design, John Wiley & Sons, Inc., New York

Miller, L. G. and Kaspar C. W. (1994) *Escherichia coli* O157:H7 acid tolerance and survival in apple cider. *Journal of Food Protection* **57**, 460-464

Min, K. and Lueptow, R. M. (1994) Circular Couette flow with pressure driven axial flow and a porous inner cylinder. *Experiments in Fluids* **17**, 190-197

Ng, B. S. and Turner, E. R. (1982) On the linear-stability of spiral flow between rotating cylinders. *Proceedings of the Royal Society of London Series A, Mathematical and Physical Sciences* **382**, 83-102

Park, Y., Forney, L. J., Kim, J. H. and Skelland, A. H. P. (2004) Optimum emulsion liquid membranes stabilized by non-Newtonian conversion in Taylor-Couette flow. *Chemical Engineering Science* **59**, 5725-5734

Park, Y., Skelland, A. H. P., Forney, L. J. and Kim, J. H. (2006) Removal of phenol and substituted phenols by newly developed emulsion liquid membrane process. *Water Research* **40**, 1763-1772

Pudjiono, P. I., Tavare, N. S., Garside, J., and Nigam, K. D. P. (1992) Residence time distribution from a continuous Couette flow device. *Chem. Eng. J.* **48**, 101-110

Pudjiono, P. I. and Tavare, N. S. (1993) Residence time distribution analysis from a continuous Couette flow device around critical Taylor number. *Can. J. Chem. Eng.* **71**, 312-318

Radata, Inc. (2006) A UV System for Everyone. [Online] http://www.radata.com/wtest/infopacket/treatment/wedeco_uv.pdf

Rafique, M. and Lami, S. S. (2001) Flow regimes and vortex competition in modified Taylor-Couette system: Inner Rotating wavy cylinder coaxial with a smooth stationary outer cylinder, *12th International Couette-Taylor Workshop*, Evanston, IL

Lord Rayleigh (1916) On the dynamics of revolving fluids. *Proc. Roy. Soc. London. A* **93**, 148-154

Resende, M. M., Vieira, P. G., Sousa R., Giordano, R. L. C. and Giordano R. C. (2004) Estimation of Mass Transfer Parameters in a Taylor-Couette-Poiseuille Heterogeneous Reactor. *Brazilian Journal of Chemical Engineering* **21**, 175-184

Rotz, C. A. and Suh, N. P. (1979) Vortex motion induced by V-grooved rotating cylinders and their effect on mixing performance. *Journal of Fluid Mechanics* **101**, 186-192

Schlichting, H. and Gersten, K. (2000) *Boundary-Layer Theory*, Springer-Verlag Berlin Heidelberg

Schwarz, K. W. (1964) Modes of instability in spiral flow between rotating cylinders. *Journal of Fluid Mechanics* **20**, 281

Sczechowski, J. G., Koval, C. A. and Noble R. D. (1995) A Taylor vortex reactor for heterogeneous photocatalysis. *Chemical Engineering Science* **50**, 3163-3173

Severin, B. F., Suidan, M. T. and Engelbrecht, R. S. (1983) Kinetic modeling of U. V. disinfection of water. *Water Research* **17**, 1669-1678

Severin, B. F., Suidan M. T., Rittmann B. E. and Engelbrecht, R. S. (1984) Inactivation kinetics in a flow-through UV reactor, *Journal WPCF* **56**, 164-169

Severin, B. F., Suidan M. T., Rittmann B. E. and Engelbrecht, R. S. (1984) Inactivation kinetics in a flow-through UV reactor, *Journal WPCF* **56**, 164-169

Shih, T.-H., Liou, W. W., Shabbir, A., Yang, Z. and Zhu. J. (1995) A new k-ε eddy-viscosity model for high Reynolds number turbulent flows - Model development and validation.. *Computers Fluids* **24**, 227-238

Snyder, H. A. (1962) Experiments on stability of spiral flow at low axial Reynolds numbers. *Proceedings of the Royal Society of London Series A, Mathematical and Physical Sciences* **265**, 198-214

Sorour, M. M. and Coney, J. E. R. (1979) Characteristics of spiral vortex flow at high Taylor numbers. *Journal Of Mechanical Engineering Science* **21**, 65

Swanson, K. J., Leasor, S. B. and Downing D. L. (1985) Aciduric and heat resistant microorganisms in apple juice and cider processing operations. *Journal of Food Science* **50**, 336-339

Taghipour F. (2004) Ultraviolet and ionizing radiation for microorganism inactivation. *Water Research* **38**, 3940-3948

Takeuchi, D. I. and Jankowski, D. F. (1981) A numerical and experimental investigation of the stability of spiral Poiseuille flow. *Journal of Fluid Mechanics* **102**, 101-126

Taylor, G. I., (1923) Stability of a viscous liquid contained between two rotating cylinders. *Proceeding of the Royal Society of London. Series A, Mathematical and Physical Sciences* **223**, 289-343

Turchi, C., Mehos, M. and Pacheco, J. (1993) Design issues for solar-driven photocatalytic systems in *Photocatalytic Purification and Treatment of Water and Air* (Editors Ollis, D. F. and Al-Ekabi, H.), 789-794, Elsevier

US FDA (2000) 21 CFR Part 179. Irradiation in the production, processing and handling of food. *Fed. Regist.* **65**, 71056–71058

Water Environment Federation (1996) *Wastewater Disinfection Manual of Practice FD-10*, Alexandria, VA

Wereley, S. T. and Lueptow, R. M. (1999) Velocity field for Taylor–Couette flow with an axial flow. *Physics of Fluids* **11**, 3637-3649

Wiener, R. J., Snyder, G. L., Prange, M. P., Frediani, D. and Diaz, P. R. (1997) Periodic-doubling cascade to chaotic phase dynamics in Taylor vortex flow with hourglass geometry. *Physical Review E* **55**, 5489-5497

Wilson, B. R. et al. (1992) Coliphage MS2 as a UV water disinfection efficacy test surrogate for bacterial and viral pathogens, Poster Session, 1992 Water Quality Technology Conference, November 1992.

Wolfe, R. L. (1990) Ultraviolet disinfection of potable water. *Environmental Science and Technology* **24**, 768-772

Xue, W., Yoshikawa, K., Oshima A. and Nomura M. (2002) Continuous emulsion polymerization of vinyl acetate. II Operation in a single Couette-Taylor vortex flow reactor using sodium lauryl sulfate as emulsifier. *Journal of Applied Polymer Science* **86**, 2755-2762

Yakhot, V. and Orszag, S. A. (1986), Renormalization group analysis of turbulence: I. Basic theory. *Journal of Scientific Computing* **1**, 1-51

Ye, Z., Koutchma, T., Parisi, B., Larkin, J. and Forney, L. J. (2006), Ultraviolet Inactivation Kinetics of *E. coli and Y. pseudotuberculosis* in Annular Reactors. submitted to *Journal of Food Science*

Zhu, X., Campero, R. J. and Vigil, R. D. (2000) Axial mass transport in liquid-liquid Taylor-Couette-Poiseuille flow. *Chemical Engineering Science* **55**, 5079-5087

Zhu, X. and Vigil, R. D. (2001) Banded liquid-liquid Taylor-Couette-Poiseuille flow. *AIChE Journal* **47**, 1932-1940

VITA

Zhengcai Ye

Zhengcai Ye was born in Jiangsu Province, China. After graduating from East China University of Science and Technology (ECUST) with a Master of Science in Inorganic Materials in 1994, he worked as a Research Associate for three years at the Department of Chemical Engineering, ECUST and as a Chemical and Software Engineer for another three years at Shanghai Baosteel Group Corporation, the largest steelmaking enterprise of China. After awarded with Master of Science in Chemical Engineering from the Florida State University in 2002, Zhengcai Ye began to study for a higher degree at the Georgia Institute of Technology. In the Fall semester of 2006, he was awarded a Doctorate of Philosophy in Chemical Engineering.

Zhengcai Ye's research area is broad, including Chemical Engineering, Metallurgical Engineering, Material Science and Engineering and Software Engineering. However his research interest is in the field of chemical reaction engineering, especially in numerical modeling of chemical reactors with multiphase flow.